

STUDY OF RF STRUCTURES FOR LINEAR ACCELERATORS

By

ASAVARI SANTOSH DHAVALE

(Enrollment No : PHYS 01200704012)

Bhabha Atomic Research Center

Mumbai 400 085, INDIA

A thesis submitted to the

Board of Studies in Physical Sciences

In partial fulfillment of requirements

For the Degree of

DOCTOR OF PHILOSOPHY

of

HOMI BHABHA NATIONAL INSTITUTE

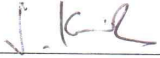


Dec. , 2011

Homi Bhabha National Institute

Recommendations of the Viva Voce Board

As members of the Viva Voce Board, we certify that we have read the dissertation prepared by Asavari S. Dhavale entitled "Study of RF Structures for Linear Accelerators" and recommend that it may be accepted as fulfilling the dissertation requirement for the Degree of Doctor of Philosophy.



Chairman: Prof. S.Kailas **Date:** 26/7



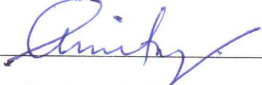
Guide/ Convener: Prof. K. C. Mittal **Date:** 26/7/2012



Member 1: Prof. S.K.Gupta **Date:**



Member 2: Prof. R.G.Pillay **Date:**



External Examiner: Prof. Amit Roy **Date:** 26/7/2012

Final approval and acceptance of this dissertation is contingent upon the candidate's submission of the final copies of the dissertation to HBNI. I hereby certify that I have read this dissertation prepared under my direction and recommend that it may be accepted as fulfilling the dissertation requirement.

Date: 26/7/2012

Place: Mumbai



Guide: Prof. K. C. Mittal

STATEMENT BY AUTHOR

This dissertation has been submitted in partial fulfillment of requirements for an advanced degree at Homi Bhabha National Institute (HBNI) and is deposited in the Library to be made available to borrowers under rules of the HBNI.

Brief quotations from this dissertation are allowable without special permission, provided that accurate acknowledgement of source is made. Requests for permission for extended quotation from or reproduction of this manuscript in whole or in part may be granted by the Competent Authority of HBNI when in his or her judgment the proposed use of the material is in the interests of scholarship. In all other instances, however, permission must be obtained from the author.

Asavari S. Dhavale

DECLARATION

I, hereby declare that the investigation presented in the thesis has been carried out by me. The work is original and has not been submitted earlier as a whole or in part for a degree / diploma at this or any other Institution / University.

Asavari S. Dhavale

ACKNOWLEDGEMENTS

I would like to express deep gratitude to my guide Dr. K. C. Mittal, Project Manager, EBC, Kharghar, BARC for his constant support, guidance and encouragement during the entire period. I would also like to thank my doctoral committee members Dr. S. Kailas, Dr. S.K.Gupta and Dr. R.G.Pillay for their valuable guidance and suggestions.

I would like to thank Sh. D. P. Chakravarthy, Head, Accelerator and Pulse power Division, Bhabha Atomic Research centre, Mumbai for providing facilities, cheerful help. I thank Dr. L. M. Gantayet, Director, Beam Technology Development Group, for his support and encouragement. I also thank Dr. A. K. Ray, Former Director, Beam Technology Development Group, and Raja Ramanna Fellow, BARC for his interest in the activity.

I would like to thank all my colleagues at Accelerator and Pulse Power Division for their help in conducting the experiments. In particular I want to thank Sh.S.R.Ghodke, Sh.S.Nayak, Sh.A.Roy and Smt. Shreya Sarkar. I would especially like to thank Smt. Supriya Barje for her prompt help in making drawings. I would also like to thank my associates from MDPDS workshop Sh. V.V.Marathe and Sh.A.V.Apte for their help and cooperation in mechanical design.

Finally I would like to thank my family especially my husband and daughter for their unconditional love and support.

Asavari S. Dhavale

SPECIAL ACKNOWLEDGEMENTS

As work on Niobium material was carried out at Thomas Jefferson Laboratory (TJNAF), USA, I would like to thank Dr.G.Myneni for giving me an opportunity to work there and making available the facilities where I got introduced to a new field of material science. I also thank him for his help, support and guidance during my stay at USA.

I would also like to thank Dr. G. Ciovati, TJNAF, USA for his help in conducting experiments and analyzing the data. I admired his keen interest and enthusiasm for the work. I thank him for many fruitful discussions and suggestions during this period.

I thank Mr. M. Morrone and Mr. P. Kushnick from TJNAF, USA for providing technical help during the experiments, without their help and cooperation it would have been difficult to complete the work in time.

During my stay at Jefferson lab. I made wonderful friends who helped in several ways. Especially I would like to thank Chen, Janardan, Raja and Shuba for their help and wonderful company.

Asavari S. Dhavale

CONTENTS

	Page No.
SYNOPSIS	11
LIST OF FIGURES	18
LIST OF TABLES	22
LIST OF PUBLICATIONS	23
CHAPTER 1 INTRODUCTION	24
CHAPTER 2 THEORY	30
2.1 THEORY OF RF ACCELERATORS	30
2.1.1 CAVITY FUNDAMENTALS	30
2.1.2 FIGURES OF MERIT	33
2.1.3 TRANSMISSION LINE	34
2.2 BASICS OF SUPERCONDUCTIVITY	36
2.2.1 BCS THEORY	37
2.2.2 SUCCESSES OF BCS THEORY	39
2.2.3 GINZBURG-LANDAU(G-L) THEORY	40
2.2.4 TYPE I AND TYPE II SUPERCONDUCTORS	43
2.2.5 CRITICAL CURRENT DENSITY, J_C AND PINNING FORCE, F_P	47
2.3 CHEMICAL PROCESSES	47
2.3.1 BUFFERED CHEMICAL POLISHING, BCP	48
2.3.2 ELECTROPOLISHING, EP	48
2.3.3 LOW TEMPERATURE BAKING, LTB	49
CHAPTER 3 DESIGN OF FUNDAMENTAL POWER COUPLER	50

3.1 INTRODUCTION	50
3.2 DESIGN CRITERIA	51
3.2.1 CHOICE OF THE COUPLER	51
3.2.2 POSITION OF THE COUPLER	52
3.2.3 CHOICE OF COUPLING FACTOR	52
3.2.4 EFFECT OF BEAM LOADING	53
3.3 COMPUTATION OF EXTERNAL Q	55
3.3.1 KROLL- YU METHOD	57
3.3.2 P. BALLEYGUIER METHOD	62
3.3.3 VALIDATION OF KROLL-YU METHOD	66
3.3.4 COMPARISON OF DIFFERENT COMPUTATIONAL METHODS	67
3.3.5 RESULTS AND DISCUSSION	69
3.4 DESIGN OF DOOR-KNOB TRANSITION	74
3.5 OPTIMIZATION OF ENDCELL AND COUPLER FOR 5-CELL CAVITY	75
3.5.1 OPTIMIZATION OF END CELL	76
3.6 CONCLUSION	78
CHAPTER 4 EXPERIMENTAL RESULTS	80
4.1 INTRODUCTION	80
4.2 MEASUREMENT PROCEDURE	80
4.2.1 MEASUREMENT OF f_0 AND Q_0	80
4.2.2 MEASUREMENT OF R/Q	81

4.2.3 MEASUREMENT OF Q_{ext} OF THE POWER COUPLER	82
4.3 EXPERIMENTAL SET-UP	83
4.3.1 RESULTS OF 1.05 GHZ CAVITY	83
4.3.2 DISCUSSION	85
4.4 RESULTS OF 700 MHZ CAVITY	91
4.5 RESULTS OF FORMED CAVITY	93
4.6 CONCLUSION	95
CHAPTER 5 MULTIPACTING ANALYSIS OF COAXIAL COUPLER	96
5.1 INTRODUCTION	96
5.2 THEORY	98
5.3 DEVELOPMENT OF CODE	102
5.4 RESULTS AND DISCUSSION	104
5.5 CONCLUSION	110
CHAPTER 6 STUDY OF MATERIALS FOR CAVITY PRODUCTION	113
6.1 INTRODUCTION	113
6.2 EXPERIMENTAL SETUP	113
6.2.1 SAMPLE PREPARATION	115
6.3 EXPERIMENTAL METHODS	115
6.3.1 THERMAL CONDUCTIVITY MEASUREMENT	115
6.3.2 MAGNETIZATION MEASUREMENT	117
6.3.3 MEASUREMENTS OF SURFACE SUPERCONDUCTIVITY	118
6.4 EXPERIMENTAL RESULTS	120
6.4.1 THERMAL CONDUCTIVITY	120

6.4.2 DC MAGNETIZATION	121
6.4.3 SURFACE SUPERCONDUCTIVITY	126
6.4.4 CRITICAL CURRENT DENSITY, J_c	128
6.4.5 PINNING FORCE, F_p	131
6.5 DISCUSSION	134
6.6 CONCLUSION	136
CHAPTER 7 CONCLUSION	138
REFERENCES	140
REPRINTS OF PUBLISHED PAPERS	

SYNOPSIS

Particle accelerator technology has tremendous usage in the field of industry as well as basic sciences. The linear accelerators are especially useful in the field of medicine, applied sciences, basic research and various industrial areas. With development of free electron lasers (FEL) a demand for high brightness sources has increased. Considering the potential of this field, Accelerator and Pulse Power Division (APPD) has taken up several accelerator development projects. An Electron Beam Center (EBC), Khargher that houses two industrial accelerators 10 MeV, 10 kW RF electron linac and 3 MeV, 30 kW has been established for the industrial applications like irradiation of cables, spices, medical equipment [1, 2]. Another project of national interest is the development of Accelerator Driven Subcritical System (ADSS) that will be mainly utilized for the transmutation of nuclear waste. It involves development of RF accelerator system to accelerate proton beam from 50 keV to 1 GeV. The proton beam generated by ion source will be accelerated upto 100 MeV by various stages of normal conducting accelerating structures viz., RFQ, CCDTL, CCL. The last module that will accelerate proton beam from 100 MeV to 1 GeV ($\beta > 0.42$) will be superconducting coupled cavity structure made up of elliptical cavities [3,4].

The ever increasing demand of high field gradients has opened up new avenues in the field of superconducting accelerators. The CEBAF, SNS are some of the large accelerator facilities that are in existence [5,6]. The future of ongoing ILC and ADS projects is solely dependent on the superconducting technology [7,8,9]. Also in many of the Nuclear Physics Laboratories, SC post accelerators are used [10,11]. Generally, for the acceleration of particles having low energy ($\beta < 0.3$), Quarter Wave Resonator, Spoke type cavities [12] are more popular whereas at higher energies ($\beta > 0.6$) elliptical cavities are more suitable. The applications where high energy and high current beams are required, superconducting RF (SCRf) linear accelerators (linac) are the obvious choice. For the acceleration of proton, electrons or heavy ions having relativistic velocity $\beta \sim 0.4$ to 1, mainly coupled cavity structures are used.

The study of RF structures is a vast subject and to make the feasible accelerating structure an in depth understanding of several physics phenomena is required. In case of superconducting accelerator structures the study of cavity, fundamental power coupler (FPC) and higher order mode (HOM) coupler are the most important areas. The performance of these devices is limited by thermal quenching, field emission and multipacting [13-17]. Also the superconducting materials and the processes used to clean the cavity surface play important role in achieving the final accelerating gradient [18,19]. Among these **the present thesis is focused on the three areas pertaining to SCRf that are the study of Fundamental Power Coupler, Multipacting study of the Coupler and the study of materials for the cavity production.**

The RF power generated by RF power source is fed to the cavity with the help of power coupler. It is the most intricate and vital part of any RF accelerator, as the amount of power fed to the accelerator and hence the electric field gradient generated in the cavity depends on the design of coupler, also it is the portion of accelerator that separates the ultra high vacuum cavity region from the atmospheric region. In case of superconducting accelerators the scenario is even more complicated by the fact that in addition to above mentioned roles, coupler also separates the region of room temperature and the LHe temperature. It is a transition element that goes from

the power source (atmospheric pressure, room temperature) to the inside of cryostat (ultrahigh vacuum, LHe temperature).

Any mismatch at the coupler results in the improper field gradient as well as the reflection of RF power at the source side. This in turn can damage the other components present in the transmission line like directional coupler, circulator, ceramic windows etc. Thus a careful study of cavity and the coupler parameters and optimization of the coupling factor between cavity resonator and the input coupler is essential [20]. The design of coupler is not unique for any accelerator but varies as per the type of accelerator structure, the power level, operating frequency and the availability of the space required. Considering the technological and engineering challenges this topic presents, it is chosen as a topic of study.

The performance of superconducting cavity, couplers and ceramic windows is greatly affected due to multipacting. Beyond a certain threshold, cavity fields cannot be increased with increase in input power as incident power is absorbed by multipacting electrons. Evidence of multipacting has been observed experimentally in many RF devices. Thus it is essential to study the multipacting phenomena at various power levels and RF frequencies.

The word “multipacting” is a contraction of the phrase multiple impacts. In a RF device, an electron originating from the wall, by bombardment of charged particles/x-rays or produced by the ionization of the residual gas, gets energized by the electromagnetic fields present in the device. When such an electron strikes the wall, depending upon the incident energy of incident electron, more number of electrons are knocked out if the secondary emission coefficient (SEC), δ of the surface is greater than one. In turn the secondary electrons are accelerated and upon impact produce another generation of electrons. The process repeats and a large number of electrons are generated. If the resonance condition is established, an electron current increases exponentially. It is limited only by the space charge effect and the RF power. The performance of coupler is often degraded by the occurrence of multipacting. Thus it is important to optimize coupler dimensions so that required coupling factor is achieved while minimizing the risk of multipacting.[16,21]

Lead and Niobium are commonly used materials for the SCRF applications. Of these lead-coated copper cavities were used in the projects like LEP at CERN. Though, the coated cavities are cheaper than the niobium cavities, the performance of the structures depends on the quality of the coating and the accelerating gradient in these cavities is less than the niobium cavities. Niobium is a more popular material as it is machinable and high accelerating gradients can be achieved after careful surface treatments like Buffered Chemical Polishing (BCP), Electropolishing (EP) and Low Temperature Baking (LTB). In the recent years, Ingot technology has taken a root as the average quality factor of the cavities fabricated from ingots is higher thus it is cost effective and more suitable for the CW applications like ADSS.

The use of superconducting rf (gigahertz range) cavities made of high purity (residual resistivity ratio > 200) bulk niobium has been increasing steadily over the last decade, as these cavities are being employed in a growing number of accelerator facilities all over the world for applications that range from basic energy science to high energy physics. This demand requires continuous improvement of the cavity performance, both in terms of higher quality factors (to

reduce cryogenic losses) and higher accelerating gradients (to reduce the real-estate gradient of high-energy accelerators).

The most outstanding issue related to the basic understanding of the superconductivity of high-purity, bulk Nb in strong rf fields is the occurrence of a sharp increase of the RF losses when the peak magnetic field, B_p , reaches about 90 mT; consequently limiting the operational accelerating gradient of SRF Nb cavities for particle accelerators to about 25 MV/m. This phenomenon was discovered in 1997 [22, 23], after the development of improved surface cleaning techniques allowed the preparation of cavities which achieved high surface fields, without being limited by “extrinsic” losses, such as those caused by field emission.

Experiments showed that the onset of the newly discovered “anomalous” losses, which are commonly referred to as “high field Q-slope” or “Q-drop”, range between 80-110 mT (it has been established that the Q-drop is a magnetic field phenomenon), depending on the particular material-processing combination. Lower onset of the Q-drop is typically associated with “rougher” surfaces.

Currently, two types of high-purity (residual resistivity ratio greater than 200) Nb material are used for cavity fabrication: fine grain (ASTM 5), and large (cm^2 size) grain or even single crystal. The two techniques currently used for the final surface polishing of Nb cavities are Buffered Chemical Polishing (BCP) and Electropolishing (EP). An empirical “cure” for the Q-drop had already been discovered in 1998 and consisted of a low-temperature (100-140 °C, 48 h) baking of the cavities in ultra-high vacuum [24,25,26].

Though the empirical data is available from the cavity experiments, there is no clear understanding of the phenomena that causes the improvement in the cavity performance after LTB. Also it is known that cavities treated by electropolishing perform better than those treated by BCP but the fundamental knowledge of the processes and their effect on the basic properties of the niobium is lacking. Hence the detailed study of the superconducting properties of the Large grain (Ingot A-D) and FG material treated with various surface treatments is carried out in order to understand the effect of the surface treatments on the basic properties of niobium and their possible effect on the Q-drop. The thesis is organized in seven chapters as described below.

Chapter 1 : Introduction

The applications and need of superconducting accelerators is discussed. The aim and scope of the present thesis work is discussed.

Chapter 2 : Theory

This chapter gives the basic theory of RF accelerators and the RF parameters that are important in the accelerator design. The basic superconductivity theory is included. Also, the brief information about the chemical processes used in cavity processing is included for the sake of completeness.

Chapter 3 : Design of Fundamental Power Coupler

This chapter contains the detailed analysis and discussion of the various cavity and coupler parameters that are essential to optimize the coupler dimensions. Also the effect of beam loading and its effect on the requirement of coupling factor or external Q is discussed. The computation of External Q is an important step in the optimization of coupler parameters. The chapter discusses in detail different computational methods employed to compute external Q using the standard electromagnetic codes. The comparison of the computational results using different methods is added. The computational results for the single cells operating at 700 MHz and 1056 MHz are presented. Also the optimization of the end cell and coupler dimensions for 5-cell 700 MHz cavity is presented. This chapter also covers the design of the other coupler components in transmission line [27-30].

Chapter 4 : Experimental Results

The experimental studies were carried out on a prototype copper cavity and the coupler. The resonant frequency, ratio of Shunt Impedance, R to Quality factor, Q (R/Q) and the external quality factor (Q_{ext}) that decides the coupling between cavity and the coupler, are the geometrical factors and their magnitude depends only on the geometry of the cavity and the coupler. It is independent of the material and temperature at which the measurements are done. The chapter gives brief information of the measurement procedures used. It presents in detail the results of the cold model testing of the various cavity coupler parameters like resonant frequency, R/Q, Q_{ext} of the coupler. The higher order modes generated along with the fundamental mode give rise to the additional cryogenic losses, especially the dipole mode. The measurement of R/Q of dipole modes is also carried out. The chapter presents the experimental studies carried out on 700 MHz and the 1.05 GHz cavities fabricated by machining. In practice, the cavities, used in SCRF accelerators, are fabricated by forming the half cells that are later joined by electron beam welding. Hence few trial cavities were fabricated from copper sheet by forming. The experimental results of the formed cavities are also included in this chapter [31-33].

Chapter 5 : Multipacting Study

In practice, two types of multipacting phenomena are observed, viz., one-point multipacting and two-point multipacting. Usually, one point multipacting is observed in RF cavities where only one RF surface is involved. The two point multipacting is observed in the input couplers, co-axial lines, low beta cavities where two RF surfaces are closely spaced.

A RF power is fed to the superconducting cavity with the help of coaxial type of input coupler. The chapter deals with the multipacting analysis of the coaxial coupler. The study of multipacting is an involved process because of the complex geometries of the RF devices, time varying nature of the electromagnetic fields and susceptibility of the phenomena to the surface conditions. Thus the analysis is done using numerical methods.

The study of multipacting essentially involves the tracing of electron trajectories in an electromagnetic field and the calculation of generated secondary electrons upon the impact of primary electrons with the physical boundary of the RF structure. A code is developed in 'C' language to study the multipacting in coaxial coupler. The chapter describes in detail the

evolution of code and the simulation results carried out at different power levels and for different frequencies for various couplers dimensions [34].

Chapter 6 : Study of Materials

This part of the thesis work is carried out at Jefferson Laboratory, Virginia, USA. A system has been developed at Jefferson laboratory for the characterization of the superconducting material [35]. As described earlier the aim of the experiment was to understand the effect of various surface treatments on the superconducting properties of niobium and to understand its possible connection with the Q-slope. The thermal conductivity, DC magnetization, AC measurement and the measurement of transition temperature was carried out on the large grain as well as fine grain niobium samples in the temperature range of 2 K to 8 K. The chapter covers the experimental results carried out on electro polished and baked samples. A detail analysis and the discussion of the experimental results are presented. The variation of critical current density and the pinning force with temperature and magnetic field is studied. A pinning model is proposed based on the experimental results obtained from magnetization measurement. The AC measurements revealed some of the interesting findings about the effect of BCP and EP on the flux penetration. Also the effect of low temperature baking is studied and discussed in detail [36].

Chapter 7 : Conclusion

In conclusion, the computational work revealed that the Kroll-Yu method that was earlier thought to be suitable only for the computation of low external Q can be implemented for computation of high external Q that is for superconducting cavity couplers. The results computed by Kroll-Yu and Pascal methods are matching well. Since external Q is the geometrical factor the validation of design was checked experimentally on the copper model. The experimental and the computed external Q are in good agreement; the percentage error is less than 20%. Also, the measured cavity parameters like resonant frequency, R/Q of monopole and dipole modes are matching with the simulation results. In case of 1.05 MHz cavity, the measured monopole frequency was 1051.17 MHz and the R/Q was 9.404 Ω . The dipole mode was degenerate having frequencies 1469.3 MHz and 1470.6 MHz while the corresponding measured R/Q's were 3.34 Ω and 4.32 Ω . The external Q was measured by keeping coupler in transverse and the longitudinal position. By changing the penetration depth of the inner conductor from -40 mm to 40 mm, the external Q was changed from 6.14×10^8 to 9.6×10^5 in case of transverse coupler while in case of axial coupler external Q of 2.25×10^7 to 5×10^4 was achieved by changing penetration depth from -108 mm to -63 mm.

The coupler is the transition element so mixed mode that is standing waves exist in the coupler at all times for any power level. The multipacting bands were calculated for different coupler dimensions under these conditions. For the simulation of secondary electrons Monte Carlo method was used. The resonant trajectories were traced for 20 impacts. The simulations were carried out for coupler 1 (ID : ϕ 34.78 mm, OD : ϕ 80 mm) and coupler 2 (ID : ϕ 17.38 mm, OD : ϕ 40 mm) at a RF frequency of 350 MHz, 700 MHz and 1050 MHz. The multipacting bands in the power range 0.1 MW to 1 MW were found. The results are in agreement with scaling laws.

In order to understand the effect of various surface treatments, the DC and AC measurements were carried out on large grain as well as fine grain niobium samples with more emphasis on the study of pinning mechanism and flux penetration in the niobium.

The DC magnetization measurements showed that the onset field of flux penetration and the upper critical field do not depend significantly on RRR and do not change significantly after the low-temperature baking. The AC measurements show sensitivity to the surface treatments. The penetration depth is less in the samples treated with EP as compared to BCP, indicating a lower resistivity and therefore higher purity, of the EP treated surface. The near-surface flux penetration field is larger after EP than after BCP and it has no significant dependence on RRR if the surface is treated by EP. A modest increase (less than 10%) of this onset field was measured after 120°C baking. The ratio H_{coh}/H_{c3} remains unchanged with the surface treatments. The effect of low temperature baking is to improve the H_{coh}/H_{c2} ratio and hence the H_{c3}/H_{c2} ratio. In short the low temperature baking improves the coherence phase of the surface superconductivity. The increase in H_{c3} after baking is associated with increase in H_{ffp} .

This chapter includes the summary of all the simulation as well as experimental results. Some of the important findings are discussed in detail. The chapter is concluded with the future scope of the thesis work and the related topics.

References :

- 1] R.C.Sethi et. al., “Design and development of 10 MeV, 10 kW RF Electron Linac for Applied Research and Industrial Applications”, proceedings of the first Asian Particle Accelerator Conference, KEK, Japan, March 1998 (APAC-98), p 193.
- 2] K.C.Mittal et. al., “Development of 3 MeV, 30 kW DC Electron Accelerator at EBC Khargher”, APAC 2007, RRCAT, Indore, India
- 3] P.K. Nema, P.Singh, P. Satyamurthy, S.B. Degweker, V.K. Handu, “ADS programme and associated developments in India-Roadmap and Status of Activities”, IAEA Conference
- 4] P.Singh, “Accelerator Development in India for ADS Programme”, *Pramana*, Vol. 68, No. 2, 331-342, DOI : 10.1007/s12043-7-038-0
- 5] C.Pagani, “Technical Issues for Large Accelerators based on High Gradient SC cavities”, EPAC 2004, Lucerne, Switzerland
- 6] Michael Pekeler, “Fabrication of Superconducting Cavities for SNS”, LINAC 2004
- 7] P.N.Ostroumov, “Application of International Linear Collider SC Cavities for acceleration of Protons”, *Phys. Rev. ST. Accel. Beams*, 1, 120101 (2007)
- 8] C. Pagani, “SRF Activities at INFN Milano - LASA”, SRF 2001
- 9] A.Bossoti et. al., “RF Tests of the beta = 0.5, 5 – cell Trasco Cavities”, EPAC 2004, Lucerne, Switzerland
- 10] V.Nanal, “Operational Experience of the SC Linac Booster at Mumbai”, Proceedings of HIAT09, Venice, Italy
- 11] A.Roy, “SRF Activities at IUAC New Delhi and other Laboratories in India”, Proceedings of SRF2007, Peking University, Beijing, China
- 12] K.W.Shepard et. al., “High Energy Ion Linacs based on Superconducting Spoke Cavities”, *Phys. Rev. ST. Accel. Beams* 6, 080101, 2003
- 13] H.Padamsee, J.Knobloch, T. Hays, “RF Superconductivity for Accelerators”, edited by John Wiley & Sons, p. 183(1998)
- 14] E. Zaplatina, “Design Study of Superconducting Proton Linac Accelerator Cavities”, PAC 99, New York
- 15] S. Koscielniak, “Accelerator Design for a ½ MW Electron Linac for Rare Isotope Beam Production”, EPAC08, 11th European Particle Accelerator Conference, Genoa, June 23-27, 2008
- 16] G.Devanz, “Multipactor Simulations in superconducting cavities and coupler”, *Phys. Rev. ST. Accel. Beams* 4, 01201 (2001)

- 17] H.Padamsee, "A Statistical model for Field Emission in SC Cavities", PAC 93, May 17 – 20, 1993, Washington DC
- 18] G.Ciovati and P.Kneisel, "Measurement of the high-field Q drop in the TM_{010} and TE_{011} modes in a niobium cavity", *Physical Review Special Topics-Accelerators and Beams*, 9, 042001 (2006)
- 19] P.Kneisel, G.R.Myneni et. al., "Development of Large Grain/ Single Crystal Niobium Cavity Technology at Jefferson Lab.", *Proceedings of International Niobium Workshop*, Oct. 30 – Nov. 1, 2006, Araxa, Brazil
- 20] Q.S.Shu et. al., "High Power Coupler for the TESLA Superstructure cavities", PAC 2005, Knoxville, Tennessee
- 21] E.Somersalo, P.Yla-Oijala, "Analysis of Multipacting in Coaxial lines", PAC'95, Dallas, USA(1995)
- 22] P. Kneisel, K. Saito and R. Parodi, in *Proceedings of the 8th Workshop on RF Superconductivity*, Abano Terme, 1997, edited by V. Palmieri and A. Lombardi, (INFN, Legnaro, Italy, 2008), LNL-INFN 133/98, p. 463.
- 23] E. Kako, M. Bolore, Y. Boudigou, J.P. Charrier, B. Coadou, E. Jacques, M. Juillard, J.P. Poupeau, H. Safa, S. Noguchi, M. Ono, K. Saito and T. Shishido, in *Proceedings of the 8th Workshop on RF Superconductivity*, Abano Terme, 1997, edited by V. Palmieri and A. Lombardi, (INFN, Legnaro, Italy, 2008), LNL-INFN 133/98, p. 491.
- 24] P. Kneisel, in *Proceedings of the 9th Workshop on RF Superconductivity*, Santa Fe, NM, 1999, edited by F. Krawczyk, (LANL, Los Alamos, NM, 2000), p. 328.
- 25] B. Visentin, J. P. Charrier and B. Coadou, in *Proceedings of the 1998 European Particle Accelerator Conference*, Stockholm, Sweden, 1998, edited by S. Myers, L. Liljeby, Ch. Petit-Jean-Genaz, J. Poole and K.-G. Rensfelt (IoP, Philadelphia, USA, 1998), p. 1885.
- 26] G. Ciovati, in *Proceedings of the 13th Workshop on RF Superconductivity*, Beijing, China, 2007, edited by J. K. Hao, S. L. Huang and K. Zhao (PKU, Beijing, China, 2008), p. 70
- 27] A.Roy, **A.S.Dhavale**, J.Mondal, K.C.Mittal, "RF Design of a Single Cell Superconducting Elliptical Cavity with Input Coupler", 12th Workshop on RF Superconductivity, Cornell University, USA (2005)
- 28] A.Roy, J. Mondal, K.C.Mittal, "Superconducting Elliptical 1050 MHz $\beta=0.49$ Cavity Design for High Current Proton Accelerator", InPAC'06, Mumbai, India, November 1-4, (2006)
- 29] **A.S.Dhavale** and K.C.Mittal, "Evaluation of external Q of the superconducting cavity using Kroll-Yu method", *Review Of Scientific Instruments* 77, 066101 (2006)
- 30] **A.S.Dhavale** and K.C.Mittal, "Evaluation of External Q using Kroll-Yu Method with Microwave Studio", *Journal of Instrumentation, JINST*, 3 T06001, 2008.
- 31] **A.S.Dhavale** and K.C.Mittal "Design of Input Coupler for the superconducting cavity", **A.S.Dhavale** and K.C.Mittal, *Nuclear Instruments and Methods in Physics Research A*, Volume 604, Issue 3, 11 June 2009, doi: 10.1016/j.nima.2009.03.176 36]
- 32] **A.S.Dhavale** and K.C.Mittal, "RF characterization of elliptical prototype copper cavity and the power coupler", *Journal of Instrumentation, JINST*, 4 T 09002
- 33] K.C.Mittal, **A.S.Dhavale** et.al., "SCRf Program at BARC", InPAC 2009, RRCAT, Indore
- 34] **A.S.Dhavale** and K.C.Mittal, "Study of Multipacting in coaxial coupler", IPAC10, Kyoto, Japan, 2010
- 35] G.Ciovati et.al., "A coaxial TE_{011} Cavity and a system to measure DC and RF properties of Superconductors", *Proceedings of the 13th Workshop on RF Superconductivity (SRF 2007)*, Beijing, China, 2007
- 36] **A.S.Dhavale**, G.Ciovati and G.Myneni, "Effect of Electropolishing and Low Temperature Baking on the Superconducting Properties of Large-Grain Niobium", *Symposium on Superconducting Sci. and Technology of Ingot Niobium (SSTIN10)*, Sep. 22-24, 2010, TJNAF, Newport News, VA

LIST OF FIGURES

1. A pillbox cavity of radius, R and length, L showing TM_{010} field components [p.31]
2. Elliptical cavity showing field distribution simulated using SUPERFISH and the 3-D structure simulated using MWS [p.32]
3. Field distribution in TE_{10} mode in rectangular guide and TEM mode in coaxial line [p.36]
4. Schematic representation of electron-electron interaction transmitted by phonon [p.38]
5. Temperature dependence of energy gap [p.39]
6. Negative surface energy of type II superconductor. Penetration depth and coherence length (top), contribution to free energy (middle), total free energy (bottom) [p.45]
7. Representation of mixed state of type II superconductor showing the normal core encircled by supercurrent vortices [p.46]
8. Magnetic flux density versus applied magnetic field of type I and type II superconductor [p.46]
9. Schematic of SC Cavity with Power Coupler [p.54]
10. Schematic of cavity and coupler as a coupled resonators [p.58]
11. Study of mode frequencies as a function of position of short [p.61]
12. Microwave Studio Output of Simulated Structure [p.62]
13. Comparison of external Q evaluated using Pascal method, Kroll-Yu method and MWS module [p.69]
14. Effect of coupler position, ($f = 700$ MHz) [p.70]
15. Effect of coupler penetration depth, ($f = 700$ MHz) [p.70]
16. Effect of coupler size, ($f = 1.05$ GHz) [p.71]
17. Effect of distance between cavity and coupler, ($f = 1.05$ GHz) [p.71]

18. Effect of penetration Depth, ($f = 1.05$ GHz) [p.72]
19. Effect of Beam Pipe Radius, ($f = 1.05$ GHz) [p.73]
20. Details of Door-knob transition, ($f = 700$ MHz) [p.74]
21. S- parameter response at Door-knob Transition simulated using MWS [p.75]
22. Different types of End cells [p.77]
23. 5-cell assembly with optimized end cell and coaxial coupler simulated using MWS; arrows indicate the direction of electric field (π mode) [p.77]
24. Change of Q_{ext} with penetration depth of inner conductor [p.77]
25. Cavity with Coaxial Coupler and the bead pull set up [p.83]
26. Cavity, Beam pipe and Coupler Parts [p.84]
27. Schematic of cavity and power coupler [p.85]
28. Resonant frequency and Q_1 ; VNA output [p.86]
29. Dipole frequencies; VNA output [p.86]
30. Variation of resonant frequency with bead position [p.87]
31. Frequency shift of TM_{010} mode; VNA output [p.88]
32. Phase shift of TM_{010} mode; VNA output [p.88]
33. Variation of dipole mode frequency, f_1 with bead position [p.89]
34. Variation of dipole mode frequency, f_2 with bead position [p.89]
35. Variation of Q_{ext} with Penetration depth; experimental and computed data [p.91]
36. Frequency response of 700 MHz cavity [p.92]
37. Phase shift due to bead; field inside the cavity [p.92]
38. Comparison of measured and computed External Q of 700 MHz cavity [p.93]
39. Formed Copper cavities ($f = 1.05$ GHz) [p.94]

40. Frequency response of the formed cavity [p.94]
41. Field inside the cavity [p.95]
42. Secondary Emission Curve as a function of Energy [p.100]
43. Flow chart of the program [p.103]
44. a) Multipacting barriers calculated for TTF III coupler using our code and Track3P (shaded portion) as quoted in ref. [92] [p.105]
44. b) Secondary electron yield [p. 105]
45. One Point, 3rd order trajectory of coupler 2 [p. 107]
46. One point, 3rd order trajectory as a function of time of coupler 2 [p. 107]
47. Multipacting bands of coupler 1 calculated for different loads [p. 108]
48. Multipacting bands for different coupler size at a frequency of 1.05 GHz[p. 108]
49. Multipacting band calculated for coupler 1 at different frequencies [p. 109]
50. Multipacting bands of coupler 1 calculated at 1.05 GHz at different initial position [p. 109]
51. Multipacting bands of coupler 3 at different frequencies calculated under standing wave condition. [p. 110]
52. Multipacting trajectory of coupler 1 at 700 MHz at different DC bias voltages [p. 112]
53. Schematic of the experimental setup. [p. 114]
54. Schematic of the EP setup. [p. 115]
55. Typical I-V curve for the EP of the samples. [p. 116]
56. Measured voltage from the pick-up coil as a function of the applied magnetic field during a ramp-up of the field from 0 mT to 600 mT. [p. 118]

57. Frequency change measured during ramp-up and ramp-down of the applied magnetic field at 4 K. [p. 119]
58. Frequency change measured during warm-up of sample D in zero applied field allowing measuring the critical temperature [p. 120]
59. Thermal conductivity as a function of temperature measured on samples D (a) and FG (b) after EP and LTB. [p. 122]
60. Magnetization as a function of the applied field measured on LG sample D at 2.0 K after different surface treatments [p. 123]
61. Critical fields as a function of temperature from DC magnetization methods for sample D (a) and FG (b) after EP. The data were fitted with Eqs. (4) and (5). [p. 125]
62. Frequency shift vs. H for sample C after EP and LTB (a) and for sample FG (b) after BCP and EP. [p. 127]
63. Plot of Critical current density as a function of reduced magnetic field, b at different temperatures for (a) sample D, (b) FG [p. 129]
64. Variation of critical current density with temperature; data and fit for sample D and FG [p. 130]
65. Normalized pinning force plotted against the reduced magnetic field for all temperatures and fit using equation 11; a) LG sample, $A=4.11$, $p=0.79$, $q=1.38$ D b) FG, $A=7.77$, $p=1.39$, $q=1.61$ [p. 133]
66. Plot of $F_{p,max}$ as a function of $H_{c2}(T)$ at different temperatures for sample D and FG [p. 134]

LIST OF TABLES

1. Properties of commonly used superconducting materials for SCRF applications [p.44]
2. Optimized parameters of single, elliptical cavity [p.55]
3. Fitted Frequency and Q_{ext} data [p.61]
4. Effect of Mesh Size on Q_{ext} [p.62]
5. External Q calculation of Pill Box Cavity [p.67]
6. Comparison between P.Balleyguier method and Kroll-Yu method 1.05 GHz Coupler [p.68]
7. Comparison between P.Balleyguier method and Kroll-Yu method 700 MHz Coupler [p.68]
8. Optimized Coupler Dimensions of 700 MHz and 1.05 GHz Cavity [p.73]
9. Optimied dimensions of inner cell and end cell for 700 MHz, 5-cell cavity [p.78]
10. MP power levels estimated by code and from scaling law [p.111]
11. RRR and Ta concentration from the chemical analysis of the samples and calculated from the thermal conductivity at 4.3 K measured on the samples treated by EP. [p.121]
12. Comparison of H_{ffp} and $H_{\text{c}2}$ at 2 K after EP and LTB [p.123]
13. Fitted values of $H_{\text{ffp}}(0 \text{ K})$, $H_{\text{c}2}(0 \text{ K})$ and T_{c} after EP. The experimental value of T_{c} is also indicated for comparison. [p.124]
14. Fitted values of $H_{\text{ffp}}(0 \text{ K})$, $H_{\text{c}2}(0 \text{ K})$ and T_{c} after LTB at 120 °C for 48 h. The experimental value of T_{c} is also indicated for comparison. [p.126]
15. Critical fields in a $\sim 30 \mu\text{m}$ depth from the surface measured at 2 K, after EP and LTB [p.128]
16. Fitted Parameters $J_{\text{c}}(0)$ and K at 2 K after EP treatment [p.130]

LIST OF PUBLICATIONS

Journal Papers

- 1] **A.S.Dhavale** and K.C.Mittal, “RF characterization of elliptical prototype copper cavity and the power coupler”, *Journal of Instrumentation, JINST*, 4 T 09002
- 2] **A.S.Dhavale** and K.C.Mittal “Design of Input Coupler for the superconducting cavity”, *Nuclear Instruments and Methods in Physics Research A*, Volume 604, Issue 3, 11 June 2009, doi: 10.1016/j.nima.2009.03.176 36
- 3] **A.S.Dhavale** and K.C.Mittal, “Evaluation of External Q using Kroll-Yu Method with Microwave Studio”, *Journal of Instrumentation, JINST*, 3 T06001, 2008.

International Conference/ Symposium

- 1] **A.S.Dhavale** and K.C.Mittal, “Study of Mutipacting in coaxial coupler”, IPAC10, Kyoto, Japan, 2010
- 2] **A.S.Dhavale**, G.Ciovati and G.R.Myneni, “Effect of Electropolishing and Low Temperature Baking on the Superconducting Properties of Large-Grain Niobium”, Symposium on Superconducting Sci. and Technology of Ingot Niobium (SSTIN10), Sep. 22-24, 2010, TJNAF, Newport News, VA

National Conference

- 1] K.C.Mittal, **A.S.Dhavale** et.al., “SCRF Program at BARC”, InPAC 2009, RRCAT, Indore

CHAPTER 1

INTRODUCTION

Energy is essential for survival and growth of human civilization. Several means of energy production from wind, solar to nuclear energy are available. Of these majority of the power is generated from fossil fuels. The fossil fuels release CO₂ in the atmosphere, the increasing usage of these fuels to meet the increasing demand of power will lead to doubling the concentration of CO₂ in coming 50-75 years [1] that may lead to severe climate changes. The rate of energy consumption of the planet is increasing at the rate of 2.3% per year and it will continue to increase as the billions of people in the developing countries continue to strive for the better life [2]. The nuclear energy is an alternative that generates power with clean environment. The present nuclear reactors make use of isotope U²³⁵ which represents only 0.7 % of natural uranium. The fuel shortage will occur in the future. Thus it is essential to breed the fissile material from U²³⁸ or Th²³². Also the disposal of nuclear waste generated in the reactors is the biggest challenge the world is facing today.

Carlo Rubbia, a Nobel Prize winner physicist and the former Director of Europe's CERN International Nuclear Physics Laboratory proposed the concept of energy amplifier in 1994. An energy amplifier is a novel type of nuclear power reactor, a subcritical reactor, in which an energetic particle beam is used to stimulate a reaction, which in turn releases enough energy to power the particle accelerator and leave an energy profit for power generation. The reactor being in subcritical state it provides more safety compared to conventional reactors. The concept has more recently been referred to as an Accelerator-Driven System (ADS). The energy amplifier uses an accelerator (e.g. cyclotron or linear accelerator) to produce a beam of protons. The protons hit a heavy metal target such as lead, lead-bismuth, thorium or uranium and produce

spallation neutrons. The heavy isotopes in the blanket assembly, surrounding spallation target, undergo fission producing energy in the process [3]. It is also possible to transmute long-lived nuclear waste in ADS by directing spallation neutrons on the blanket containing the nuclear waste with fissionable fuel. It might be possible to increase the neutron flux through the use of a neutron amplifier, a thin film of fissile material surrounding the spallation source [4].

The link between peaceful and military applications has been shortened due to the inevitable development in nuclear technology. From this angle the breeding reaction of uranium has a risk of proliferation due to large production of plutonium while the breeding of thorium is immune to it. Also thorium is abundantly available in the nature; the present reserves of thorium are enough to produce energy for several thousand years [4].

India being a developing country, its energy production demands are ever increasing. Due to limited reserves of coal and uranium, the large growth in nuclear industry can be realized only by efficient conversion of fertile material into fissile material and utilizing later to produce energy. A closed nuclear fuel cycle that involves reprocessing and recycling of fissile material is inevitable [5].

Large scale utilization of thorium as nuclear fuel has been a long term goal in Indian Nuclear Power program. Three stage program for gradual switch over from Uranium to Plutonium-fueled fast breeders and finally to thorium fuel system has been in place for this purpose. In 2003, India initiated a program to pursue a roadmap on physics studies and stage-wise technology development for ADS. Under this program, activities related to the reactor concepts & design, spallation target system and technology for high power proton accelerator have progressed [6].

The yield of spallation neutrons per proton increases monotonically with the energy of incident proton beam while the total neutron flux per Watt of incident beam reaches nearly constant value above the energy of 1 GeV [7,8]. An upper limit on the beam energy is set by the beam losses while the lower limit is decided by the efficiency of spallation process. In addition, it is required that proton driver be reliable, rugged and stable in order to provide uninterrupted beam power to the spallation target, over long periods of time. Thus the most challenging aspect of the ADS is the development of accelerator that can produce a CW proton beam (> 20 mA) of energy ~ 1 GeV. The superconducting accelerator is the obvious choice for the high energy and high current, CW applications. The main advantage of superconducting cavities is that the RF losses are about five times lower than the normal conducting copper cavities. Though the refrigeration of SC cavities at LHe temperature (2-4 K) is required their efficiency of converting AC power into beam power is $\sim 70\%$ compared to $\sim 15\%$ of the normal conducting ones. The beam aperture in the SC cavities is much larger compared to normal conducting cavities, which allows preservation of better beam quality. Thus it is more suitable for acceleration at high energy.

Since the first use of SRF cavities at Stanford University in 1974 [9], the field of SRF has flourished. Some of the well known SRF facilities include, TRISTAN at High Energy Accelerator Research Organization (KEK), Japan, the Large Electron Positron Collider (LEP) at CERN in Switzerland, the HERA at Deutsches Electron Synchrotron Laboratory (DESY), Germany, the Continuous Electron Beam Accelerator Facility (CEBAF) at Jefferson Laboratory in USA. Apart from this, SC cavities are being developed for variety of new applications like high energy, high luminosity electron-positron collider (ILC), proton-proton colliders, storage rings etc. The performance of the SRF cavities has improved significantly over the last few

decades. The acceleration gradient has improved from 5-10 MV/m to 25-40 MV/m [9]. Recently, field gradient has reached to the theoretical limit of ~ 50 MV/m [10].

At present in the country two superconducting accelerator facilities are existing at IUAC, Delhi and TIFR, Mumbai [11,12]. These are the post accelerator stages made up of Quarter Wave Resonators (QWR), the accelerated beam is used for nuclear physics experiments. A R&D activity of development of superconducting cyclotron is underway at VECC, Kolkata.

Bhabha Atomic Research Center, India has initiated the R&D program to study various aspects of the ADS. The required 1 GeV proton beam will be produced by linear accelerator (linac) in three different phases viz, 20 MeV, 100 MeV and 1GeV. The proton beam will be generated by 50 keV ECR ion source that is accelerated further by 3 MeV RFQ and 20 MeV DTL linac [13]. The intermediate stage between 20 MeV to 100 MeV can be superconducting or normal conducting.. The last module that will accelerate proton beam from 100 MeV to 1 GeV, will be a superconducting accelerator. Accelerator and Pulse Power Division (APPD), BARC is involved in the development of superconducting module for ADS. Essentially it will be a coupled cavity linac made up of elliptical cavity resonators. As an initial stage it was decided to take up the design of single cell. Thus R&D on the design and prototype development of the cavity, power coupler etc. has been started [14, 15, 16].

The study of superconducting RF accelerator involves in depth understanding of the RF structure as well as the superconducting materials. Among the RF structures, study of RF cavity, fundamental power coupler (FPC) and higher order mode coupler (HOM) are most important. The performance of these devices is affected by thermal quenching, field emission and multipacting. The study of superconducting materials and their performance under different chemical or surface treatments is important as the final field gradient achieved in the SC cavity is

severely affected by the surface conditions. Among these the present thesis is focused on the three areas pertaining to SCRF that are the study of Fundamental Power Coupler, Multipacting study of the Coupler and the study of materials for the cavity production. The work reported under this thesis has been carried out at BARC, India and the Jefferson laboratory USA.

The requirement of coupling changes with the load condition. An accelerator being a dynamic system coupling depends on the beam current and the power. Thus design of coupler depends on the operating conditions and the cavity parameters. In the present thesis the coupler design is optimized taking into account the beam loading conditions and the effect of cavity, coupler parameters on the coupling factor and hence on the external Q. The design of power coupler for single cell as well as multiple cells is presented. Also, the experimental results of RF characterization of the cavity and the coupler parameters carried out on the copper prototypes are presented.

Multipacting is a resonant phenomenon that occurs in most of the RF devices and it is necessary to take care of it in the design stage. Since no codes are available to us for multipacting simulation, it was decided to develop the in house code. The thesis presents the details of the code developed and the analysis of the coaxial coupler.

The materials used for the developemnt of the RF cavity play an important role in achieving required design parameters. A lead and niobium are the most commanly used SC materials due to high T_c . But the field gradient achieved with lead coated copper cavities is limited so the niobium is the most popular material. Currently, two types of high-purity (residual resistivity ratio greater than 200) Nb material are used for cavity fabrication: fine grain (ASTM 5), and large (cm^2 size) grain or even single crystal. The two techniques currently used for the final surface polishing of Nb cavities are Buffered Chemical Polishing (BCP) and

Electropolishing (EP). In spite of the careful treatment of the cavity surface, the SC cavities show a reduction in the Q-value after the field of 90-110 mT. This is termed as Q-drop or Q-slope. This is undesirable especially in the applications where high field gradients are required. An empirical “cure” for the Q-drop had already been discovered in 1998 and consisted of a low-temperature baking (LTB) (100-140 °C, 48 h) of the cavities in ultra-high vacuum [17,18,19].

Though the empirical data is available from the cavity experiments, there is no clear understanding of the phenomena that causes the improvement in the cavity performance after LTB. Also it is known that cavities treated by electropolishing perform better than those treated by BCP but the fundamental knowledge of the processes and their effect on the basic properties of the niobium is lacking. Hence the detailed study of the superconducting properties of the Large grain (Ingot A, B, C, D) and FG material was carried out. The samples are treated with Electropolish and Low temperature bake in order to understand the effect of these surface treatments on the basic properties of niobium and their possible effect on the Q-drop. The thesis is organized in seven chapters.

Chapter 2 covers the basic theory of RF accelerators, basics of superconductivity and the brief introduction of different chemical processes used in cavity treatment. Chapter 3 is the detailed discussion of the coupler design for single cell and multiple cells. Chapter 4 presents the experimental results of the measurements carried out on the copper model to verify the design values. Chapter 5 covers the development of code to study the multipacting in the coupler and discussion of results. Chapter 6 covers the study carried out on the niobium material. Chapter 7 concludes the thesis work and presents future scope of the work.

CHAPTER 2

THEORY

2.1] Theory of RF Accelerators

2.1.1] Cavity Fundamentals

To accelerate the charged particle beam having $\beta_g \geq 0.4$ the coupled cavity linear accelerator structure is used. It is made up of chain of cavity resonators where charged particle beam is successively accelerated in each resonator due to the presence of RF electric field. The SC structures are made up of elliptical cavity resonators where individual cavities operate at TM_{010} mode while the structure operates in π -mode that is the phase shift between two adjacent resonators is 180° .

Most of the resonator shapes are derived from the cylindrical or pillbox cavity where the cavity axis coincides with the beam axis. The field distribution of the cavity modes can be easily evaluated by solving wave equation,

$$\nabla^2 \vec{f} - \frac{1}{c^2} \frac{\partial^2 \vec{f}}{\partial t^2} = 0 \quad (1)$$

with appropriate boundary conditions,

$$\hat{n} \times \vec{E} = 0, \hat{n} \cdot \vec{H} = 0 \quad (2)$$

Where, \vec{f} is either electric field or magnetic field. Thus two types of modes viz., Transverse magnetic (TM) and Transverse electric (TE) modes are observed in the cavity. As the name suggests, in TM modes magnetic field is always transverse to the beam axis while in TE

mode electric field is in the transverse direction. The eigen mode having lowest eigen frequency is the TM_{010} ¹ mode that has only two nonzero components viz., longitudinal electric field E_z and azimuthal magnetic field, B_θ (see figure 1). The problem is analytically solvable for pillbox cavity shape, the field distribution of E_z and B_θ is given by,

$$E_z = E_0 J_0(k r) \cos(\omega t) \quad (3)$$

$$B_\theta = \left(-\frac{E_0}{c} \right) J_1(k r) \sin(\omega t) \quad (4)$$

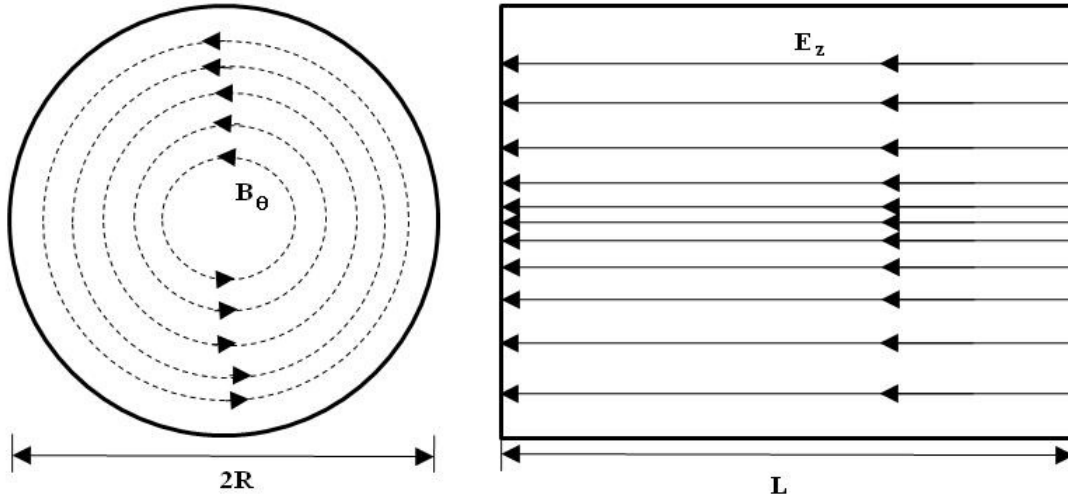


Figure 1: A pillbox cavity of radius, R and length, L showing TM_{010} field components

The root of the Bessel function $J_0(k.r)$ is 2.405 where k is the wave vector and r is the radius vector. A radius 'a' and resonant frequency 'f' of the cavity are related as,

¹ Transverse magnetic modes are denoted by TM_{mnp} where indices m, n and p indicate the number of sign changes of E_z in θ , r and z direction.

$$f = \frac{2.405 c}{2 \pi a} \quad (5)$$

Where ‘c’ is the velocity of light. Thus resonant frequency of TM_{010} mode is inversely proportional to the cavity radius and is independent of the cavity length.

In practice, cavity resonators have more complicated shapes and the wave equation is solved numerically using 2-D code SUPERFISH [20] and 3-D codes HFSS [21], MAFIA [22] and Microwave studio [23]. Figure 2(a) shows the quarter of the elliptical cavity simulated using ‘ELLFISH’ program of SUPERFISH code group and figure 2 (b) shows the 3-D structure simulated using Microwave Studio (MWS).

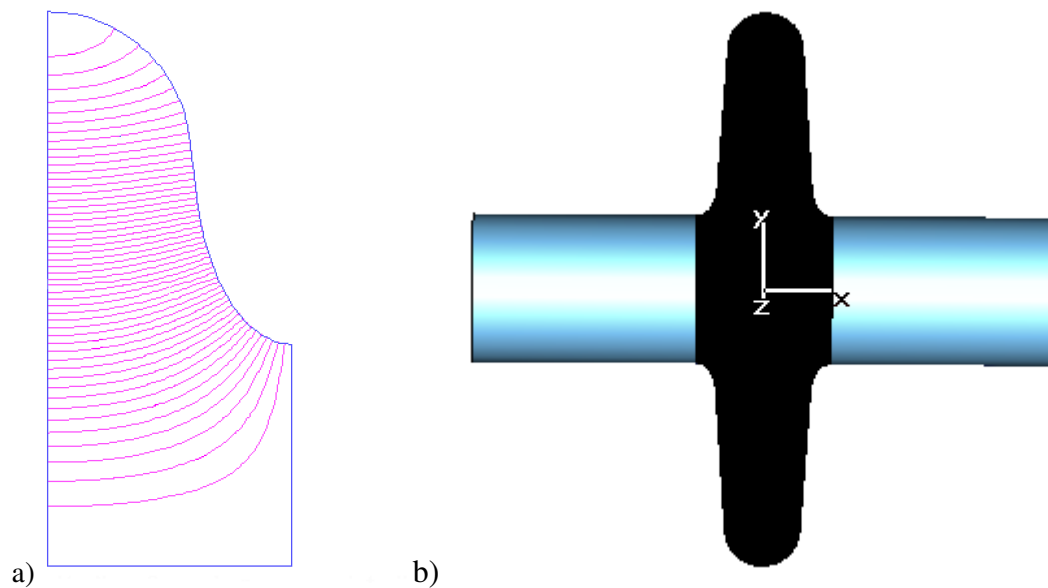


Figure 2(a-b) : Elliptical cavity showing field distribution simulated using SUPERFISH and the 3-D structure simulated using MWS

2.1.2] Figures of Merit

The performance of the cavity resonator is gauged from the Quality Factor (Q_0) of the resonator. It is defined as the ratio of energy stored in the cavity to power dissipated in the cavity in one RF cycle.

$$Q_0 = \frac{\omega U}{P} \quad (6)$$

The time averaged stored energy in the cavity is given by,

$$U = \frac{1}{2} \mu_0 \int_V |\vec{H}|^2 dv = \frac{1}{2} \epsilon_0 \int_V |\vec{E}|^2 dv \quad (7)$$

At RF frequencies the currents flow through the thin surface layer of the cavity walls giving rise to the power dissipation. Even superconductors have a finite surface resistance at RF frequencies. The dissipated power is given by,

$$P = \frac{1}{2} R_s \int_S |\vec{H}|^2 ds \quad (8)$$

$$Q_0 = \frac{\omega \mu_0 \int_V |\vec{H}|^2 dv}{R_s \int_S |\vec{H}|^2 ds} = G / R_s \quad (9)$$

‘G’ is the geometry factor of the cavity that depends only on the shape of the cavity and is useful to compare various cavity shapes.

Shunt Impedance is another physical quantity used to characterize the RF cavity. It is defined as,

$$R = \frac{V_{acc}^2}{P} \quad (10)$$

The ratio R/Q_0 is independent of surface resistance and is given by,

$$\frac{R}{Q_0} = \frac{V_{acc}^2}{\omega U} \quad (11)$$

This quantity is independent of the surface resistance or the size of the cavity and termed as figure of merit. The accelerator cavity shape is optimized so as to obtain high R/Q_0 ratio while minimizing the ratio of E_{peak}/E_{acc} and H_{peak}/E_{acc} . The high surface electric field leads to the field emission while high surface magnetic field leads to the quenching of superconductivity. [24,25]

2.1.3] Transmission line

Electromagnetic (e.m.) waves can propagate through hollow conductor pipe. This concept is used to transfer power at high frequencies. This hollow pipe is called “waveguide”. In microwave transmission, commonly used waveguides are coaxial lines, rectangular tubes and circular tubes. As the waveguide walls are made up of conductor e.m. wave bounces back and forth between them, thus enabling propagation of power or energy. At the end of the guide e.m. wave is absorbed by a load. For complete transmission of power to the load, the characteristic impedance of the waveguide must match with the impedance of the load. The impedance mismatch gives rise to a reflected wave. The vector sum of forward and the reflected wave generate nodes and antinodes of electric/ magnetic field along the length of the waveguide/ transmission line. The amount of mismatch is measured in terms of “voltage standing wave ratio (VSWR)” which is the ratio of maximum to minimum voltage.

For given dimensions of waveguide various electric and magnetic field configurations are possible that are called as “modes”. They are classified into “Transverse Electric (TE)” and “Transverse Magnetic (TM)” type. A particular mode can pass through the waveguide with minimum attenuation only if the wavelength of the wave is less than a critical “cut-off” wavelength. The cut-off wavelength of each mode is different. The mode having longest cut-off wavelength is called the “dominant mode”. In rectangular and circular waveguide, TE_{10} and TE_{11} are the dominant modes respectively. A coaxial line can propagate any frequency including zero frequency.

The choice of transmission line depends on the application. For the transmission of power rectangular waveguides are preferred over the circular as in circular guides there is a possibility of plane of polarization to get rotated through an angle about the axis of the tube. Due to asymmetry such possibility does not exist in rectangular guides. Also, when the dimensions of rectangular guides are chosen such that width of the guide is double the height, the cut-off frequency of next higher modes (TE_{01} and TE_{20}) is double that of dominant mode (TE_{10}). Thus single mode transmission is possible. In case of circular waveguide the cut-off frequencies of dominant mode (TE_{11}) and next higher mode (TM_{01}) are separated by a factor of 1.3. The circular guides with TM_{01} mode are preferred in applications where rotary joints are involved e.g. antenna. [26-30]

The mode of propagation in coaxial lines is “Transverse electromagnetic (TEM)”. The choice between coaxial cable and rectangular waveguide depends on the frequency of operation, power handling capacity, vacuum requirement and applications. A more detail discussion of the same is given in chapter 3. Figure 3 shows the TE_{10} mode in rectangular waveguide and the TEM mode in coaxial line.

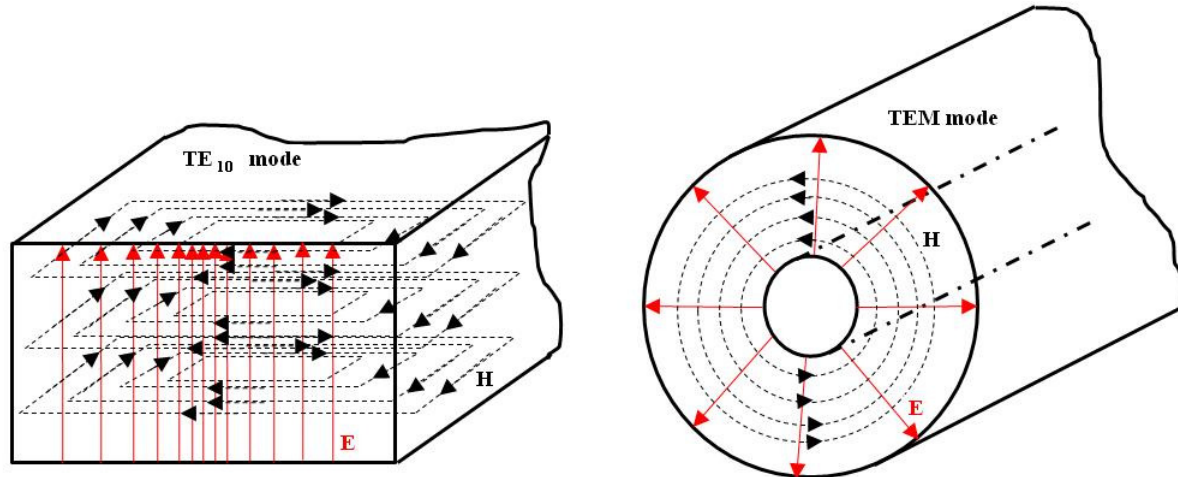


Figure 3 : Field distribution in TE_{10} mode in rectangular guide and TEM mode in coaxial line; electric field is denoted by solid, red (—) line and magnetic field is denoted by dotted, black (---) line

2.2] Basics of Superconductivity

The electrical resistivity of metals and alloys decreases when they are cooled. The current in the conductor is carried by conduction electrons which are free to move through the material. At temperatures above the absolute zero the atoms in the crystal lattice are vibrating about their equilibrium position giving rise to the phonons. Also the foreign atoms or the impurities break the periodicity of the crystal lattice. The scattering of conduction electrons due to phonons and the impurity atoms is the cause of resistivity in the metal. As the temperature is reduced the thermal vibrations are reduced and the contribution due to phonons is reduced. The decrease in resistance is linear up to temperature, $T \sim \theta_D/3$ where, θ_D is the Debye temperature. Below this, resistivity varies as T^5 . Thus ideally for a perfectly pure metal resistivity should approach zero as temperature is reduced towards 0^0 K. On the other hand, the impurity scattering is independent of temperature. Thus certain “residual resistivity” remains even at lowest temperature. [31,32]

Certain metals when cooled show a different behavior; below certain temperature called “transition temperature or critical temperature (T_c)” their resistivity is dropped suddenly, this phenomena is termed as “superconductivity”. Niobium, lead are mainly used for the fabrication of cavity resonators in the superconducting accelerators [33-40]. The wires made up of alloys of niobium like Nb₃Sn, NbTi are used in SC magnets [41-44]. The cuprate based superconductors such as bismuth strontium calcium copper oxide (BSCCO) and Yttrium barium copper oxide (YBCO) have $T_c > 30$ K are termed as high temperature superconductors (HTSC) are being considered for new applications [45].

The fact that superconducting metal has no resistance is strictly true only for the constant DC current. Below transition temperature the conduction electrons divide into two classes viz, “superelectrons” and “normal electrons”. In DC current, the entire current will be carried by superelectrons thus exhibiting zero resistance. When an AC field is applied, the superelectrons will lag behind the field because of the inertia. Hence superelectrons present inductive impedance and because there is now electric field present some of the current will be carried by normal electrons. Thus giving rise to resistance. [25,31,32]

Most of the phenomena in superconductivity are explained by the phenomenological Ginzburg-Landau theory and BCS theory.

2.2.1] BCS Theory

It is a first microscopic theory of superconductivity since its discovery in 1911 proposed by Bardeen, Cooper and Schrieffer in 1957. The theory describes superconductivity as a microscopic effect caused by a “condensation” of pairs of electrons into a boson like state.

An electron moving through a conductor will attract nearby positive charges in the lattice. This deformation of the lattice causes another electron with opposite spin to move into the region of higher positive charge density. The two electrons become correlated forming “cooper pairs”. Figure 4 shows the schematic representation of electron-electron interaction. The \vec{P}_1 and \vec{P}_2 are the momentum before scattering while \vec{P}_1' and \vec{P}_2' are the momentum after scattering while \vec{q} is the momentum of phonon. The momentum is conserved between initial and final state. The relation between all these quantities is as follows,

$$\vec{P}_1 = \vec{P}_1' + \vec{q} \quad (12)$$

$$\vec{P}_2 + \vec{q} = \vec{P}_2' \quad (13)$$

There are a lot of such electron pairs in a superconductor so that they overlap very strongly, forming highly collective condensate. The electrons have spin $\frac{1}{2}$ so they are fermions but cooper pair is a composite boson as its total spin is 0 or 1. Thus the cooper pairs are allowed to be in the same state. The tendency of all cooper pairs to “condensate” into the same ground state is responsible for the peculiar properties of the superconductor. [25,31,32]

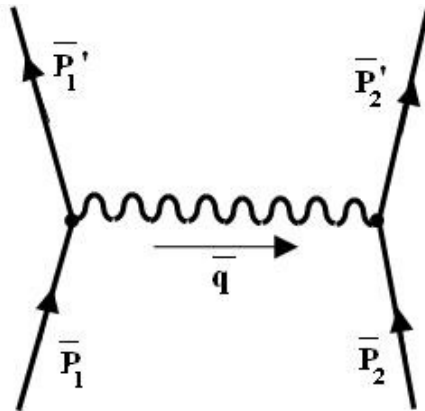


Figure 4: Schematic representation of electron-electron interaction transmitted by phonon

2.2.2] Successes of BCS Theory

1] The electrons are bound in a cooper pairs; these pairs are correlated due to Pauli's exclusion principle. In order to break the pair, one has to change energies of all other pairs. This means that there is energy gap for single particle excitation. The energy gap is highest at low temperature but vanishes at T_c as shown in figure 5. Energy gap, $E_g(0)$ at absolute zero is given by equation(14) which is independent of material.

$$E_g(0) = 2\Delta(0) = 3.5kT_c \quad (14)$$

Near T_c , the temperature dependence of energy gap is given by,

$$\Delta(T) = \Delta(0)\cos\left(\frac{\pi t^2}{2}\right)^{1/2} \quad \text{where } t = T/T_c \quad (15)$$

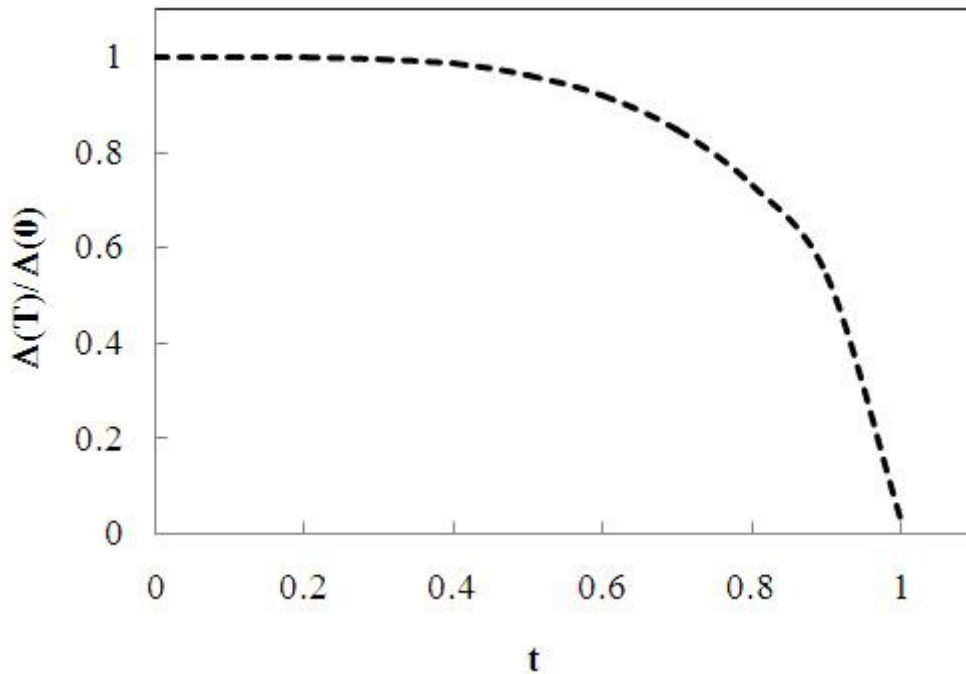


Figure 5: Temperature dependence of energy gap

2] Due to energy gap, the specific heat of the SC is suppressed strongly at low temperature, there being no thermal excitations left. Before reaching the transition temperature, the specific heat of the SC becomes even higher than that of normal conductor and the ratio of these two values is found to be 2.5 universally.

3] BCS theory predicts “Meissner Effect” i.e. the expulsion of a magnetic field from the SC and the variation of penetration depth.

4] BCS theory predicts the variation of critical magnetic field with temperature.

$$H_c(T) = H_c(0)[1 - t^2] \quad \text{where } t = T/T_c \quad (16)$$

5] BCS theory reproduces isotope effect, for a given SC material, critical temperature is inversely proportional to the mass of isotope used.

2.2.3] Ginzburg-Landau(G-L) Theory

It examines macroscopic properties with the aid of thermodynamic arguments. It is called as phenomenological as it describes some of the phenomena of superconductivity without explaining microscopic mechanism.

The free energy, F of a superconducting state differs from that of the normal state. The free energy near the superconducting transition can be expressed in terms of complex order parameter, Ψ . The absolute value of Ψ is connected with the local density of the superconducting electrons, $|\Psi|^2 = n_s$. The free energy in expanded form is,

$$F = F_n + \alpha|\Psi|^2 + \frac{\beta}{2}|\Psi|^4 + \frac{1}{2m^*} |(-i\hbar\nabla - 2e^* \vec{A})\Psi|^2 + \frac{|\vec{B}|^2}{2\mu_0} \quad (17)$$

Where, F_n is the free energy in normal state, α and β are the phenomenological parameters, m^* and e^* are the effective mass and charge of electron while \bar{A} is the magnetic vector potential.

By minimizing the free energy w.r.t. fluctuations in ψ and \bar{A} one arrives at the G-L equations,

$$\alpha\psi + \beta|\psi|^2\psi + \frac{1}{2m^*}(-i\hbar\nabla - 2e^*\bar{A})^2\psi = 0 \quad (18)$$

$$\bar{j} = \frac{2e}{m^*} \text{Re}(\psi^*(-i\hbar\nabla - 2e^*\bar{A})\psi) \quad (19)$$

Equation (18) determines ψ based on applied field and equation (19) provides superconducting current. In the absence of external magnetic field equation (17) reduces to,

$$\alpha\psi + \beta|\psi|^2\psi = 0 \quad (20)$$

The trivial solution of equation (20) is $\psi = 0$ which corresponds to the normal conducting state i.e. temperature $T > T_c$. In the SC state solution is,

$$|\psi|^2 = -\alpha/\beta \quad (21)$$

α is a temperature dependent parameter such that,

$$\alpha(T) = \alpha_0(T - T_c); \quad \alpha_0/\beta > 0 \quad (22)$$

At $T > T_c$, $\alpha(T)$ is positive therefore $|\psi|^2$ is negative which is invalid so the only possible solution is $\psi = 0$. At $T < T_c$, $\alpha(T)$ is negative therefore $|\psi|^2$ is positive therefore solution is,

$$|\psi|^2 = \frac{-\alpha_0(T-T_c)}{\beta} \quad (23)$$

As $T \rightarrow T_c$, $\psi \rightarrow 0$, such a behavior indicates second order phase transition. As per G-L theory, the electrons contribute to superconductivity from superfluid thus $|\psi|^2$ indicates the fraction of electrons that has condensed into superfluid.

The G-L theory predicts the existence of coherence length, $\xi(T)$ and penetration depth, $\lambda(T)$. The coherence length is a size of thermodynamic fluctuation in SC state or in other words it is the natural length scale of spatial variations of ψ . It is defined as,

$$\xi(T) = \left(\frac{\hbar^2}{2m^*|\alpha|} \right)^{1/2} \quad (24)$$

The penetration depth, λ is defined as the depth to which an external magnetic field can penetrate the superconductor. It is given by,

$$\lambda(T) = \left(\frac{m^*}{4\mu_0 e^{*2} \Psi_0^2} \right)^{1/2} \quad (25)$$

Both ξ and λ vary with temperature as $(1-t)^{-1/2}$; where $t = T/T_c$, near transition temperature. The Ginzburg-Landau parameter, κ is defined as,

$$\kappa = \frac{\lambda(T)}{\xi(T)} \quad (26)$$

2.2.4] Type I and Type II Superconductors

The free energy in SC state is lower than normal conducting state. When the external dc magnetic field is turned on, supercurrents flow in the penetration depth to cancel out the fields in the interior. When an external field is equal to the thermodynamic critical field, H_c the two phases are in equilibrium.

$$F_s(H) = F_n = F_n(H=0) + \mu_0 V_s \int_0^{H_c} H dH \quad (27)$$

Consider a SC region near a normal region. At the boundary the flux density penetrates a distance λ into the SC region while the number of super electrons per unit volume increases slowly over the distance ξ . The magnetic contribution raises the free energy by amount $1/2\mu_0 H_c^2 \lambda$ per unit area while the presence of ordered super electrons reduces the free energy by an amount $1/2\mu_0 H_c^2 \xi$. Thus the free energy of the normal- SC interface is $1/2\mu_0 H_c^2 (\xi - \lambda)$ per unit area. If $\xi > \lambda$, then contribution to the surface energy is positive and the G-L parameter, $\kappa < 1/\sqrt{2}$. These types of superconductors are termed as type I. In case of type II superconductors $\xi < \lambda$, so the contribution to the surface energy is negative and the G-L parameter, $\kappa > 1/\sqrt{2}$ (see figure 6). In type II superconductors above lower critical field H_{c1} , the field enters the bulk of superconductor in the form of quantized flux lines called as “vortex”. Each vortex has a single flux quantum and the circulating supercurrent associated with it. The effective radius of normal core is the coherence length. As shown in figure 7, the vortices arrange themselves in the form of a lattice (hexagonal, triangular or square) termed as “flux line lattice (FLL)”. This is called as the “intermediate or mixed state”. This state persists till upper critical field, H_{c2} . Above which the bulk of the superconductor becomes normal conducting. Figure 8 shows the magnetic flux

density versus applied magnetic field of type I and type II superconductors. Table 1 gives the list of parameters of widely used superconductors for SCRF applications like cavities, magnets or thin film applications [46]. Among these Nb has a highest H_{c1} so it is more popular as a cavity material.

In 1963 Saint-James and de Gennes [32] showed that superconductivity persists in a surface layer of thickness $\sim\xi$ of a superconductor in contact with an insulator even beyond H_{c2} . Up to a field H_{c3} surface is superconducting even though bulk of the SC is normal. The value of H_{c3} depends on the angle between surface and the applied field. It is maximum, $H_{c3} = 1.692 H_{c2}$ when field is parallel while it is equal to H_{c2} when field is perpendicular to the surface.

Table 1 : Properties of commonly used superconducting materials for SCRF applications [46,47]

Material	T_c (K)	H_c [T]	H_{c1} [mT]	H_{c2} [T]	$\lambda(0)$ [nm]
Pb	7.2	0.08	-	-	48
Nb	9.2	0.2	170	0.4	40
Nb ₃ Sn	18	~ 0.5	40	30	85
NbN	16.2	~ 0.23	20	15	200
MgB ₂	40	~ 0.32	20-60	3.5-60	140

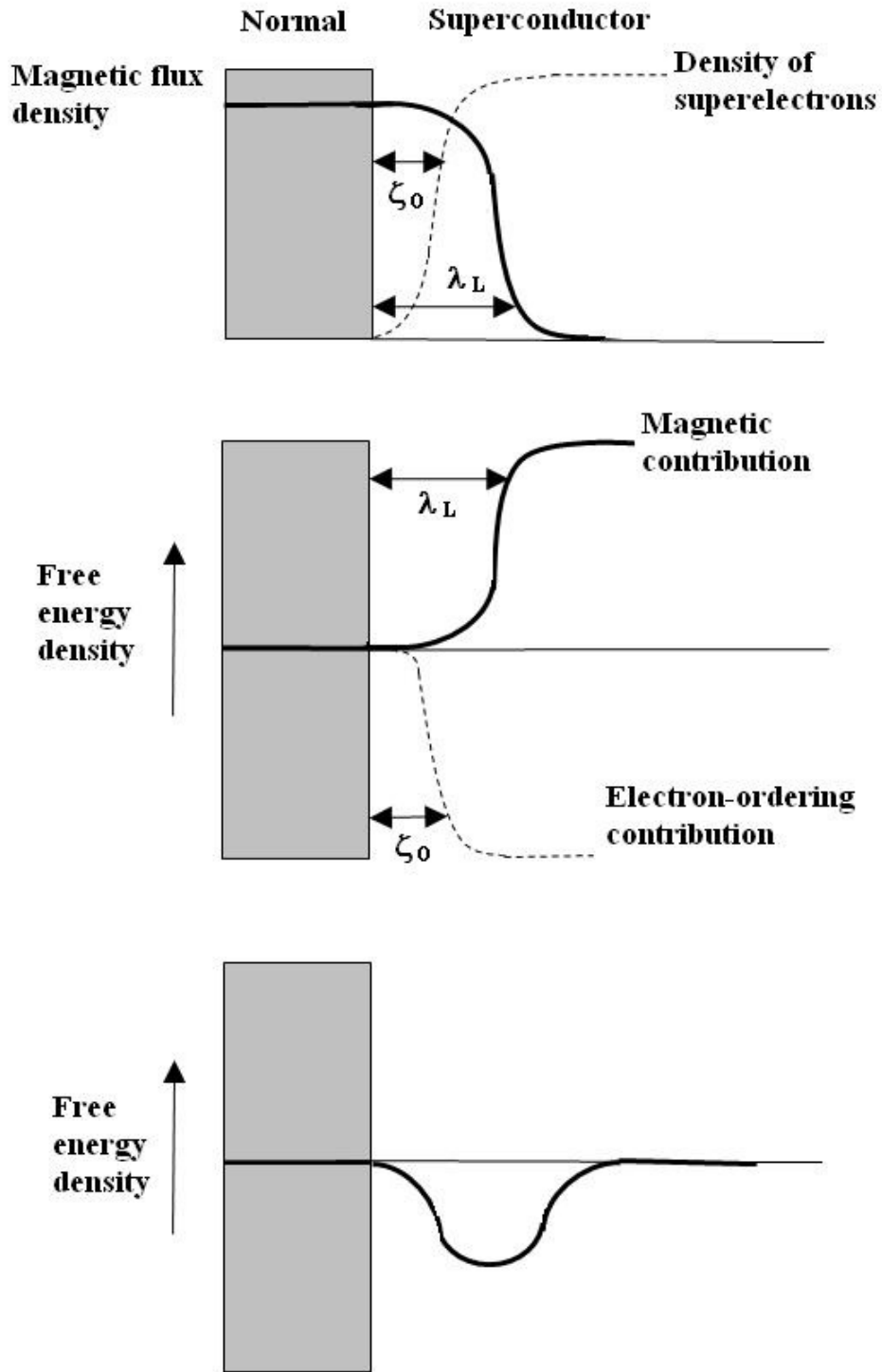


Figure 6: Negative surface energy of type II superconductor. Penetration depth and coherence length (top), contribution to free energy (middle), total free energy (bottom)

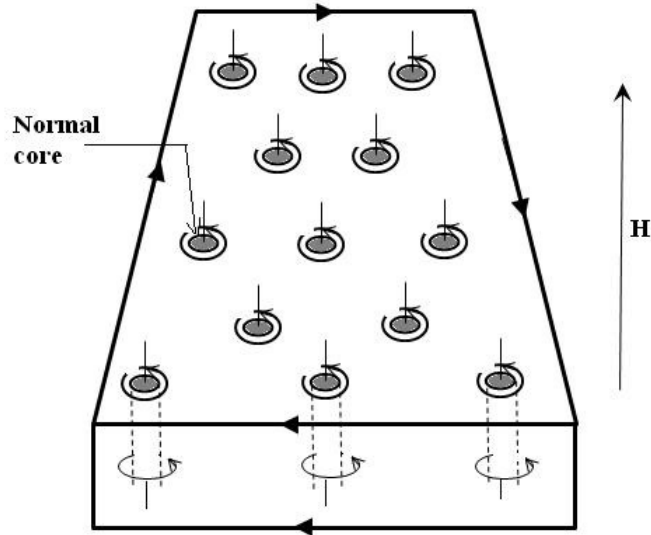


Figure 7 : Representation of mixed state of type II superconductor showing the normal core encircled by supercurrent vortices

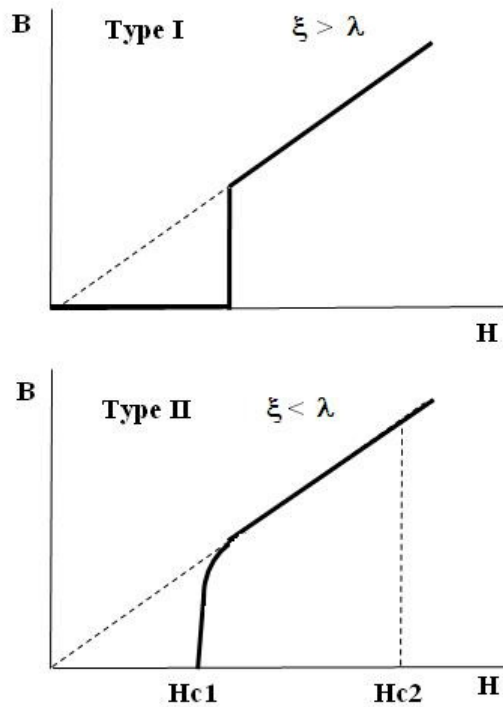


Figure 8 : Magnetic flux density versus applied magnetic field of type I and type II superconductor

2.2.5] Critical Current Density, J_c and Pinning Force, F_p

The critical current density is the maximum resistanceless current that a superconductor can carry. The perfect diamagnetism of a SC arises because in an applied magnetic field, resistanceless surface currents circulate so as to cancel the flux density inside. If the strength of applied magnetic field is increased the shielding currents will also increase. If applied magnetic field reached beyond critical field the shielding current reaches J_c and the superconductivity is lost.

The Lorentz force acting on the vortices due to the critical current and the magnetic flux density, B is given by,

$$F_L = J_c \times B \quad (28)$$

The vortices get trapped/ pinned to the dislocations or impurities present in the bulk of SC. The pinning force is denoted by F_p . When the $F_L \leq F_p$, the vortices are stationary; when F_L exceeds F_p the vortices start moving leading to the dissipation. [32]

2.3] Chemical Processes

The cavities once formed undergo various surface treatments so as to remove the impurities embedded during the fabrication. Various techniques like high pressure rinsing (HPR), buffered chemical polishing (BCP), electropolishing (EP), low temperature baking (LTB) are routinely used. In this section, a brief information about the BCP, EP and LTB is given.

2.3.1] Buffered Chemical polishing, BCP

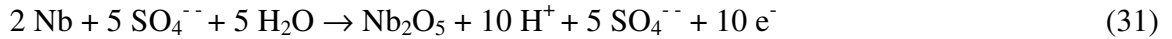
A mixture of nitric acid, hydrofluoric acid and phosphoric acid in ratio 1:1:1 or 1:1:2. The nitric acid oxidizes the niobium, while the fluoric acid removes the oxide according to the following reactions,



These reactions are highly exothermic and the phosphoric acid is used as a buffer to slow down the kinetic of the process. Typical etching rates are 1 – 2 $\mu\text{m}/\text{min}$ and 5 – 7 $\mu\text{m}/\text{min}$ for 1:1:2 and 1:1:1 solutions respectively. The etching rate depends on several factors like temperature, amount of niobium already dissolved in the acid and agitation. [47]

2.3.2] Electropolishing, EP

In this process a constant DC voltage is applied between the anode (niobium sample) and the cathode (aluminum). The mixture of sulfuric acid and hydrofluoric acid is used in 9:1 ratio. The following reactions produce the dissolution of niobium,



The details of the experimental set-up will be discussed in chapter 6. A roughness analysis on niobium samples shows that the EP produces smoother surface than the BCP.[47,48]

2.3.3] Low Temperature Baking, LTB

The samples were baked at low temperature in ultra high vacuum ($>10^{-7}$ torr) either in a vacuum furnace or using heater tapes. The temperature and duration of the baking was maintained at 120°C and 48 hr. for all the samples.

CHAPTER 3

DESIGN OF FUNDAMENTAL POWER COUPLER

3.1] Introduction

In any RF accelerator fundamental power coupler is as important as the cavity itself as it is that part of the accelerator which transmits the RF power from RF source to the accelerator structure. Any mismatch at the coupler can result in loss and reflection of power in the transmission line. This may lead to severe damage of other components present in the line. Also if the sufficient power is not fed to the accelerator then the required field gradient cannot be established. The choice of power coupler is not unique, it varies as per the operating frequency, RF power level and beam current. In addition to this, it is also necessary to ensure multipacting free operation of the coupler at required power level and also the cryogenic heat loads at LHe temperature should be minimized [49].

Most of the couplers that are used for high power operation are built either as coaxial lines with capacitive coupling or the waveguide. A design employed at CERN for the LEP (500 MHz) cavity uses coaxial coupler that can transfer 120 kW power under matched condition. A DC bias to inner conductor suppresses multipacting substantially [50]. Similarly, Cornell CESR(261 kW, 500 MHz) waveguide fixed coupler [51], KEKB (380 kW, 508 MHz) coaxial fixed [52], LEP II (120 kW, 352 MHz) coaxial fixed [53], TRISTAN(200 kW, 509 MHz) coaxial fixed [54], Jlab, FEL (50 kW, 1500 MHz) [55], APT (1 MW, 700 MHz) coaxial variable type [56], SNS (48 kW, 805 MHz) [57], LHC (500 kW, 400 MHz) coaxial variable coupler [58,59] are the existing coupler designs.

Chapter 3 is divided in four subsections. A section (3.2) discusses the crucial parameters to be considered while designing a power coupler for superconducting cavity, section (3.3) is about the computation of external Q using computer codes. The results are computed for 700 MHz and 1.05 GHz cavity using Kroll-Yu method and P. Balleyguier method. The results are compared with the external Q calculated using Microwave Studio. A design of waveguide to coaxial transition is described in section (3.4). A section (3.5) presents the end-cell and coupler design of 5-cell cavity.

3.2] Design Criteria

3.2.1] Choice of the Coupler

Power coupler transmits the power generated by power source to the SC cavity. Two types of couplers can be used viz., waveguide type and co-axial type. Both have some advantages and disadvantages in terms of design, power handling capacity and multipacting. The comparison between two types is as follows, [60, 61]

	Advantages	Disadvantages
Waveguide Type	<ul style="list-style-type: none"> 1] Simple Design 2] Better power handling capacity 3] Higher Pumping Speed 	<ul style="list-style-type: none"> 1] Large Size 2] Difficult to make variable
Co-axial Type	<ul style="list-style-type: none"> 1] Compact 2] Easy to make it variable 3] Multipacting can be suppressed easily 	<ul style="list-style-type: none"> 1] Difficult to cool 2] Complicated Design 3] Smaller pumping speed

The choice of the coupler is made on the basis of operating frequency, source power and the simplicity of design. At lower frequency size of the waveguide is quite large and it is

cumbersome to accommodate it into the cryostat while co-axial type will be compact. On the other hand because of its large size pumping of the entire system through waveguide is possible, also external cooling can be provided easily by brazing cooling channels on the walls of the guide that is essential at high power. A co-axial type is more suitable at lower frequency and lower power levels but the design is quite complicated.

3.2.2] Position of the Coupler

To get the required coupling, position of the coupler w.r.t. cavity is very important. The SC cavity operates in TM_{010} mode where E_z and B_θ are the non-zero field components. In case of cavity coupling generally power is coupled either at the position of maximum electric field or the maximum magnetic field i.e. near the beam hole or near the equator. In SC cavity field levels are much higher ($\sim 10^6$ V/m) therefore coupling hole near the beam hole will enhance the electric field and will cause the multipacting while coupling hole near the equator will enhance magnetic field and it may cause thermal breakdown. Hence position of the coupler is chosen to be on the beam axis of the cavity where the field levels are much lower as compared to the actual cavity.

3.2.3] Choice of Coupling Factor

For efficient coupling of RF power to the accelerator, coupling factor between coupler and cavity has to be unity. Otherwise part of the power will get reflected. The coupling factor, β is defined as,

$$\beta = \frac{Q_0}{Q_{ext}} \quad (33)$$

$$Q_0 = Q_L(1 + \beta) \quad (34)$$

Where Q_0 , Q_L are the unloaded, loaded Q-factors of the cavity whereas Q_{ext} is the Q-value of external circuit (waveguide or transmission line) through which the accelerator is coupled to the source. The power flow to the accelerator is maximum when source is matched or critically coupled ($\beta=1$ or $Q_0 = Q_{ext}$) to the load i.e. accelerator. Under the situation when $\beta < 1$ (undercoupled) or $\beta > 1$ (overcoupled) the system is mismatched, power is reflected back.

3.2.4] Effect of Beam loading

A case where load impedance remains constant it is easy to design power coupler but in case of linac load varies with time. In this situation design of power coupler is complex. The net impedance seen by generator varies with beam current (or power) hence the coupling coefficient [25,61]. Thus while designing the coupler, the system must be evaluated under various conditions viz.,

1. The value of β , under no beam condition
2. The value of β , under full beam condition
3. The value of β , under different beam powers

The exact relation for the Q-value in terms of cavity and beam parameters is given by [62],

$$Q = [\beta_p (\lambda/2) E] / [2 (r/Q) I \cos \phi] \quad (35)$$

Upon considering all the advantages and disadvantages with different coupler types a general scheme for the present SC cavity was worked out that uses both waveguide and coaxial coupler. A Power generated by power source is carried by waveguide up to the cryostat. Inside the cryostat a coaxial antenna is used to feed power to the cavity. The coaxial coupler is a rigid transmission line having vacuum/ air as a dielectric. Its dimensions are chosen such that the

characteristics impedance of the line is 50Ω . The coupler port is situated on the beam pipe of the cavity. The junction between waveguide and coaxial coupler is to be carefully designed to ensure loss-free transition that is a “door-knob transition”. The schematic of the power coupler for SC cavity is shown in figure 9.

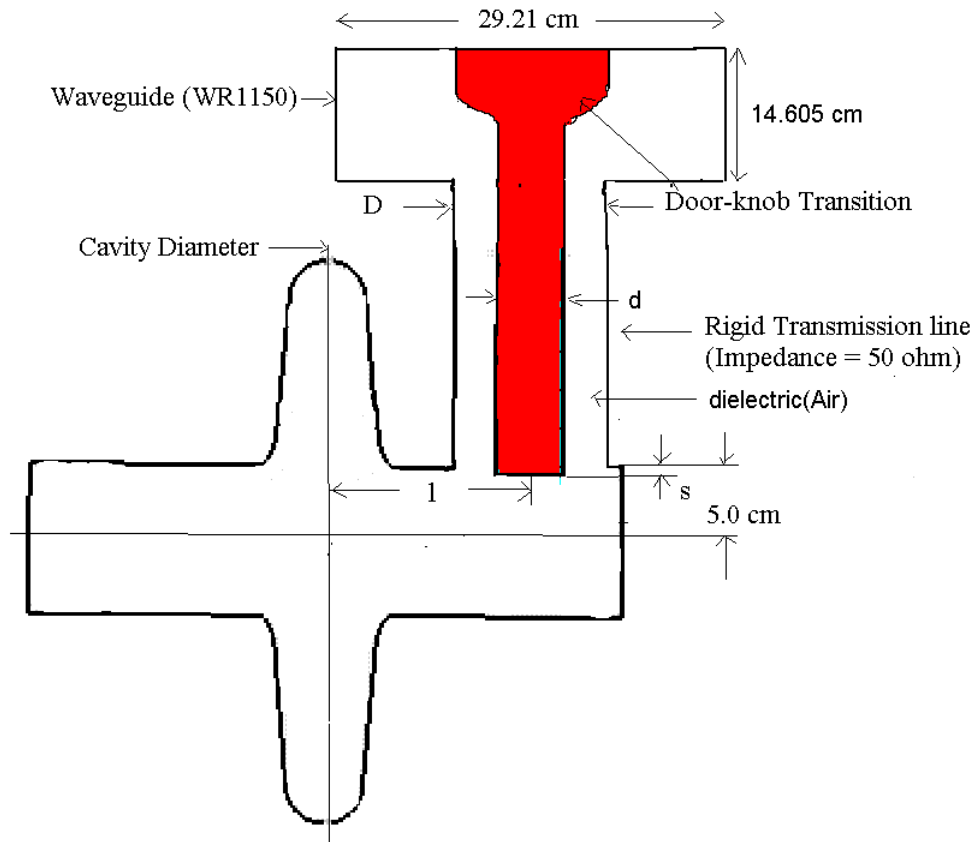


Figure 9: Schematic of SC Cavity with Power Coupler

As an initial step the single cell, elliptical cavities are designed. Two frequencies viz., 700 MHz and 1.05 GHz are chosen for the SC cavity which are the second and third harmonics of the operating frequency (350 MHz) of ADS linac [13]. The optimized cavity parameters of a single,

elliptical cavity designed for 700 MHz and 1.05 GHz [14,15,63] are summarized in table 2. The further sections will discuss the coupler design for these two cavities in detail.

Table 2: Optimized parameters of single, elliptical cavity

Parameters	Design Value	
Frequency	700 MHz	1.05 GHz
β	0.42	0.49
Cavity Diameter	37.38 cm	25.18 cm
Cavity Length	9.0 cm	7.0 cm
Bore Radius	5.0 cm	4.0 cm
Beam pipe length	15.0 cm	15.0 cm
Q_0	$6.1 \times 10^8 @ 4.2 \text{ K}$	$4.2 \times 10^8 @ 4.2 \text{ K}$
r/Q_0	8.3	8.45
Geometric factor, G	122.4 Ω	141.4 Ω

3.3] Computation of External Q

To get the optimum coupling, the parameters that need to be optimized are the coupler dimensions: outer conductor diameter (D) and inner conductor diameter (d), beam pipe radius, penetration depth (s) and position of the coupler w.r.t. cavity center (l) on the beam pipe as shown in figure 9.

A] Coupler Dimensions, D and d: The power handling capacity of the co-axial cable increases with physical dimensions. The average power flow at which multipacting occurs was found to scale as the dimensions of the coaxial line [64]. Thus coupler dimensions can be adjusted so as to

push the threshold of low-order multipacting above the operating voltage. The detailed discussion of the multipacting in coaxial coupler is given in Chapter 5.

B| Beam Pipe Radius: Since the coupler is connected to the beam pipe the size of the beam pipe affects the coupling and hence the coupling coefficient. The magnitude of the fields present in the beam pipe increases with increase in beam hole size and hence it enhances the coupling but at the same time larger beam hole reduces the cavity shunt impedance and hence the accelerating gradient. Also the ratio of peak electric field and peak magnetic field to the accelerating field increases with bore radius that increases the chances of multipacting in the cavity limiting the cavity performance.

C| Coupler Position, l: Since the electric and magnetic field gradients are quite high ($\sim 10^6$ V/m) in the SC cavity, the coupler is connected to the beam pipe unlike the normal conducting structures where coupler is directly mounted on the cavity. Thus position/ distance of the coupler from cavity will affect the coupling. The farther the coupler from the cavity lesser is the coupling at a given penetration depth of the antenna.

D| Effect of Penetration Depth, s: The strength of the coupling depends on the penetration of antenna inside the beam pipe. The coupling improves with the insertion of antenna inside the beam pipe.

As discussed in sub-section (3.2.3) to ensure maximum power transfer to the cavity the coupling coefficient between the power coupler and the cavity should be unity i.e. $Q_0 \cong Q_{\text{ext}}$. The external Q, Q_{ext} is the geometrical factor of the coupler and does not depend on the material used or the temperature at which the measurement was carried out. Thus to optimize the coupler parameters, effect of various coupler and cavity parameters on the external Q was studied.

The first step in the coupler design is the computation of Q_{ext} . Various methods have been developed for the evaluation of coupling factor. e.g. S-parameter calculation using Transient analysis, Kroll-Yu method, Pascal Balleyguier Method which are based on the Eigen Mode analysis [62,65,66]. The P. Balleyguier method requires knowledge of electric/magnetic field at the position of open/short accurately thus the accuracy of results depends on the mesh size [67]. The subsection (3.3.1) discusses Kroll-Yu method and its optimization to evaluate high external Q, subsection (3.3.2) describes the P. Balleyguier method, subsection (3.3.3) shows the validation of Kroll-Yu method while subsection (3.3.4) shows the comparison between different computational methods

3.3.1] Kroll- Yu method

A number of computer programs viz., MAFIA, SUPERFISH, URMEL have been developed for the design of a cavity resonators which give information about the field distribution, shunt impedance, Q-value but cannot calculate Q-value due to external coupling due to waveguide/ co-axial line. Thus Kroll-Yu in 1990 developed a procedure to calculate external Q by using these codes.

Slater had studied combined behavior of (cavity + waveguide) system by inserting terminating short at the waveguide end. He found the relation between line resonant frequency and the cavity resonant frequency of the structure [68] as follows,

$$\tan (2\pi l/\lambda_g) = \Sigma 1/Q_{\text{ext}} (\omega/\omega_r - \omega_r/\omega) \quad (36)$$

Where, 'l' is the length of waveguide, ' λ_g ' is the guide wavelength and ' ω_r ' is the resonant frequency of cavity.

Though this equation is fundamental equation to study the coupling in cavities, it is not suitable in its present form for direct evaluation of Q_{ext} .

Kroll-Yu suggested an alternate method [69] that is similar to Slater's method but better suited for computer application. A (cavity + waveguide) system terminated in a short (tangential electric field component, 'E_t' is zero) can be treated as two coupled resonators, cavity and waveguide as shown below in figure 10.

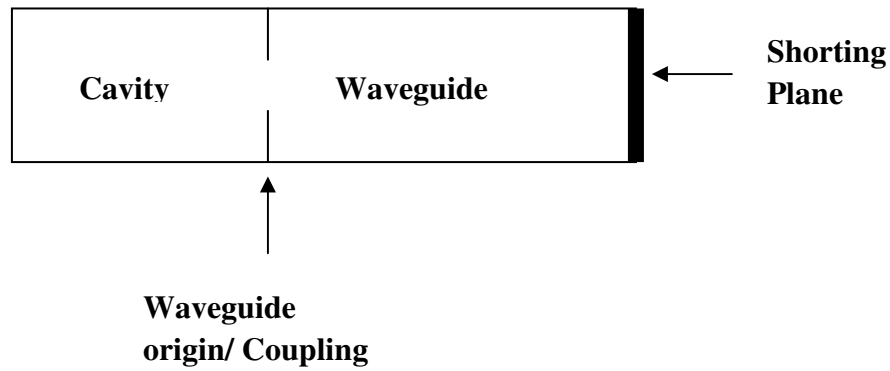


Figure 10: Schematic of cavity and coupler as a coupled resonators

The formulation deals with frequency, ω , as a function of phase change along the guide length, ψ given by $2\pi D/\lambda_g$ where λ_g is the guide wavelength and D is the guide length. A quantity $G \equiv -(1/2) (d\psi/d\omega)$ plotted as a function of ω exhibits a typical resonance curve with peak at the resonant frequency of (cavity + waveguide) system feeding into a matched load. When multiplied by the resonant frequency, the height of the curve is equal to Q_{ext} . The eigen modes of this system are complex in nature viz, $u + i v$. Also,

$$G \equiv -(1/2) (d\psi/d\omega) = (1/2) (v/(w-u)^2 + v^2) + (1/2) \chi'(u) \quad (37)$$

This is resonant curve at frequency $\omega=u$ and $Q_{\text{ext}}=(1/2)(u/v) + (1/2)\chi'(u)$

A] Implementation formulae: The exact relation between ψ and ω is given by 4 – parameter formula,

$$\psi(\omega) = \tan^{-1}[v/(\omega-u)] - \chi(\omega) + n\pi \quad (38)$$

$$\text{where , } \chi(\omega) \cong \chi(u) + \chi'(u) (\omega-u)$$

By using simulation codes like MAFIA, Microwave Studio, HFSS one can obtain different ψ - ω pairs (data points) for different values of waveguide length, D. The essence of the method is to fit data points by four parameter formula. The fitted values of u and v give information about the resonant frequency and external Q value. Also it is observed that for $Q > 20$, choice of $\chi'(u)$ equal to zero is excellent. Thus for determination of u and Q_{ext} just three points are sufficient (3-parameter fit).

The data points are denoted by (ψ_i, ω_i) , $i=1,2,3$. From equation (38),

$$\psi(\omega_i) + \chi(u) + \chi'(u) (\omega_i-u) = \tan^{-1}[v/(\omega_i-u)] \quad (39)$$

Taking the difference of the above for $i=1$ and $i=2$ yields

$$\psi_1 - \psi_2 + \chi'(u) (\omega_1 - \omega_2) = \tan^{-1}[v/(\omega_1-u)] - \tan^{-1}[v/(\omega_2-u)] \quad (40)$$

Rearranging and using trigonometric identity,

$$(\omega_1 - \omega_2) \cot[\psi_1 - \psi_2 + \chi'(u) (\omega_1 - \omega_2)] = -v - (\omega_1 - u) (\omega_2 - u) / v \equiv B_{12} \quad (41)$$

Thus it is seen that B_{12} is completely determined by data points. Choice of $\chi'(u)$ is arbitrary.

Analogously B_{23} is defined. Let

$$A \equiv B_{12} - B_{23} / \omega_3 - \omega_1 = (\omega_2 - u) / v \quad (42)$$

Thus u , v and $\chi(u)$ are,

$$u = \omega_2 + A B_{12} + \omega_1 A^2 / (1 + A^2) \quad (43)$$

$$v = (u - \omega_1) A - B_{12} \quad (44)$$

$$\chi(u) = \tan^{-1}[v/(\omega_1 - u)] - \psi_i - \chi'(u) (\omega_1 - u) \quad (45)$$

Setting $\chi'(u)$ to zero, three parameter fit of the resonance curve is obtained.

Fitted values of frequency and Q_{ext} are obtained by using above implementation formulae for the given set of data points (ψ_i, ω_i) . In the present analysis, resonant frequency and external Q are obtained by 3- parameter fit of the data points. The next sections describe the optimization of the Kroll-Yu method with the simulation results for 700 MHz cavity. The simulations are carried out using Microwave Studio (MWS).

B] Optimization of Evaluation Procedure: Figure 11 shows the behavior of (cavity + coupler) system as a function of position of the short. Cavity mode (TM_{010}) frequency did not change much whereas the coupler mode (TEM) frequency changed appreciably as a function of position of the short. It was observed that values of fitted parameters (f and Q_{ext}) were greatly affected by the choice of the data points. It was observed that data points in the vicinity of a point where cavity resonance frequency and the line frequency were nearly same, provided consistent results. So for further evaluation points in the shaded portion indicated in figure 11 were chosen. Table 3 shows the variation of fitted ' f ' and ' Q_{ext} ' for various sets of data points picked up from the same curve.

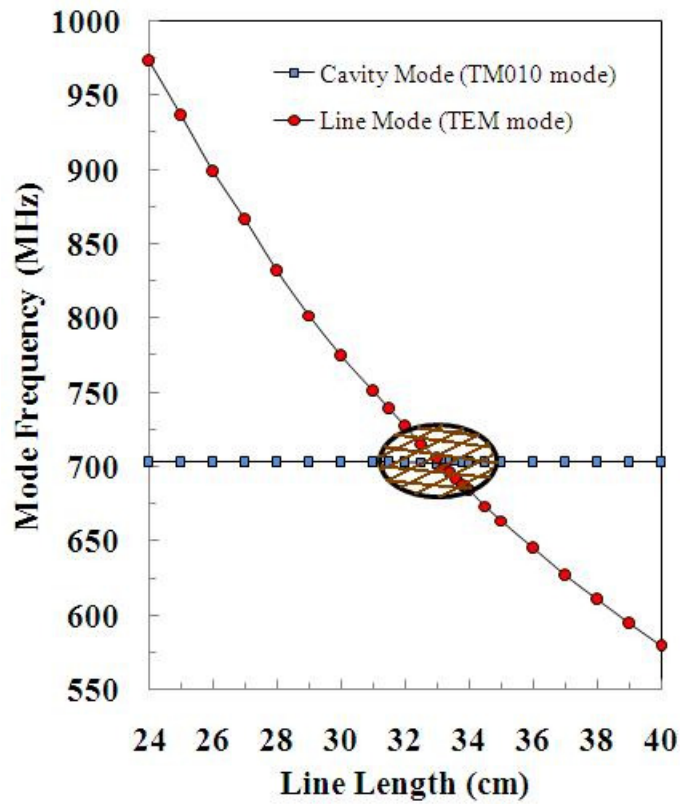


Figure 11: Study of mode frequencies as a function of position of short

Table 3: Fitted Frequency and Q_{ext} Data

No.	Line length Data [m]	Frequency data [MHz]	Fitted Parameters	
			Frequency[MHz]	Q_{ext}
1.	0.24, 0.25, 0.26	703.318, 703.316, 703.313	703.324	61334.1
2.	0.332, 0.334, 0.336	703.950, 703.623, 703.516	703.306	19177.7
3.	0.38, 0.39, 0.40	703.338, 703.333, 703.330	703.322	53547.3

C] Optimization of mesh : The effect of mesh size on the evaluation of Q_{ext} was studied. To reduce the evaluation time, symmetry plane at $z=0$ (XY-plane) with boundary condition $H_t=0$

was introduced as shown in figure 12. The number of meshnode of half problem geometry was varied from about 6000 to 3×10^5 . The change in the Q_{ext} was negligible. [See table 4]

Table 4: Effect of Mesh Size on Q_{ext}

No.	Meshnodes	Q_{ext}
1.	14985	1.614×10^6
2.	35280	1.542×10^6
3.	75348	1.800×10^6
4.	123120	1.280×10^6
5.	181288	1.281×10^6
6.	302293	1.440×10^6

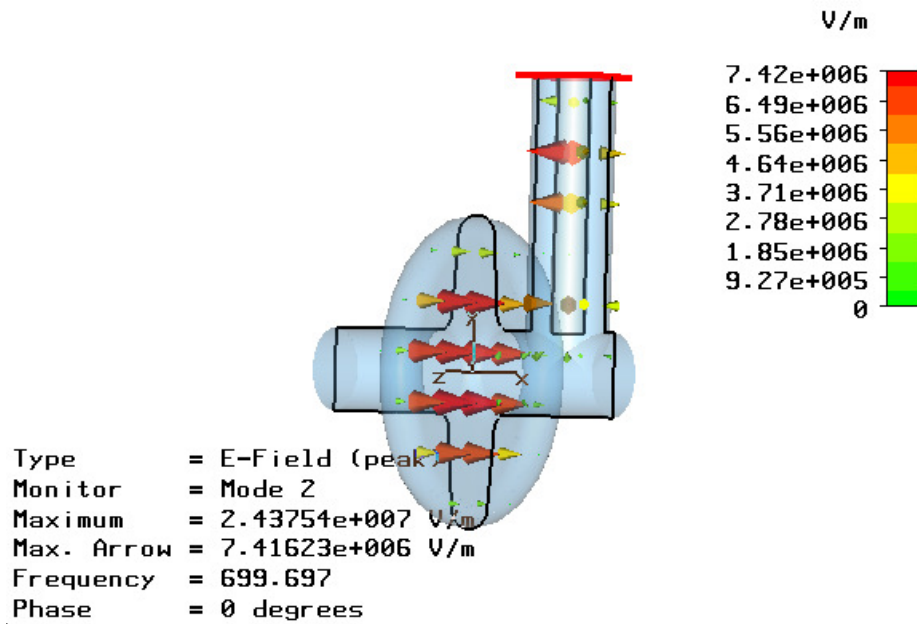


Figure 12: Microwave Studio Output of Simulated Structure

3.3.2] P. Balleyguier method

This method is one of the most widely used methods for the evaluation of external Q that is based on the evaluation of electric and magnetic field at the end of the coupler. A brief description of the method is given below [62,70].

Consider a cavity resonator connected to a transmission line and is resonating at frequency ‘ ω ’. The cavity is driven at a power ‘P’ and the stored energy in the resonator is ‘W’ the external Q is given by,

$$Q_{ext} = \omega W / P \quad (46)$$

Under the assumption that single mode viz TEM is traveling through the transmission line, P and W is given by,

$$P = \frac{1}{2\eta} \oint_{surf} |E|^2 ds = \frac{1}{2\eta} \oint_{surf} |H|^2 ds \quad (47)$$

Where, η is the mode impedance and it is equal to $(\mu_0/\epsilon_0)^{1/2}$ with vacuum as dielectric.

$$W = \frac{1}{2} \iiint_{vol} \epsilon_0 |E|^2 dv = \frac{1}{2} \iiint_{vol} \epsilon_0 |H|^2 dv \quad (48)$$

Substituting (47) and (48) in (46) external Q, Q_{ext} is given by,

$$Q_{ext} = \frac{\omega \iiint_{vol} |F|^2 dv}{c \oint_{surf} |F|^2 ds} \quad (49)$$

Where, F is either electric (E) or magnetic (H) field. Computation of external Q is not feasible using eigen mode solvers. Thus, P. Balleyguier developed the method to compute the external Q using the eigen mode solvers.

Consider a situation where the incident and reflected waves add inside the cavity volume and have an arbitrary phase difference, ϕ and a pure standing wave exists inside cavity and a line. A new quantity, Q_1 is defined such that,

$$Q_1 = \frac{\omega \iiint_{vol} |E_1|^2 dv}{c \iint_{surf} |E_1|^2 ds} = \frac{|1 + e^{i\phi}|^2}{4} Q_{ext} \quad (50)$$

The Q_1 can be computed numerically by any cavity code by terminating the line with perfect magnetic wall. Similarly if we terminate the line with perfect electric field then the physical situation is where the fields inside the cavity are subtracting and a quantity Q_2 can be defined,

$$Q_2 = \frac{\omega \iiint_{vol} |H_2|^2 dv}{c \iint_{surf} |H_2|^2 ds} = \frac{|1 - e^{i\phi}|^2}{4} Q_{ext} \quad (51)$$

The external Q is given by the addition of Q_1 and Q_2 .

$$Q_{ext} = Q_1 + Q_2 \quad (52)$$

In short, the computation of external Q needs two runs of MAFIA/ Microwave Studio or any other eigen mode solver one with the perfect electric field and the other with magnetic field as a boundary condition.

A1 Evaluation of Q_{ext} using P. Balleyguier method using Microwave Studio: The original method developed by Pascal makes use of the MAFIA code. V.Shemelin and S.Belomestnykh [67] have used the same method using Microwave Studio. To calculate the Q_{ext} , a cavity with coaxial input

coupler is modeled as shown in figure 12. A coupler with finite length is used. Two runs of Microwave studio with perfect electric field and perfect magnetic field at the coupler end are required for the evaluation². The coupler dimensions are chosen such that characteristic impedance is 50 Ω .

The coaxial coupler operates in a transverse electromagnetic (TEM) mode. It has only two non-zero components viz., radial electric field (E_r) and azimuthal magnetic field (H_ϕ). Figure 3 in Chapter 2 shows the coaxial coupler with propagating TEM mode.

The characteristics impedance, Z_0 of the coaxial line having inner conductor radius, 'a' and outer conductor radius, 'b' operating in TEM mode is given by,

$$Z_0 = 60 \ln\left(\frac{b}{a}\right) \quad (53)$$

Let 'P' be the total power transferred through the coupler.

$$P = I^2 R = \frac{V^2}{R} \quad (54)$$

Therefore peak electric and magnetic field can be written in terms of voltage and current as follows,

$$V = E r \ln\left(\frac{b}{a}\right) \quad (56)$$

² Microwave Studio normalizes the fields at a given frequency such that stored energy in the cavity is 1 J.

$$I = 2\pi r H \quad (57)$$

By applying perfect magnetic boundary condition at the coupler end, electric field at coupler end is obtained. By using formula given by equation 56, voltage and hence the power through the coupler can be calculated. Using equation 46, Q_1 can be estimated.

Similarly, by applying perfect electric boundary condition at the coupler end, magnetic field at coupler end is obtained. By applying equation 57, the current and hence the power through the coupler and Q_2 can be evaluated. Thus two runs of the MWS are enough to evaluate Q_{ext} at a given penetration of the inner conductor for an arbitrary length of the coaxial line.

3.3.3] Validation of Kroll-Yu Method

To check the validity of Kroll-Yu method over the wide range of Q_{ext} values, the calculations were carried out for the pill box cavity and compared with the P. Balleyguier method. The calculations were carried out for the benchmark cavity [70] operating at 1146 MHz having diameter ~200 mm and length ~150 mm with semi-rigid coaxial line of ID: ϕ 1.65 mm and OD: ϕ 5.35mm. The penetration depth was varied from 0 to 5.5 cm [70,71]. To evaluate external Q using Kroll-Yu method for the penetration depth of 0 to 2.0 cm, data points near the resonance frequency of the cavity were used whereas for the penetration depth from 2.5 cm to 5.5 cm points far away from the cavity resonance frequency give the accurate answers. Table 5 shows the comparison of Q_{ext} values computed using Kroll-Yu method and P. Balleyguier method for a pill box cavity.

Table 5: External Q calculation of Pill Box Cavity

Penetration Depth (mm)	External Q, Q_{ext}	
	P. Balleyguier Method [70]	Kroll-Yu Method
0	6068050	3553030
2.5	407113	269016
5.0	81493	74439
7.5	23841	28111
10	10536	12086.1
12.5	5361	4449.1
15	2790	2660.16
17.5	1682	1709.18
20	1064	1061.46
25	455	482.99
30	207	232.46
35	106	118.52
40	56.5	61.87
45	33	34.15
50	19.9	20.36
55	13.1	13.87

3.3.4] Comparison of different computational methods

External Q was computed for the cavity operating at 1.05 GHz having coaxial coupler of ID: ϕ 34.78 mm ; OD: ϕ 80 mm placed at a distance of 120 mm from the cavity center using Kroll-Yu method and P. Balleyguier method (see table 6). Similar calculations were carried out

for a cavity designed at a resonant frequency of 700 MHz having coaxial coupler of ID: ϕ 43.48 mm; OD: ϕ 100 mm connected at a distance of 120 mm from the cavity center (see table 7).

Table 6: Comparison between P.Balleyguier method and Kroll-Yu method 1.05 GHz Coupler

Penetration Depth ³ (mm)	External Q, Q_{ext}	
	P.Balleyguier Method	Kroll-Yu Method
-20	3.69×10^7	5.13×10^7
-10	8.66×10^6	1.81×10^7
00	3.04×10^6	2.68×10^6
10	1.08×10^6	1.91×10^6
20	4.86×10^5	7.19×10^5

Table 7: Comparison between P.Balleyguier method and Kroll-Yu method 700 MHz Coupler

Penetration Depth (mm)	External Q, Q_{ext}	
	P.Balleyguier Method	Kroll-Yu Method
-20	4.3×10^6	4.04×10^6
-10	1.31×10^6	1.45×10^6
0	5.95×10^5	6.37×10^5
10	4.0×10^5	2.72×10^5
20	2.21×10^5	1.06×10^5

The new version of Microwave Studio (MWS, Version 10) contains a module to evaluate external Q directly. Figure 13 shows the variation of Q_{ext} as a function of penetration depth

³ The negative sign of penetration depth indicates that antenna (inner conductor) is pulled inside the coupler

calculated for the cavity operating at 1.05 GHz using P.Balleyguier , Kroll-Yu method and MWS. There is a discrepancy in the results at very high $Q_{\text{ext}} (> 10^7)$ values while at lower values it is matching well. Similar results were observed for 700 MHz cavity.

Kroll-Yu method is based on the frequency difference as a function of the coupler length, thus at high Q_{ext} , the frequency change, df due to change in coupler length, $d\psi$ is very small. Thus error in the calculation is high when the Q_{ext} is high. The results calculated by Pascal method depend on the accuracy of the electric and magnetic fields calculated at the boundary. The MWS calculates the external Q from the complex poles of the S-parameters space. The code assumes lossless structure.

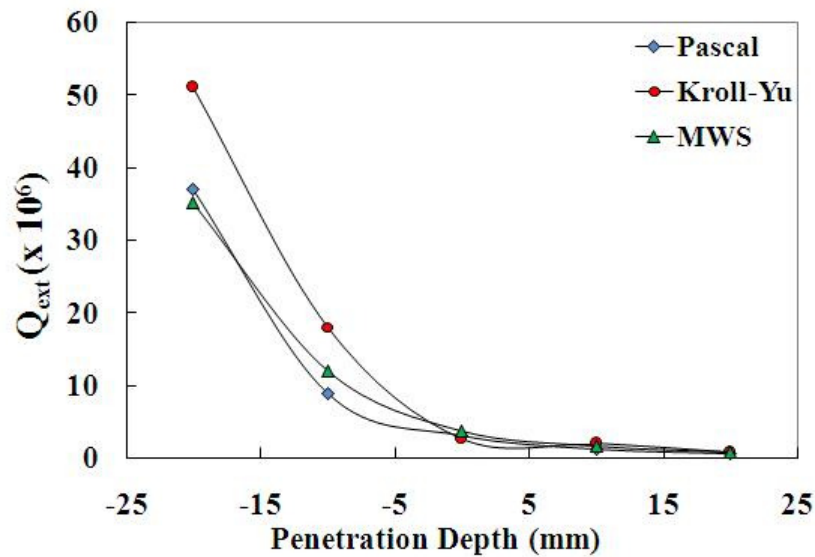


Figure 13: Comparison of external Q evaluated using Pascal, Kroll-Yu and MWS module for a 1.05 GHz cavity

3.3.5] Results and Discussion

Upon taking into account the beam loading requirements, the required external Q for perfect matching is $\sim 1.5 \times 10^6$ (phase angle $\sim 30^\circ$). The change of Q_{ext} with coupler position and

penetration depth is shown in figure 14 and 15 respectively of 700 MHz cavity having coupler ID: 43.48 mm and OD: 100 mm [14].

The coupler optimization of the 1.05 GHz cavity required the comparison between different coupler sizes viz., coupler I (ID: 20.24 mm and OD: 46.56 mm), coupler II (ID: 34.48 mm and OD: 80 mm) and coupler III (ID: 43.48 mm and OD: 100 mm). Also the optimization of the beam pipe radius was carried out as the designed beam port radius was smaller in size viz. 40 mm [15, 16].

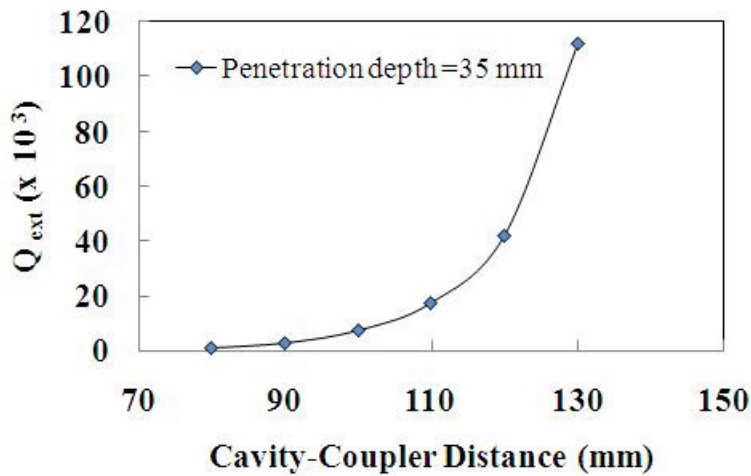


Figure 14: Effect of coupler position, (f = 700 MHz)

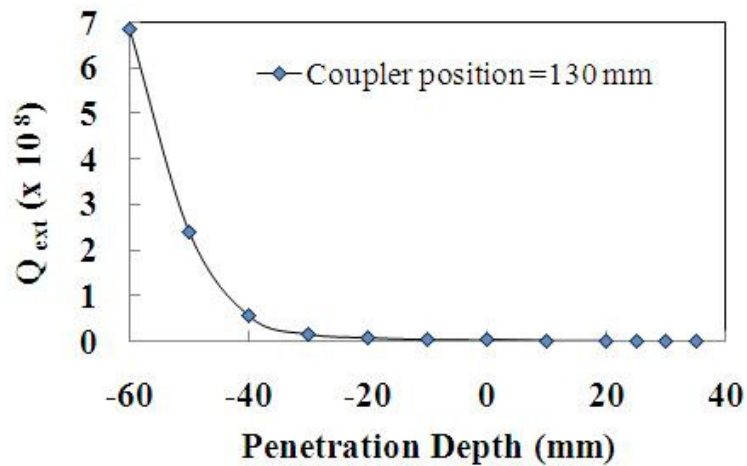


Figure 15: Effect of coupler penetration depth, (f = 700 MHz)

A| Effect of Coupler Dimensions: Studies were carried out for the cavity having beam pipe radius of 40 mm with two couplers viz, coupler I & II. It is clear from figure 16 that for the same penetration depth, larger coupler gives lower Q_{ext} that is better coupling.

B| Effect of Cavity-Coupler Distance: Simulations were carried out for cavity having beam pipe radius 40 mm and coupler II at a penetration depth of 20 mm. By changing coupler distance from 85 mm to 120 mm, Q_{ext} varied from 1.776×10^4 to 9.056×10^5 . Thus coupling reduces with the increase in distance. (see figure 17)

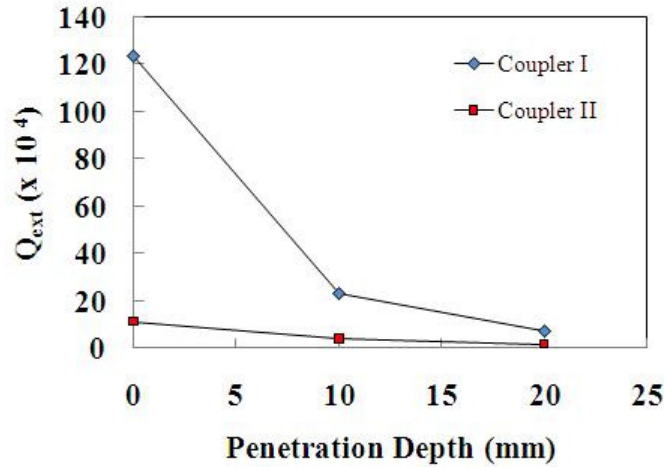


Figure 16: Effect of coupler size, ($f = 1.05$ GHz)

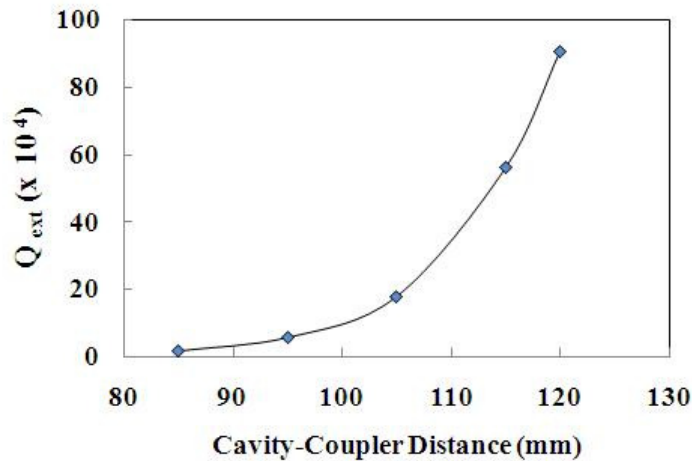


Figure 17: Effect of distance between cavity and coupler, ($f = 1.05$ GHz)

C| Effect of Penetration Depth: The penetration depth was varied from -10 mm to 40 mm and its effect on Q_{ext} was studied at a beam pipe radius of 40 mm, 50 mm and 70 mm. The cavity-coupler distance was 120 mm. The Q_{ext} reduces and hence the coupling improves with the larger penetration as shown in figure 18.

D| Effect of Beam Pipe Radius: The effect of beam pipe radius was studied by enlarging the beam pipe after a distance of ~20 mm from the cavity end. The beam pipe radius was varied from 40 mm to 90 mm. The optimum coupling was obtained for the beam pipe of radius 70 mm as shown in figure 19.

From figure 18, it is clear that to get required coupling without changing the beam pipe radius and coupler size, penetration of ~20 mm is required. Upon optimization of all the parameters, required Q_{ext} was obtained at smaller penetration. The optimized parameters are listed in table 8.

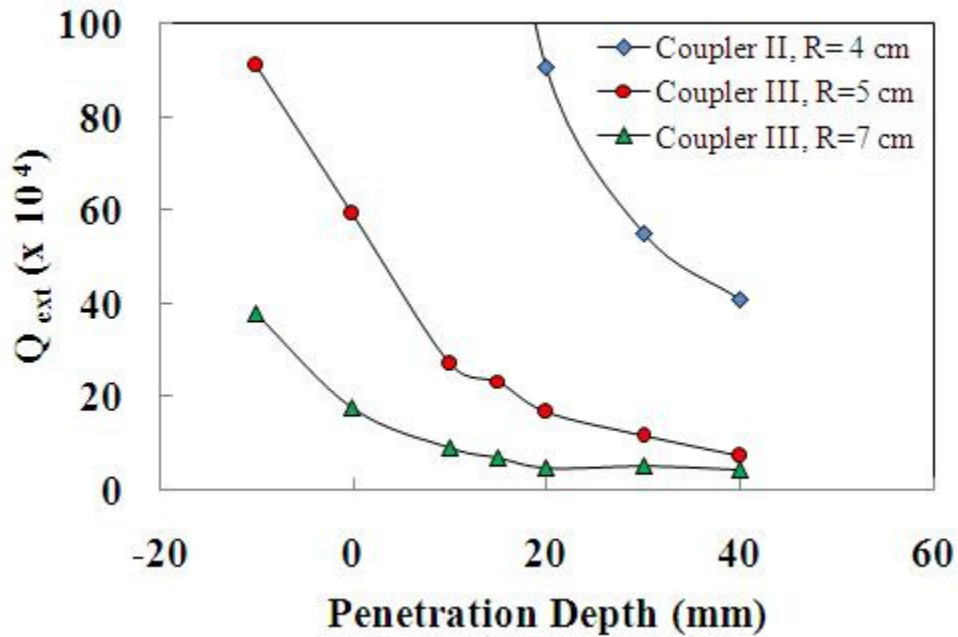


Figure 18: Effect of penetration Depth, ($f = 1.05$ GHz)

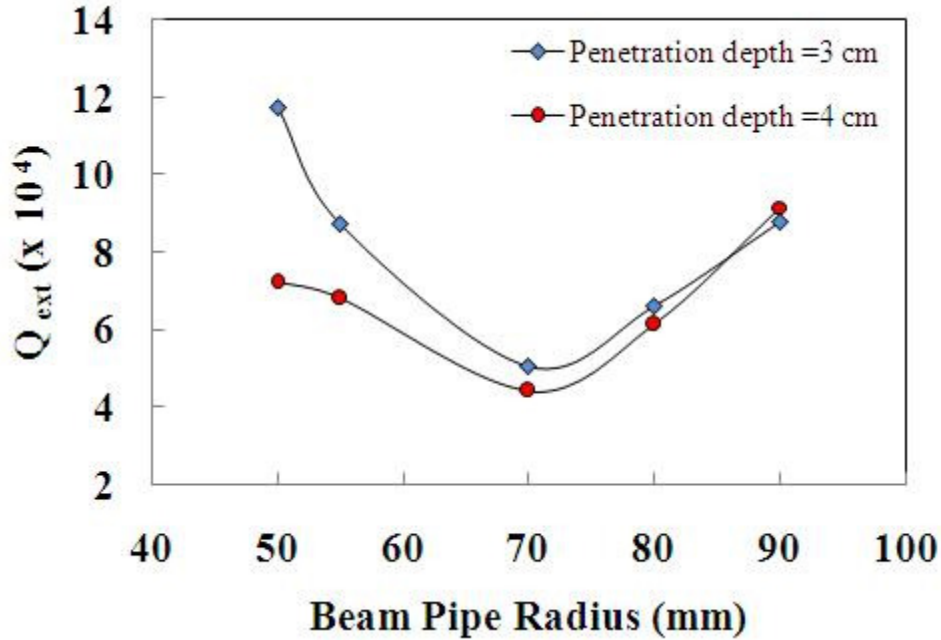


Figure 19: Effect of Beam Pipe Radius, ($f = 1.05$ GHz)

Table 8: Optimized Coupler Dimensions of 700 MHz and 1.05 GHz Cavity

Frequency	Required Q_{ext}	Coupler Dimensions (mm)	Beam Pipe Radius (mm)	Coupler Position w.r.t. cavity Centre(mm)	Penetration Depth (mm)
700 MHz	1.56×10^6 [14]	ID: 43.48, OD : 100	50	130	2
1.05 GHz	1.48×10^6 [16]	ID: 43.48, OD : 100	50	120	-15

To get better insight of the subject a copper prototype of the cavity with coaxial input coupler is fabricated at MDPDS Workshop, BARC, Mumbai. The experimental results will be discussed in Chapter 4.

3.4] Design of Door-knob Transition

Transition between rectangular waveguide and co-axial line can be designed in numerous ways. Of which door-knob transition is widely used as it provides broadband matching and is more reliable at high power [72,73]. In this type of transition, center conductor of co-axial line terminates on the opposite side of the guide in a knob of proper size to permit impedance matching and of streamlined shape to increase the power handling capacity as shown in figure 20. The performance of this type of transition is limited to the power level that causes arcing in the co-axial cable. Here it was used to provide matching between waveguide (WR1150: 29.21cm x 14.605cm) and co-axial antenna. The position (from shorted end) and the size of the door-knob was optimized to achieve return loss~ -32.55 dB and transmission loss ~0 dB at a frequency of 700 MHz which indicates matched transition (see figure 21). Similarly a door-knob having base radius 28 mm and placed at a distance of 74.5 mm from shorted end provides matching at 1.05 GHz between the same coaxial coupler and waveguide WR770.

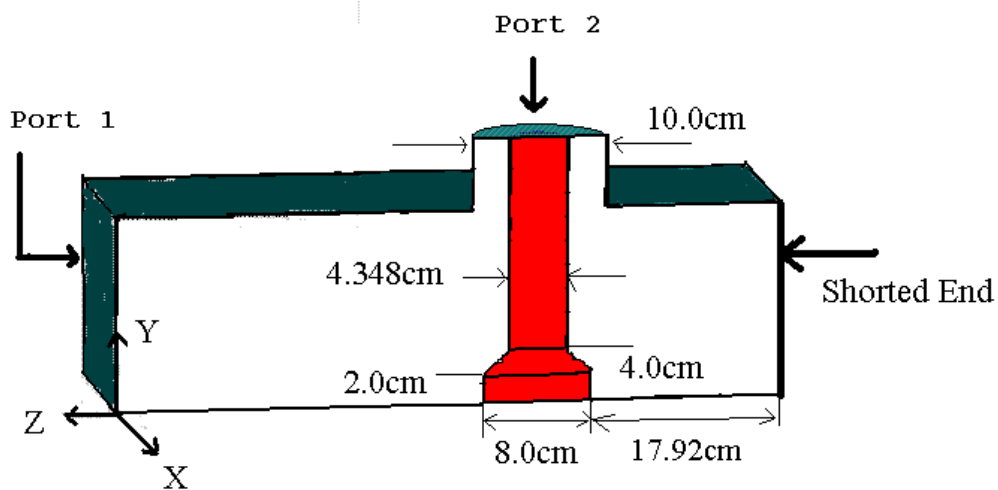


Figure 20: Details of Door-knob transition, ($f = 700$ MHz)

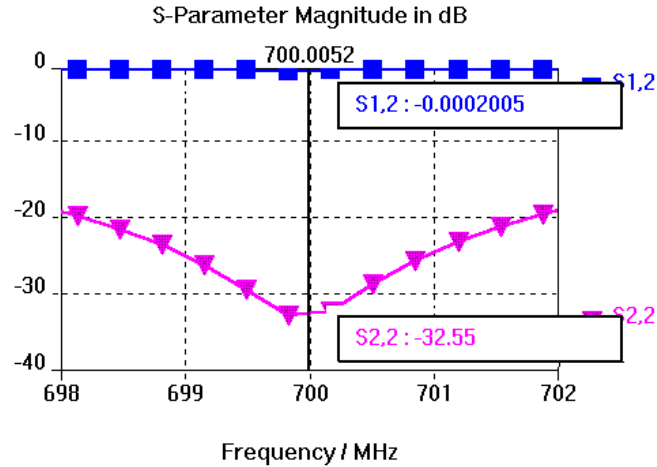


Figure 21: S-parameter response at Door-knob Transition simulated using MWS

3.5] Optimization of Endcell and Coupler for 5-Cell cavity

In previous sections, the effect of various parameters on the coupling factor for a single cavity was studied which is essential for the basic understanding of the subject. In practice, the accelerator cavity is made up of multiple cells. To understand the issues involved in the coupler design of a multicell cavity, we have studied 5-cell cavity. In this section an end cell design and the coupler design of 5-cell, 700 MHz cavity is presented.

A 5-cell, 700 MHz assembly with coaxial coupler (dimensions as given in table 8) was simulated with the MWS. A Q_{ext} of the coupler was calculated at π - mode without modifying the end cell. A $Q_{\text{ext}} \sim 2 \times 10^7$ was obtained for the optimized coupler settings, even the full penetration of the antenna inside the beam pipe could not provide required coupling. Thus the optimization of the end cell and beam pipe was carried out.

3.5.1] Optimization of End Cell

The design of the end cell depends on the internal cell design. The design criteria is same the internal cell design. It should try to attain minimum $E_{\text{pk}}/E_{\text{acc}}$ and $H_{\text{pk}}/E_{\text{acc}}$ field, in addition it

should incorporate power coupler [73]. A left half of end cell is kept same as the internal cell while the right half is optimized so as to accommodate power coupler, higher order mode (HOM) coupler and the beam pipe of larger diameter. Two different types of designs are employed for the end cell design. In a first (type a) the half cell with larger bore radius and matching beam pipe is used while the other design (type b) uses a half cell with elliptical iris and a broader beam pipe [74] as shown in figure 22. The optimization of end cell is also important for the HOM damping [75]. Since this topic is beyond the scope of the thesis, only the optimization of end cell for getting optimum coupling is considered.

The wall angle and the beam pipe radius were optimized so as to reduce the peak fields on the surface. To match the resonant frequency of end cell with the inner cells, length of the end cell is also optimized. Due to simplicity of mechanical design, “type a” shape was chosen for the end cell. Several runs of the code by varying different parameters were required to reach at the final configuration. A comparison of optimized parameters of the end cell with inner cell is shown in table 9; the peak fields in end cell are nearly same as the inner cell. The MWS output of 5-cell with modified end cell and resonating at π - mode is shown in figure 23. The variation of external Q with penetration of antenna is shown in figure 24. The required coupling is obtained at a penetration depth of 1 mm⁴; the penetration depth is calculated w.r.t. the bore radius of inner cell.

⁴ The dimensions of the coupler are same as that described in table 8.

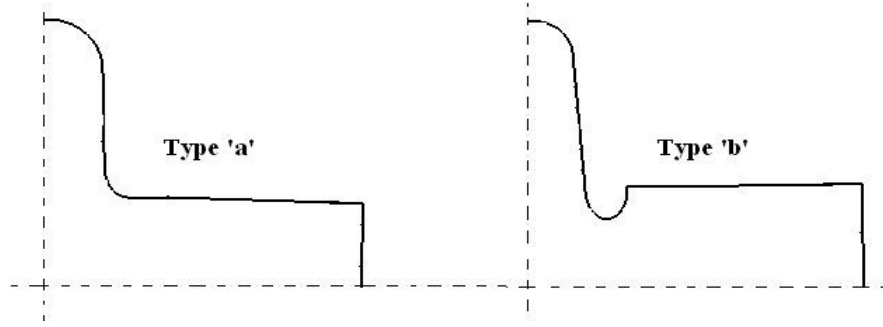


Figure 22: Different types of End cells

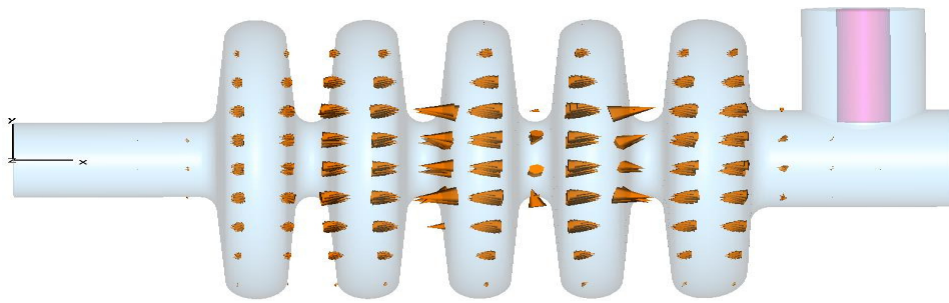


Figure 23: 5-cell assembly with optimized end cell and coaxial coupler simulated using MWS;
arrows indicate the direction of electric field (π mode)

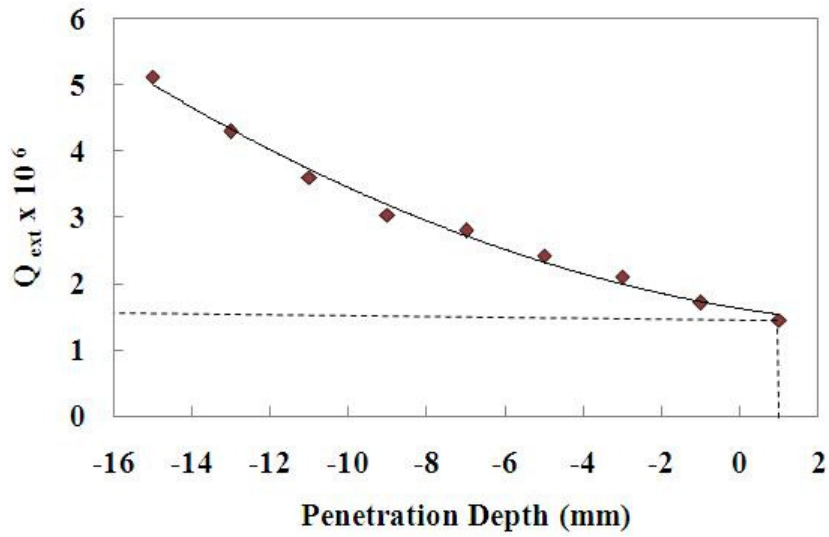


Figure 24: Change of Q_{ext} with penetration depth of inner conductor

Table 9: Optimied dimensions of inner cell and end cell for 700 MHz, 5-cell cavity

RF Parameters	Inner Cell	End Cell
Diameter	37.38 cm	37.38 cm
Length (half cell)	4.5 cm	5.36 cm
Dome Radius	2.5 cm	3.5 cm
Dome ellipse ratio	1.0	1.0
Wall Angle	4.0 ⁰	2.5 ⁰
Iris ellipse ratio	0.65	0.7
Bore radius	5.0 cm	6.5 cm
E_{pk}/E_{acc}	3.26	3.43
H_{pk}/E_{acc}	6.57 mT/(MV/m)	6.75 mT/(MV/m)

3.6] Conclusion

In conclusion, the studies shows that Kroll-Yu method that was thought to be useful for evaluation of low Q_{ext} (< 20) can be used successfully for the evaluation of high Q_{ext} provided the data points are chosen near the point where cavity frequency is close to the coupler frequency. The three runs of the MWS are sufficient to estimate the Q_{ext} .

The comparison between three techniques shows that P.Balleyguier method is very simple, straightforward and can be used efficiently for low as well as high external Q . Only two runs of the MWS are sufficient to evaluate Q_{ext} . The MWS module is useful to get the quick idea of the results. Our experience shows that the results are reliable as long as there is no change in the resonant frequency. The Kroll-Yu method is based on the fitting of data points, thus choice of

data points can affect the results. Also initially more number of computer simulations are required to identify the exact coupler length where cavity frequency and coupler frequency are matching. Figure 13 shows the comparison between three methods, the discrepancy in the results is observed at very high Q_{ext} ($>10^7$).

The larger penetration of antenna in the beam pipe can give better coupling but at the same time it may distort the field inside the pipe. A larger beam pipe gives better coupling at a given penetration depth. The coupler parameters for the single cavities are optimized using these criteria. The results are listed in table 8. In multicell (5-cell) cavity due to additional power loss, the required Q_{ext} cannot be achieved for the coupler parameters same as the single cell. It is essential to modify the end cell. The optimized parameters of end cell having larger bore radius are given in table 9.

CHAPTER 4

EXPERIMENTAL RESULTS

4.1] Introduction

In order to verify the validity of simulation results copper models of the cavity and coupler were fabricated. The cold model testing was carried out using Rhode & Schwartz Vector Network Analysis. R/Q of the cavity and the external Q of the coupler are the geometrical factors and hence are independent of the material used. In the cold model testing, cavity frequency, f_0 , Q_0 , R/Q was measured. Also external Q of the coupler was measured for different penetration depths.

4.2] Measurement procedure

4.2.1] Measurement of f_0 and Q_0

A RF power is fed to the cavity using pick up probes. A measurement can be done in either transmission mode (two pick up probes) or reflection mode (single probe). A resonant frequency will appear as a “peak” in the transmission mode (S_{21} or S_{12}) and as a “deep” in reflected mode (S_{11} or S_{22}). A frequency corresponding to the tip of the peak/ deep is the resonant frequency, ' f_0 '. A bandwidth of the resonance curve at 3-dB points is ' Δf '. The loaded quality factor, Q_L is given by equation 58. Using equation 34, the unloaded quality factor, Q_0 can be determined.

$$Q_L = \frac{f_0}{\Delta f} \quad (58)$$

4.2.2] Measurement of R/Q

Any object placed inside the cavity volume will disturb the field inside the cavity that will change the resonant frequency of the cavity. Experimentally R/Q can be evaluated by measuring the frequency shift due to perturbing object. By definition R/Q is given by [76],

$$R/Q = \left(\int E ds \right)^2 / 2 \omega U \quad (59)$$

From Slater's Perturbation Theorem,

$$df/f_0 = k \int (\mu H^2 - \epsilon E^2) dv / 4U \quad (60)$$

If magnetic field is zero, $H=0$,

$$df/f_0 = -\epsilon k \int E^2 dv / 4U = -\epsilon k E^2 \Delta v / 4U \quad (61)$$

$$E = \sqrt{\frac{4U df}{\epsilon k \Delta v f_0}} \quad (62)$$

Substituting equation (62) and $\omega = 2\pi f_0$ in equation (59),

$$R/Q = \left(\int \sqrt{df} ds \right)^2 / \pi \epsilon k \Delta v f_0^2 \quad (63)$$

Where, ds is a bead displacement, Δv is volume of the bead, $k = 1$ (assumed as bead is much smaller than the cavity dimensions), df is frequency shift due to bead, $\epsilon = \epsilon_0 (\epsilon_r - 1 / \epsilon_r + 2)$, ϵ_0 is the permittivity of free space, ϵ_r is the dielectric constant (=2.1 for teflon and tends to infinity for metallic bead)

4.2.3] Measurement of Q_{ext} of the power coupler

When working in transmission mode two couplers are used of which one is the main power coupler while another is a pick up/ auxiliary antenna. The coupling factor, β of auxiliary antenna is fixed. At a given penetration depth of the main coupler, Q_L of the cavity, coupling coefficient, β of the auxiliary coupler and the transmission coefficient, S_{21} is measured with Vector Network Analyzer. The relation between Q_{ext} and all these parameters is given by [77],

$$Q_{ext} = \frac{4\beta Q_L}{(1 + \beta)} 10^{|S_{21}(dB)|/10} \quad (64)$$

In reflected mode, a reflected power is measured at the coupler port. The reflected signal S_{22p} and S_{22b} corresponding to the position at resonant frequency and far away from the resonant frequency is measured in dB. The reflection coefficient, ρ is determined using equation 65. The corresponding VSWR, ' Γ ' is calculated from equation 66. The phase of the signal determines the type of coupling viz., “under coupling” or “over coupling” [76,78]. A ' β ' is calculated from ' Γ ' as given by equation 67. Finally, using equation 33, Q_{ext} is deduced. In case of very high Q_{ext} , the signal is very weak and determination of external Q is difficult. In such case, transmission mode measurement is preferable.

$$\rho = 10^{-|S_{22p} - S_{22b}|/20} \quad (65)$$

$$\Gamma = \left| \frac{1 + \rho}{1 - \rho} \right| \quad (66)$$

$$\begin{aligned} \beta &= \Gamma; \text{overcoupling} \\ \beta &= 1/\Gamma; \text{undercoupling} \end{aligned} \quad (67)$$

4.3] Experimental set-up

Figure 25 shows the measurement set up, a 1.05 GHz cavity with beam pipe and coaxial coupler. A bead pull set up required for the measurement of field distribution in the cavity is also shown. A bead woven in nylon thread is inserted in the cavity through the beam port, the frequency and phase change along the length of the cavity is measured by moving the bead with the help of pulleys. The different parts of the assembly like cavity, beam pipe and coaxial coupler are shown in figure 26. A similar set up is used for the measurement of different cavities.

4.3.1] Results of 1.05 GHz cavity

A prototype single cell copper cavity with the co-axial coupler was fabricated. The RF power was fed to the cavity with the help of co-axial type of power coupler (ID: 34.8 mm; OD: 80 mm) that was situated at a distance of 120 mm from the cavity center on the beam pipe having diameter of 80 mm and length of 150 mm.



Figure 25: Cavity with Coaxial Coupler and the bead pull set up



Figure 26: Cavity, Beam pipe and Coupler Parts

Figure 27 shows the schematic of cavity with co-axial power coupler. The inner conductor of the power coupler was made hollow to reduce the weight and was soldered to the central pin of the N-type connector. The aim of the experiment was to check whether the designed parameters are achieved. The measurements were carried out with Rhode & Schwarz Vector Network Analyzer (VNA). Port 1 of VNA was connected to a small pick up probe that was used to excite the cavity axially. Input coupler was connected to the Port 2 of the VNA as shown in the figure 27.

The RF parameters of the simulated half cell using ELLFISH are listed in table 2. Here, it is essential to note that ELLFISH does not directly calculate the R/Q , it either calculates the shunt impedance per unit length or (r/Q) that is effective shunt impedance divided by Q_0 . Thus calculated R/Q of the monopole or TM_{010} mode is given by,

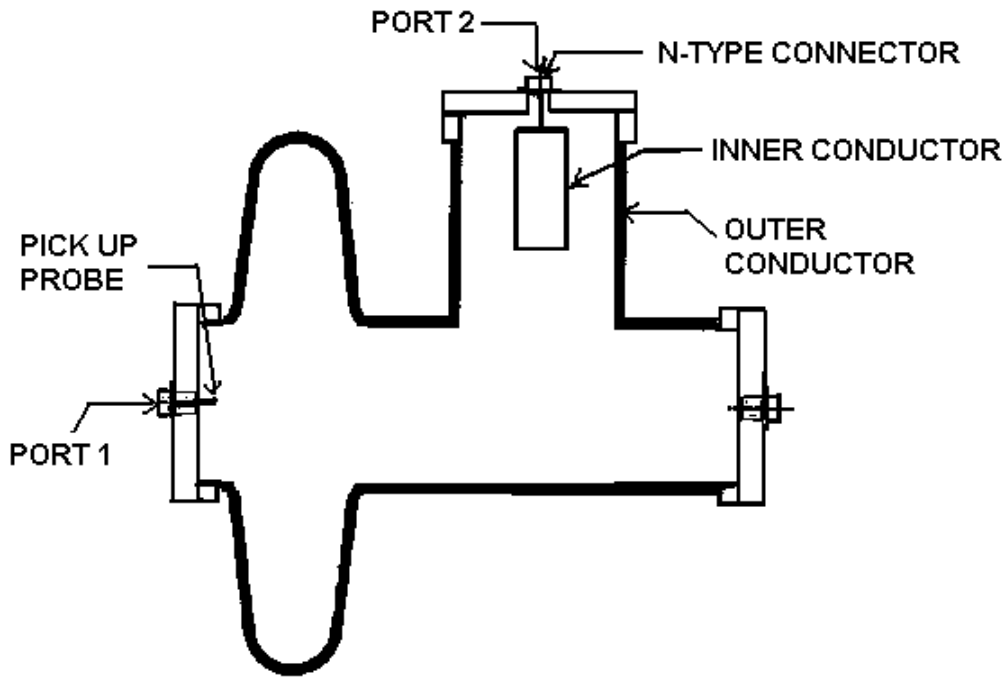


Figure 27: Schematic of cavity and power coupler

$$R/Q = (r/Q)/2T^2 = 6.94 ; T = 0.78 \quad (68)$$

The factor $\frac{1}{2}$ converts the peak voltage values to RMS voltage.

The RF surface resistance at a frequency of 1.05 GHz for a copper material is $8.42 \times 10^{-3} \Omega$. Thus from geometric factor, G the Q_0 of the copper cavity at room temperature is 16793.

4.3.2] Discussion

A] Measurement of resonant frequency and Q_0 : To measure the resonant frequency and Q_0 of the cavity, the length of the inner conductor of input coupler was kept 75 mm i.e. penetration depth of -13 mm, the coupling coefficient due to the coupler was negligible. The coupling coefficient of the pick-up probe was 0.069. The measured resonant frequency was 1.051 GHz. The frequency bandwidth at 3-dB points was 75 kHz. The measurement results are shown in figure

28. Thus Q_L and Q_0 were 14016 and 14982 respectively. The degenerate dipole mode was observed at frequencies of $f_1=1.4693$ GHz and $f_2=1.4706$ GHz (See figure 29).

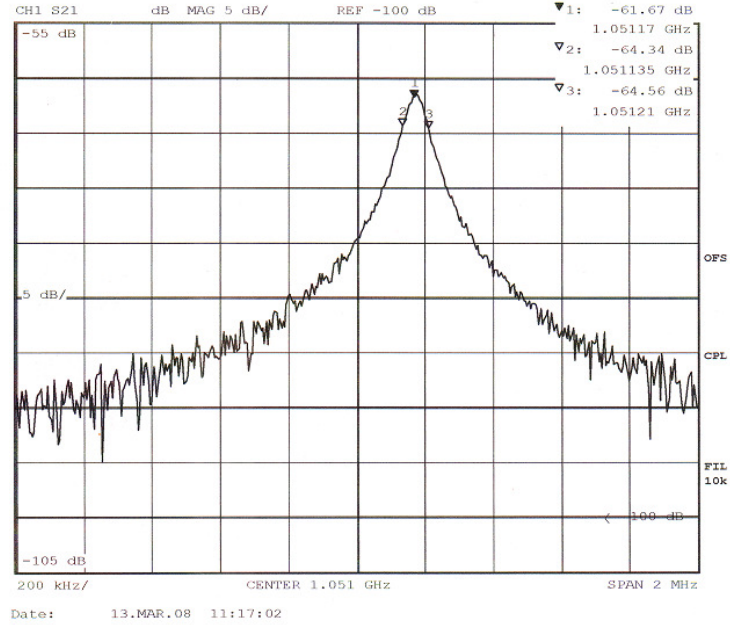


Figure 28: Resonant frequency and Q_1 ; VNA output

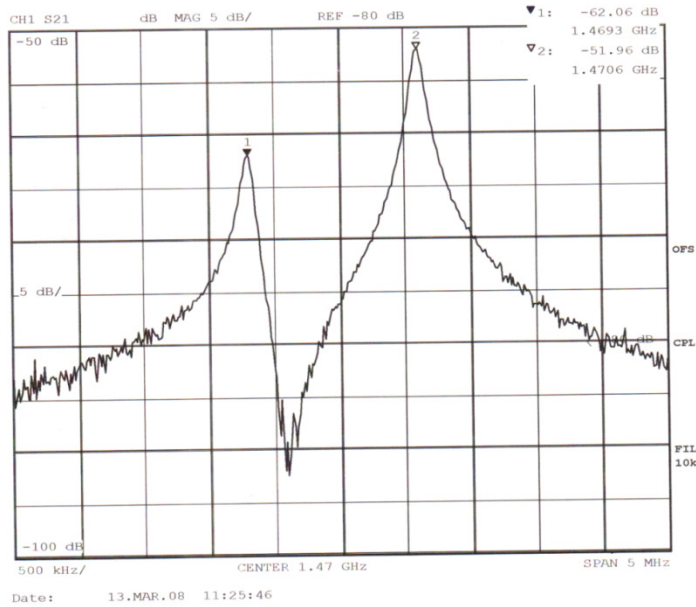


Figure 29: Dipole frequencies; VNA output

B] Measurement of geometrical Shunt Impedance, R/Q: A copper bead of radius ~2 mm and length ~4mm is made to pass through the central axis of the cavity, a change in resonant frequency is noted at the various positions of the bead with a step (=ds) of 10 mm. Figure 30 shows the variation of resonant frequency with position of the bead. A maximum frequency shift of ~77.5 kHz was observed in the center of the cavity. Figure 31 and 32 show the frequency shift in the center of the cavity and phase shift along the cavity length induced because of the bead. Since the measurement is carried out at discrete positions with a uniform interval ds , the integral can be converted to summation, thus equation 63 is modified to equation 69. The calculated R/Q, using equation 69, was 9.4Ω .

$$R/Q = \left(ds^2 \sum_{i=1}^n \Delta f_i \right) / \pi \epsilon k \Delta v f_0^2 \quad (69)$$

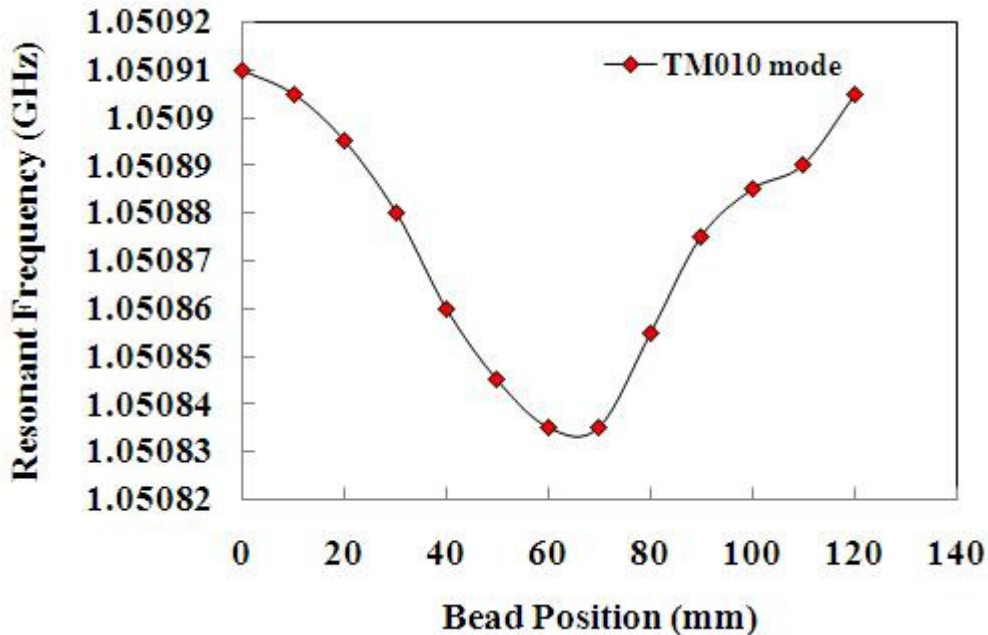


Figure 30: Variation of resonant frequency with bead position

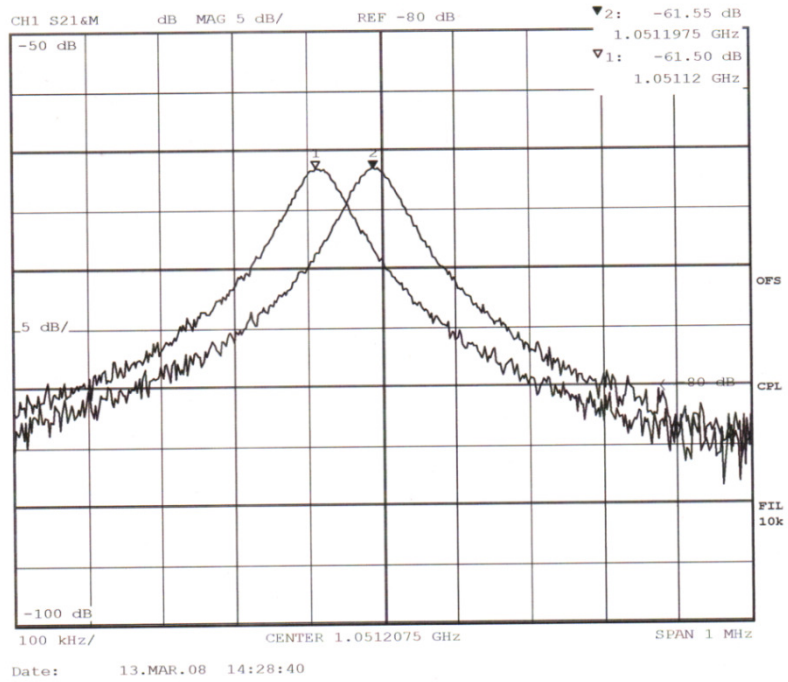


Figure 31: Frequency shift of TM_{010} mode; VNA output

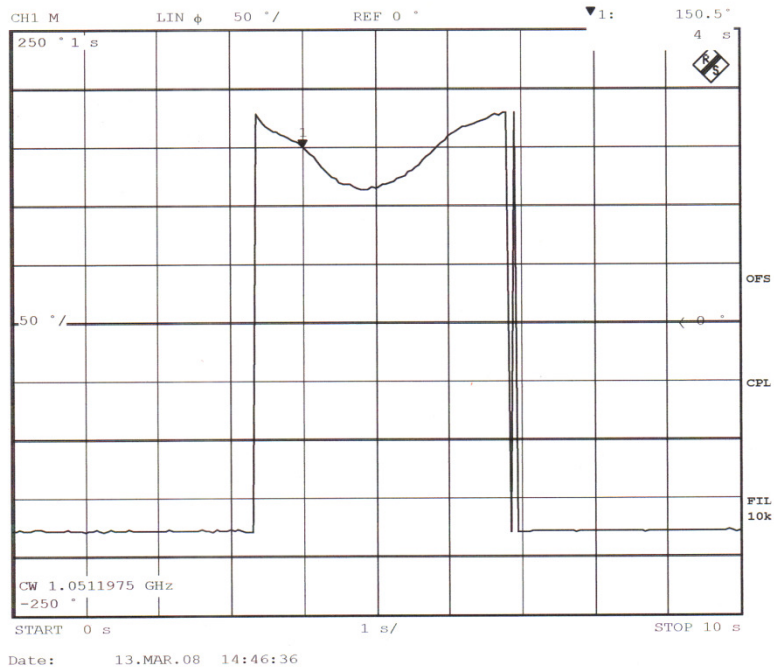


Figure 32: Phase shift of TM_{010} mode; VNA output

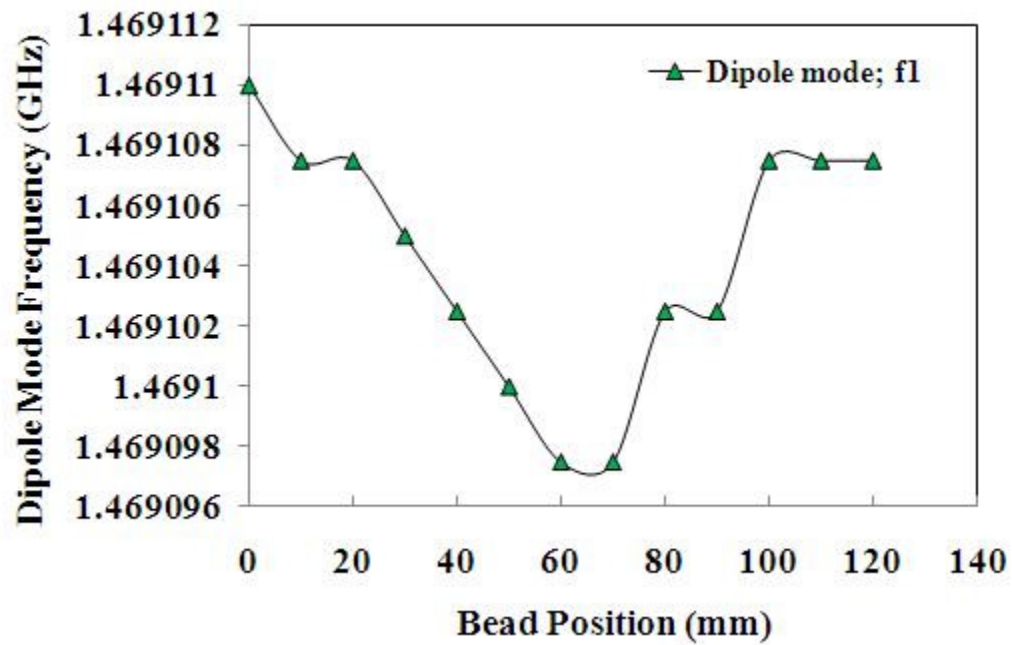


Figure 33: Variation of dipole mode frequency, f_1 with bead position

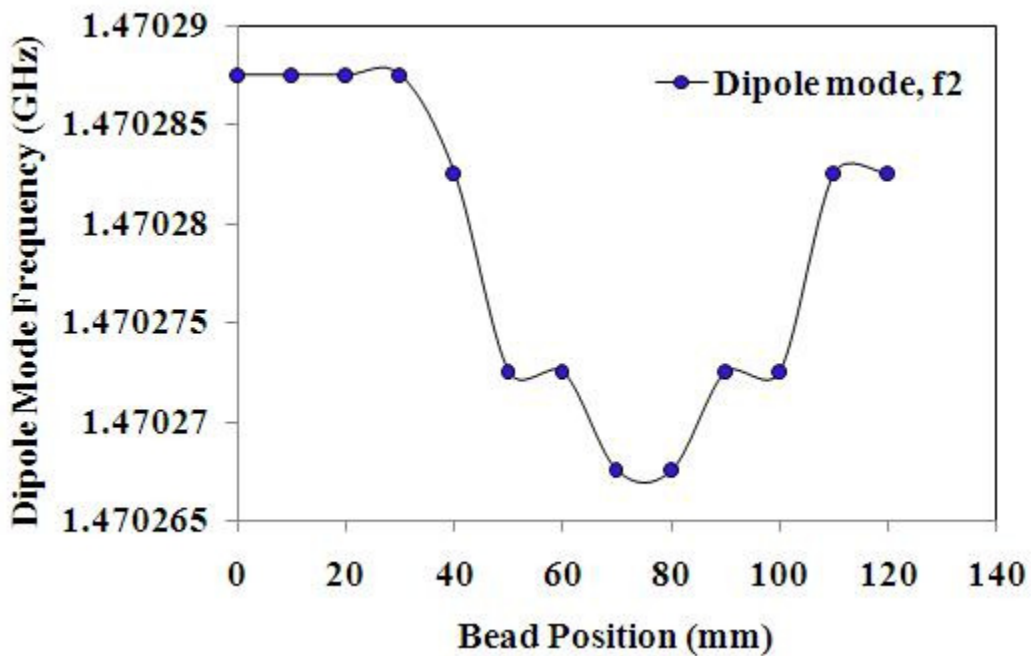


Figure 34: Variation of dipole mode frequency, f_2 with bead position

In case of dipole (TM₁₁₀) mode, electric field is zero on the central axis of the cavity. Thus a bead is passed off-center (2.9 cm away from the central axis). A teflon bead of radius ~ 2mm and length ~ 4 mm is used so that frequency shift due to magnetic field is zero and the equation 69 is applicable. The figure 33 and 34 shows the variation of dipole mode frequencies with the position of teflon bead. The calculated R/Q's at the dipole mode frequencies f₁ and f₂ were 3.34 Ω and 4.32 Ω respectively.

CI Measurement of external Q, Q_{ext} of the Input Coupler: As shown in figure 27, the cavity was simulated through auxiliary antenna connected at port 1. The coupling factor, β of auxiliary antenna is fixed. The main coupler is connected at port 2. The Q_{ext} was measured in transmission mode and was evaluated using equation 64 at different penetration depths of coaxial antenna.

By changing the penetration depth of the inner conductor of the co-axial coupler from -40 mm to 40 mm, the Q_{ext} is changed from 6.14 x 10⁸ to 9.6 x 10⁵ as shown in figure 35. Similar measurements were carried out for the axial coupler where beam pipe acts as an outer conductor of the co-axial coupler. By varying the penetration depth of inner conductor from -108 mm to -63 mm, the Q_{ext} is varied from 2.25 x 10⁷ to 5 x 10⁴.

Figure 35 also shows the comparison of the experimental data with the computed Q_{ext} values. It is found that for Q_{ext} > 10⁷ there is a discrepancy in the measured and computed values. As the coupling becomes weaker (high external Q), the measured signal is very poor (the maximum power out put of R&S VNA is limited to 0 dBm), thus measurement error is larger at higher Q_{ext}.

The experimental data can be fitted well with the empirical relation of the form,

$$Q_{ext} = a + b \text{Exp}\left(-\frac{s}{c}\right) \quad (70)$$

Where a, b, c are the fitting constants and 's' is the penetration depth.

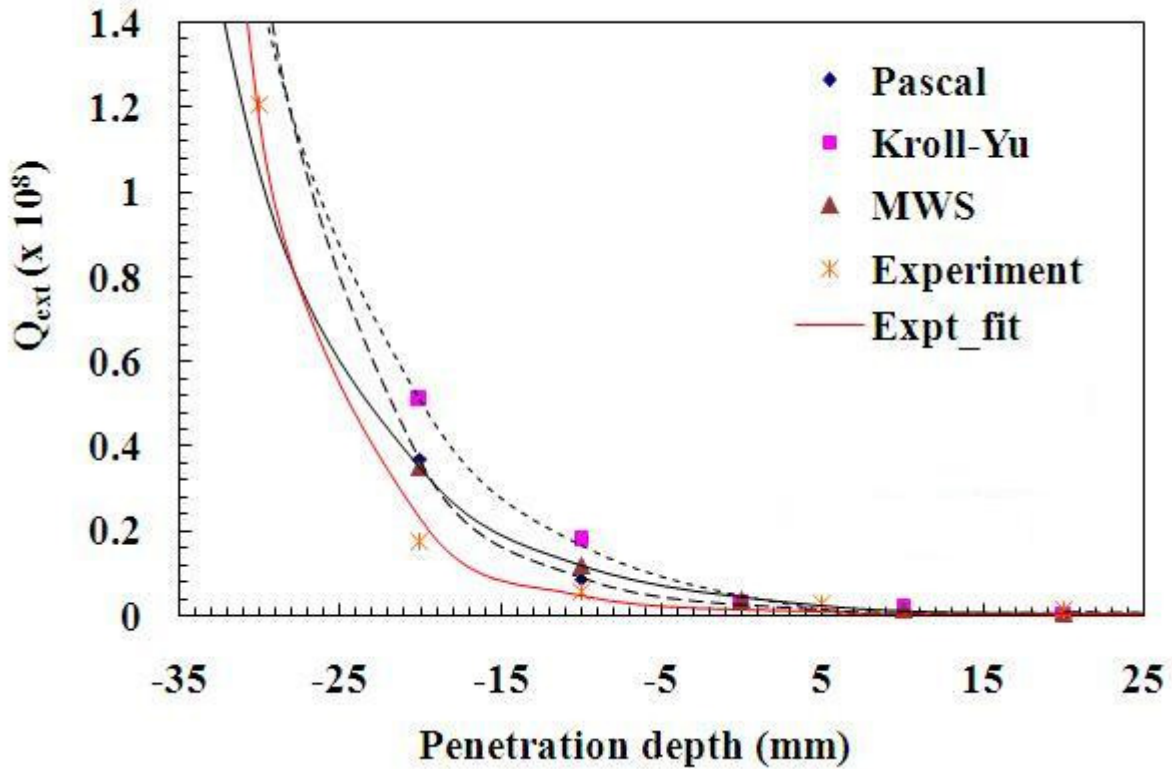


Figure 35: Variation of Q_{ext} with Penetration depth; experimental and computed data; $f=1.05$ GHz

In figure 35, the markers (orange colour) indicate measured values of Q_{ext} while fitted data using equation 70 is shown by solid line (orange colour). The fitting parameters a , b , c are 575341, 8482523, 6.1 respectively.

4.4] Results of 700 MHz Cavity

The 700 MHz cavity was fabricated at MDPDS workshop from single copper piece with machining. The measured resonant frequency and Q_0 were 695 MHz and 10880 respectively. The figure 36 and 37 show the measured resonant frequency and the field inside the cavity. The dipole mode was observed at ~ 1 GHz. The measured and computed external Q of the coupler at different penetration depths is shown in figure 38. Experimental results are in good agreement

with the computed values. As described in previous section, the experimental values can be fitted well with equation 70 with fitting parameters a, b, c as -656.07, 177.21, 8.61 respectively.

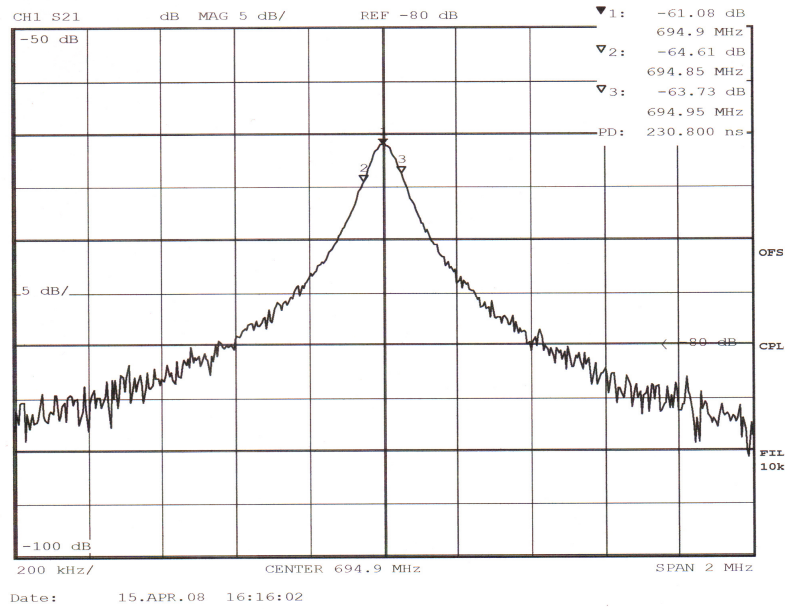


Figure 36: Frequency response of 700 MHz cavity

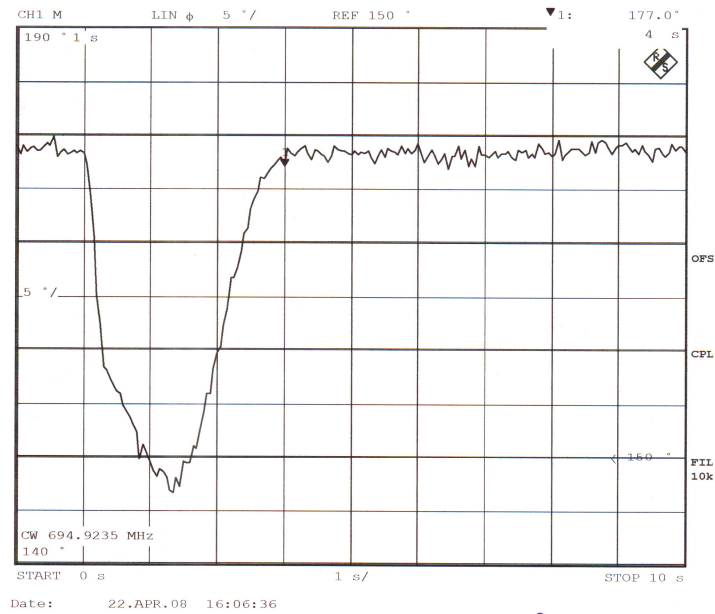


Figure 37: Phase shift due to bead; field inside the cavity

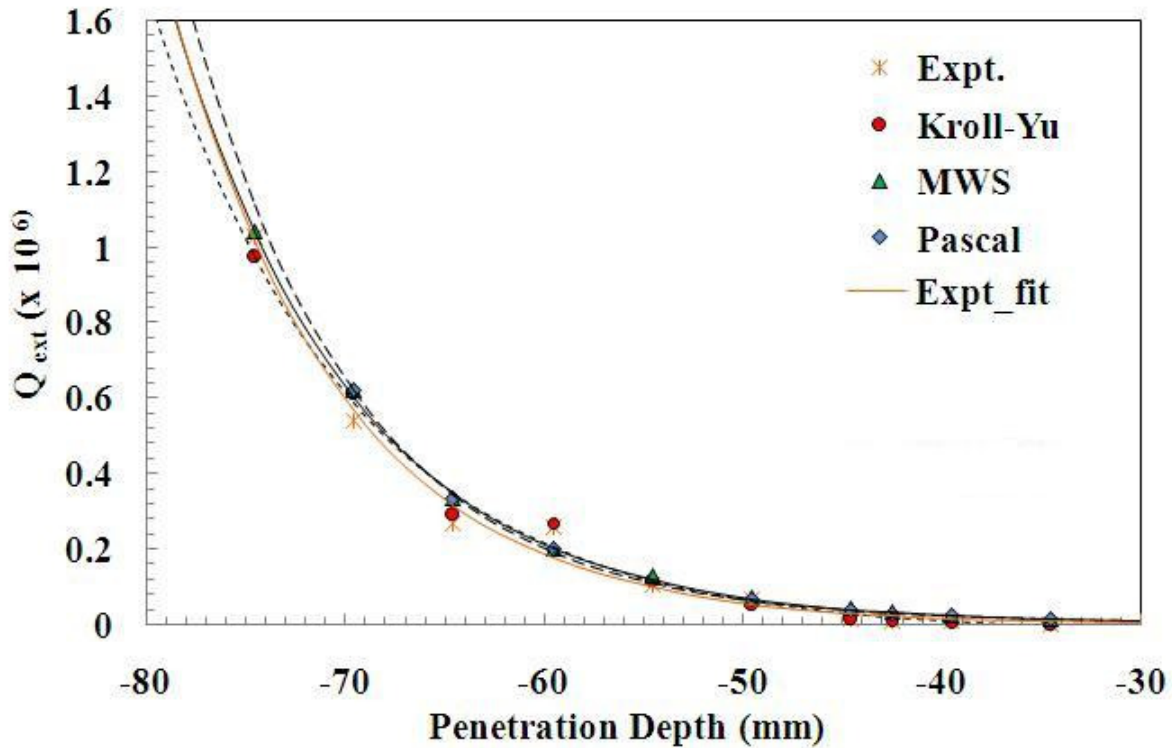


Figure 38: Comparison of measured and computed External Q of 700 MHz cavity

4.5] Results of Formed Cavity

Since Niobium is a costly material machining is not a suitable technique of cavity fabrication. In general, half-cells are fabricated from niobium sheet by forming later two cells are electron beam welded at equatorial position to form a cavity [79]. Several other techniques like hydro forming and spinning are also being tried so as to avoid the electron beam welding (EBW) joint. To begin with we have decided to use the more proven technique of forming the cavities. To develop the process of forming, initially cavities were made of ETP copper, later the process will be adapted for niobium cavity fabrication. Figure 39 shows the cavities fabricated using forming technique. The measured frequency response and field distribution inside the cavity are shown in figure 40 and figure 41 respectively.



Figure 39: Formed Copper cavities ($f = 1.05$ GHz); photographs showing half cells and full cells

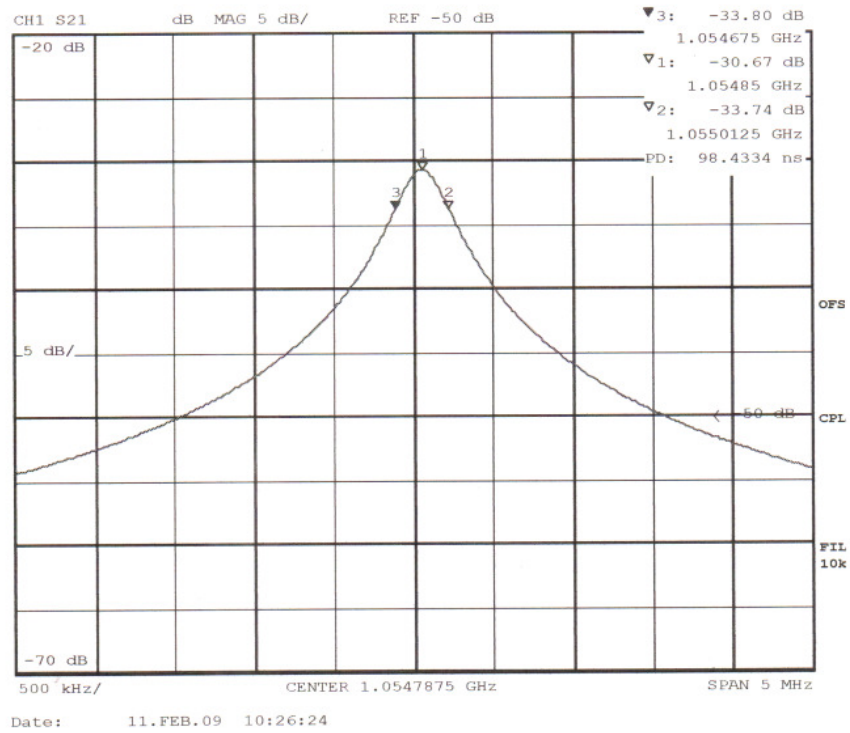


Figure 40: Frequency response of the formed cavity

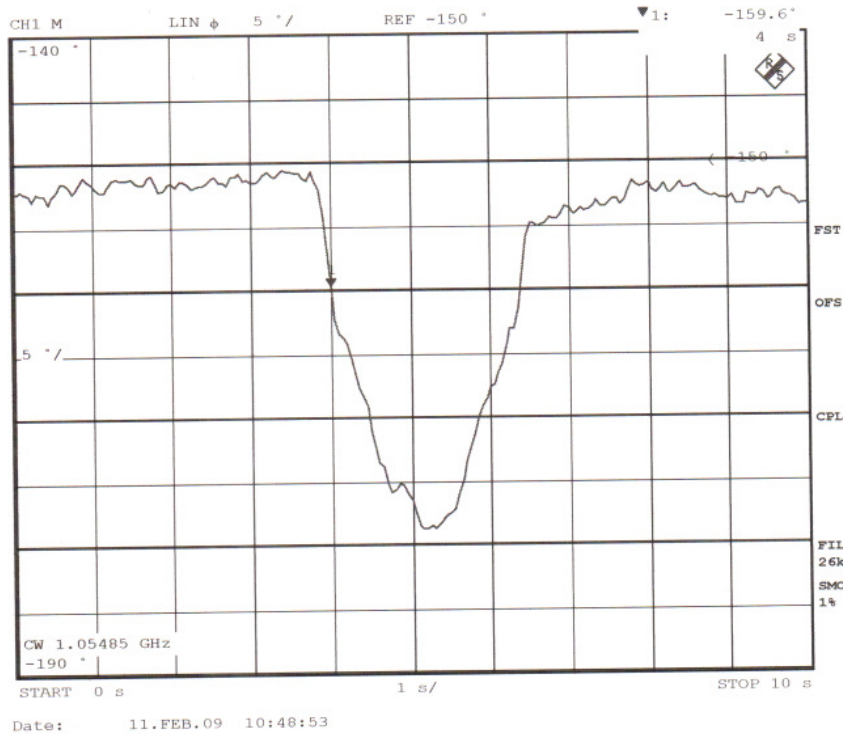


Figure 41: Field inside the cavity

4.6] Conclusion

R/Q and the Q_{ext} are the geometrical parameters of the cavity and the coupler and will remain unchanged for the given geometry. The measured value of the R/Q is required to calculate the accelerating field developed in the cavity at a given input RF power to study the Q-E behavior of the cavity at LHe temperature.

In case of dipole mode, loss factor is directly proportional to R/Q. Thus it gives information about the power lost at LHe temperature.

The Q_{ext} of the input coupler depends on the penetration depth of the inner conductor. At room temperature inner conductor length can be adjusted so that $Q_{\text{ext}} \cong Q_0$ at LHe temperature. This coupler setting will give critical coupling at LHe temperature.

CHAPTER 5

MULTIPACTING ANALYSIS OF COAXIAL COUPLER

5.1] Introduction

The performance of superconducting cavity, couplers and ceramic windows is greatly affected due to multipacting. Beyond a certain threshold, cavity fields cannot be increased with increase in input power as incident power is absorbed by multipacting electrons. Evidence of multipacting has been observed experimentally in many RF devices. Thus it is essential to study the multipacting phenomena at various power levels and RF frequencies.

The word “multipacting” is a contraction of the phrase multiple impacts. In a RF device, an electron originating from the wall, by bombardment of charged particles/x-rays or produced by the ionization of the residual gas, gets energized by the electromagnetic fields present in the device. When such an electron strikes the wall, depending upon the incident energy of incident electron, more number of electrons are knocked out if the “secondary emission coefficient (SEC), δ ” of the surface is greater than 1. In turn the secondary electrons are accelerated and upon impact produce another generation of electrons. The process repeats and a large number of electrons are generated. If the resonance condition is established, an electron current increases exponentially. It is limited only by the space charge effect and the RF power.

In practice, two types of multipacting phenomena are observed, viz., one-point multipacting and two-point multipacting. Usually, one point multipacting is observed in RF cavities where only one RF surface is involved. The two point multipacting is observed in the input couplers, co-axial lines, low beta cavities where two RF surfaces are closely spaced. The study of multipacting is an involved process because of the complex geometries of the RF

devices, time varying nature of the electromagnetic fields and susceptibility of the phenomena to the surface conditions. Thus the analysis is done using numerical methods.

The increasing demand of superconducting cavities for various applications and the need of transferring higher power levels with couplers have triggered the interest in understanding the phenomena and development of various 2-d and 3-d codes by various groups. Among these the MultiPac code by University of Helsinki [80], MUPAC from Saclay [81], TWTRAJ from Genoa [82,83], MULTIP [84] and Xing [85] from Cornell, TRAK-3D from Albuquerque [86] and MULTP from Moscow[87] are some of the existing tools.

In general, all these codes perform the task in three steps. The first step is to define the problem geometry and the calculation of RF fields in the geometry. Some of the codes have built-in e.m. field solver while most of the codes use MAFIA, SUPERFISH etc. to get e.m. fields in the geometry. The second step is to impose surface properties on the RF surface and particle tracking. A large number of particles with different initial conditions are introduced in the structure. The third step is to identify the resonant trajectories. Most of the codes use the concept of counter functions (CF, ECF, DF) developed by MultiPac code group to identify the resonant trajectories [88].

There are number of approaches to deal with the multipacting problem but simplest way is to take care of it in the design stage i.e. to optimize the geometries in such a way that multipacting barriers are avoided at operating power levels. Thus it is essential to have a simulation tool. Since no codes are available to us, it was decided to develop the in house code.

The present chapter describes in detail the development of code and the multipacting analysis of the coaxial coupler. In the present code, analytical solution of the e.m.field is used.

The particle trajectories are tracked by solving equations of motion numerically. The resonant trajectories are identified by calculating the enhanced counter function. A emission model for secondary electrons is assumed and the energy and emission angle of secondary electrons is assigned using Monte Carlo Method.

5.2] Theory

The study of multipacting essentially involves the tracing of electron trajectories in a electromagnetic field and calculation of generated secondary electrons upon the impact of primary electrons with the physical boundary of the RF structure.

Consider the co-axial coupler with propagating TEM mode, having inner conductor radius ‘a’ and outer conductor radius ‘b’. The basic parameters of which are previously discussed in Chapter 3. Considering the time varying nature of e. m. field, at any instant of time ‘t’, the electric and magnetic field is given by,

$$E(\vec{r}, t) = E_0 \sin(\omega t - kz) \quad (71)$$

$$H(\vec{r}, t) = H_0 \cos(\omega t - kz) \quad (72)$$

These are the fields in a coupler that is infinitely long i.e. when a traveling wave exists in a coupler or in short, when there is no reflected wave. In practice coaxial coupler is used to feed power to the load e.g. cavity. Thus it has finite length and due to the mismatch between the load impedance and Z_0 , a reflected wave exists. Thus electric and magnetic field inside a coupler at any position, (r,z) and time, t is a vector sum of incident and reflected wave. The standing waves are generated and electric/magnetic nodes and antinodes are generated along the length of the coupler. In general E(r,t) and H(r,t) can be written in terms of VSWR, Γ as,

$$E(\vec{r}, t) = E_0 \sin(\omega t - kz) \left(\frac{2\Gamma}{1+\Gamma} \right) \quad (73)$$

$$H(\vec{r}, t) = H_0 \cos(\omega t - kz) \left(\frac{2\Gamma}{1+\Gamma} \right) \quad (74)$$

Here, it is assumed that the length of the co-axial coupler is $\lambda/2$ and the electric field is zero at the ends. The general equation of motion of electron is given by,

$$\ddot{\vec{r}} = \left(\frac{e}{m} \right) (\vec{E} + \vec{v} \times \vec{B}) \quad (75)$$

Since the structure is azimuthally symmetric, the problem is solved in r-z plane (2-dimensional geometry). Upon resolving equation (75), the radial and axial components are respectively,

$$\ddot{r} = \left(\frac{e}{m} \right) (E_r - B_\phi v_z) \quad (76)$$

$$\ddot{z} = - \left(\frac{e}{m} \right) (B_\phi v_r) \quad (77)$$

Equations (76) and (77) are the coupled equations of motion and are solved numerically using ‘‘Euler’s method’’ for small time steps, Δt . The initial conditions like the position, energy and the phase of the electron at time $t=0$ are provided by the user. The new velocity and the position of the electron after time ‘ Δt ’ is calculated. The calculations are continued till the electron hits the physical boundary of the RF device (i.e. $r=a$ or $r=b$ in this case). When it hits the wall the final energy, position and time is recorded.

The secondary emission coefficient, δ is different for different materials but the general description of δ with impact kinetic energy is as shown in figure 42. A ' δ ' is greater than 1 only in the energy interval between E_1 and E_2 and is maximum at particular energy, E_m . For niobium, in the energy range of $E_1 \sim 50$ eV to $E_2 \sim 1500$ eV, δ is greater than 1 and is maximum ($\delta_m \sim 1.2$) at $E_m \sim 389$ eV [25].

A program calculates ' δ ' when the electron hits the physical boundary and the energy of electron lies between the interval (E_1, E_2) which is provided by the user. The ' δ ' at any energy ' E ' is calculated using model given by J.R.M.Vaughan [89] as follows,

$$\delta = \delta_m [f \text{Exp}(1-f)]^a ; f = E/E_m \quad (78)$$

Where, $E_1 \leq E \leq E_2$, ' E ' is the emitted electron energy and ' E_m ' is the energy at which $\delta \sim \delta_m$. The parameter ' a ' has value 0.62 for $f < 1$ and 0.25 for $f \geq 1$.

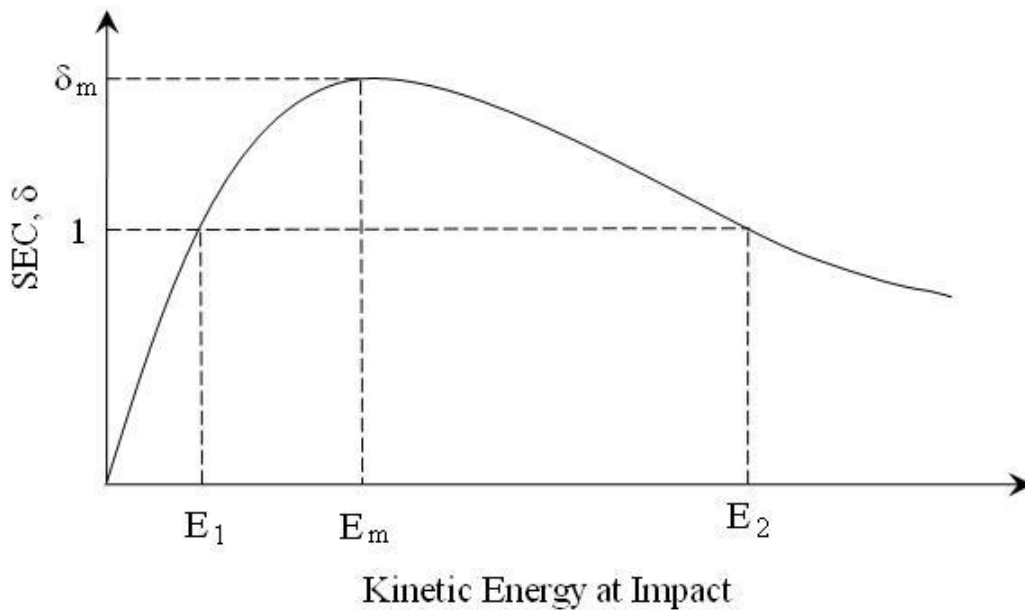


Figure 42: Secondary Emission Curve as a function of Energy

The energy and the emission angle (direction in which electron is emitted) of secondary electrons is assigned using “Monte Carlo method”. The secondary electrons follow Maxwell Distribution [90]. The normalized probability distribution function is given by,

$$f(E) = \left(\frac{2}{\sqrt{\pi}} \right) (2\bar{E})^{-3/2} \sqrt{E} \text{Exp} \left(\frac{-E}{2\bar{E}} \right) \quad (79)$$

The maximum of the probability distribution curve, occurs at $E = \bar{E}$. At $\bar{E} = 2.9 \text{ eV}$, $f(E)$ is maximum that is $f_{max} \sim 0.083$. The energy is assigned to the secondary electron using the rejection method. Two series of uniform random numbers lying between 0 and 1 are generated using Park and Miller algorithm [91]. Let μ_1 and μ_2 be the two random numbers. The energy is given by,

$$E = \mu_1 E_{max} \quad (80)$$

A $f'(E)$ is calculated using equation (79). Using second random number, $f'(E) = \mu_2 f_{max}$ is calculated. If $f'(E) < f(E)$ then random number, μ_1 is accepted and corresponding energy is assigned to the secondary electron. Otherwise the number is rejected and a next pair of random number is generated.

It is assumed that the electrons are generated isotropically about a surface normal. Thus the angle made by an emitted secondary electron with the surface normal is proportional to $\cos^{-1} \eta$, where η is the random number.

The resonant trajectories are tracked for maximum 20 impacts. A “Enhanced Counter Function, ECF” is used to find out whether a particular electron will give rise to the multipacting. ECF is the total number of secondary electrons generated after 20 impacts.

The total number of electrons generated due to single electron after 20 impacts is,

$$N_i = \prod_{k=1}^{20} \delta_k \quad (81)$$

$$ECF = \sum_{i=1}^{N_0} N_i \quad (82)$$

The program calculates the ratio, ECF/N_0 after 20 impacts, where N_0 is the total number of primary electrons that undergo 20 impacts. If the ratio, $ECF/N_0 > 1$ at a given power level then it is a multipacting level. The order of multipacting depends on the time interval between two successive impacts.

5.3] Development of code

The code is written in ‘C’ language. It consists of three programs viz. ‘mulpac1.c’, ‘mulpac2.c’ and ‘mulpac3.c’. A ‘mulpac1.c’ is the main program. It solves the equations of motion of electron, tracks the secondary electrons and calculates the ECF/N_0 . The input is provided by three files, viz, ‘geometry.dat’, ‘mulpac.dat’ and ‘random.dat’.

- (i) **geometry.dat** : It is a data file. The first line reads the dimensions of co-axial coupler a, b, RF frequency. The second line contains minimum and maximum power level and interval ΔP . The third line contains VSWR, the total number of time steps and the total number of primary electrons.
- (ii) **mulpac.dat** : It is a data file containing the information about the position (r_0, z_0), initial velocity (v_r) and the phase of the primary electrons. These values are assigned arbitrarily and it is assumed that $v_z = 0$ for primary electrons at $t=0$.

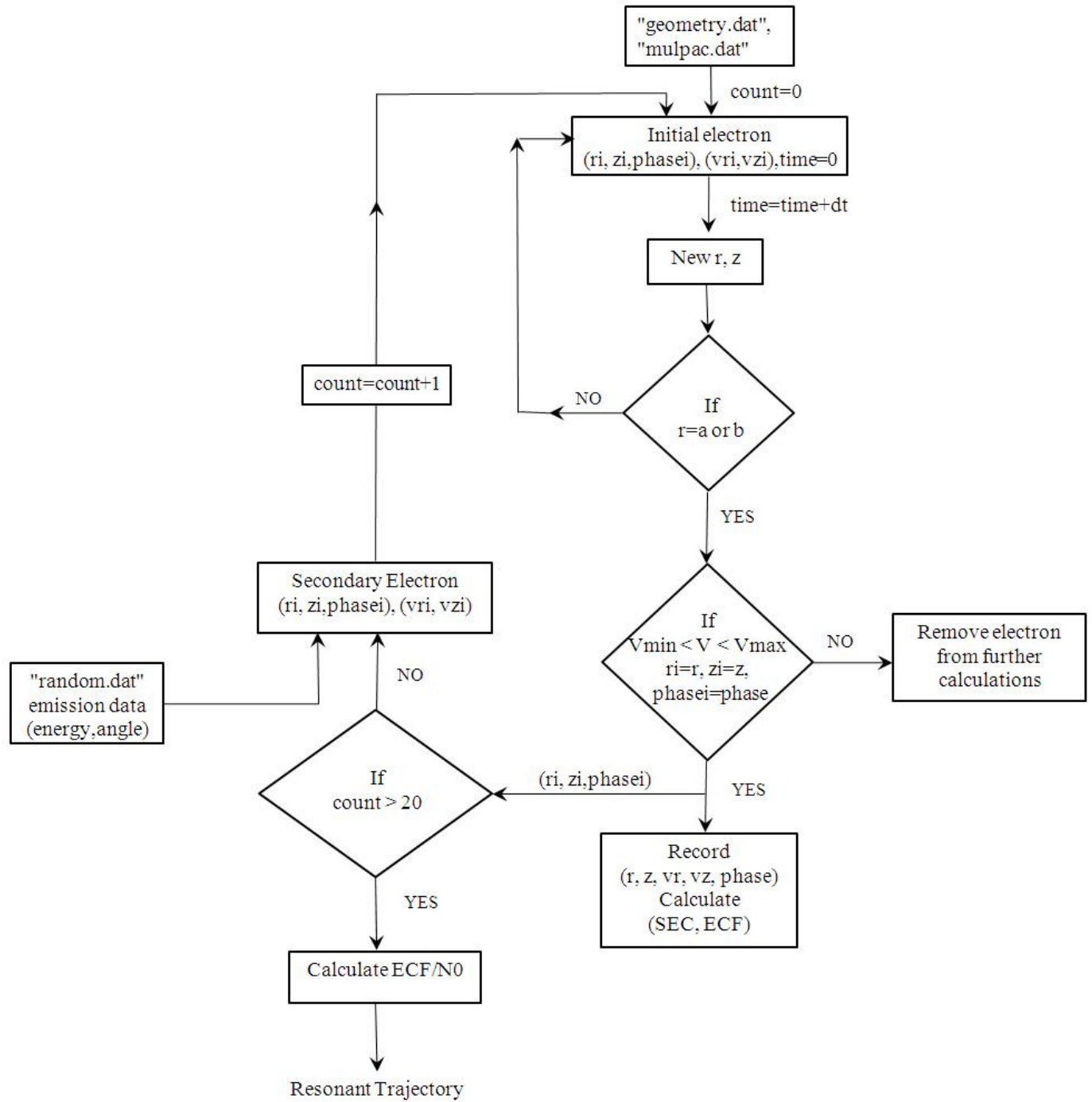


Figure 43: Flow chart of the program

- (iii) **random.dat** : This data file contains the information about the emission energy and the emission angle of secondary electrons. After every impact the emitted secondary electron is assigned an energy and emission angle randomly using this data file.

The 'mulpac.dat' is generated by the program 'mulpac2.c' that serves as an input file to the main program. The file 'random.dat' is an output of the program 'mulpac3.c'. Figure 43 shows the flow chart of the main program for tracking resonant trajectory, the operations shown are performed for each power level defined by the user.

5.4] Results and Discussion

A] Benchmark Calculations: The benchmark calculations were carried out for the TTF III, cold coupler having OD: $\phi 40$ mm and impedance 70Ω operating at 1.3 GHz. The reported results by Ge et. al. and Rusnak and Wang [92,93] using Track 3P and our calculations for the same coupler are compared. Figure 44(a) shows the ECF/ N_0 calculated using our code. The shaded portion indicates the multipacting barriers calculated by Track3P reported in ref. [92]. Our calculations predict the two main barriers near 0.4 MW and 0.7 MW. The Track 3P calculations do predict a multipacting barrier near 0.4 MW but barrier near 0.7 MW is not observed.

b] Simulation Results: The measured secondary electron yield consists of the true secondary, re diffused primary and the elastically scattered electrons. The experiments show that true secondary electron yield is $\sim 58.9\%$ between 0 to 40 eV and follows Maxwell like distribution with peak at 2.9 eV [94]. Thus to generate secondary electrons with Monte Carlo method, an average electron energy of 2.9 eV and maximum electron energy of 40 eV is assumed. (see figure 44 (b))

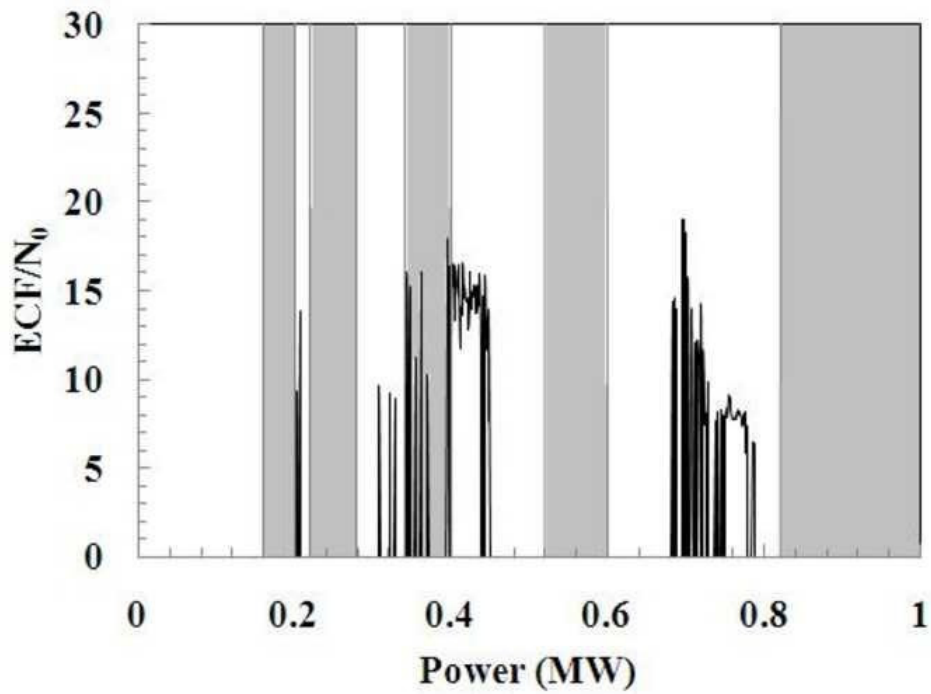


Figure 44 (a): Multipacting barriers calculated for TTF III coupler using our code and Track3P (shaded portion) as quoted in ref. [92]

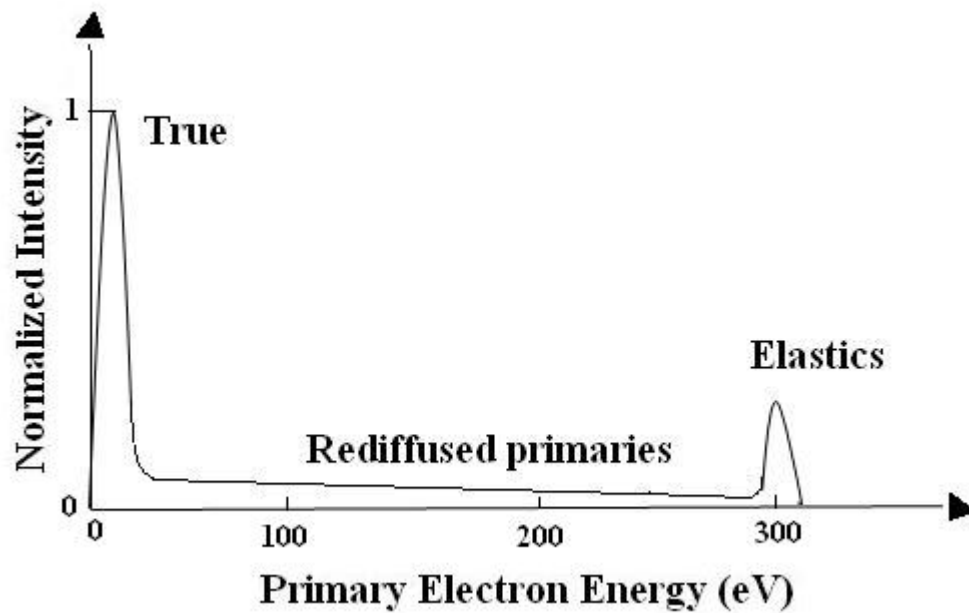


Figure 44 (b): Secondary electron yield

The simulations were carried out for two coaxial couplers, viz. Coupler 1 (ID: $\phi 34.78$ mm, OD: $\phi 80$ mm), Coupler 2 (ID: $\phi 17.38$ mm, OD: $\phi 40$ mm) and Coupler 3 (ID: $\phi 43.48$ mm, OD: $\phi 100$ mm) at a RF frequency of 700 MHz and 1.05 GHz under matched condition (VSWR=1) and under full power reflection (VSWR=10000). Large number of primary electrons (=730) with various initial positions, energy and phases were generated. Figure 45 shows the one point, 3rd order multipacting trajectory in Coupler 2 at a RF frequency of 1.05 GHz of a primary electron started at phase of 0.957 rad. Figure 46 shows the same trajectory of secondary electrons between successive impacts as a function of time which clearly indicates that multipacting order is 3. Figure 47 shows the variation of (ECF/ N_0) with RF power for Coupler 1 under various load or VSWR conditions at a frequency of 700 MHz. At higher VSWR, multipacting is likely to occur at lower power level that is evident from the results. Figure 48 shows the multipacting bands at a frequency of 1.05 GHz for Coupler 1 and Coupler 2, initial electron position is chosen at the electric field maximum. Figure 49 shows the multipacting bands at various frequencies for Coupler 1. From the Figure 48 and figure 49, it is clear that multipacting power level scales with the frequency and the coupler dimensions. Figure 50 shows the multipacting bands for the Coupler 1, at a frequency of 1.05 GHz with initial primary electron position, Z_0 chosen at electric and magnetic field maximum. The multipacting bands are observed between power levels 0.3 MW to 1 MW for the coupler 1 at 1.05 GHz while for the larger coupler 3 at 700 MHz the multipacting bands are observed near 0.3 MW, 0.5 MW and 1 MW, figure 51 shows the multipacting bands for coupler 3 at 700 MHz and 1.05 GHz under standing wave condition.

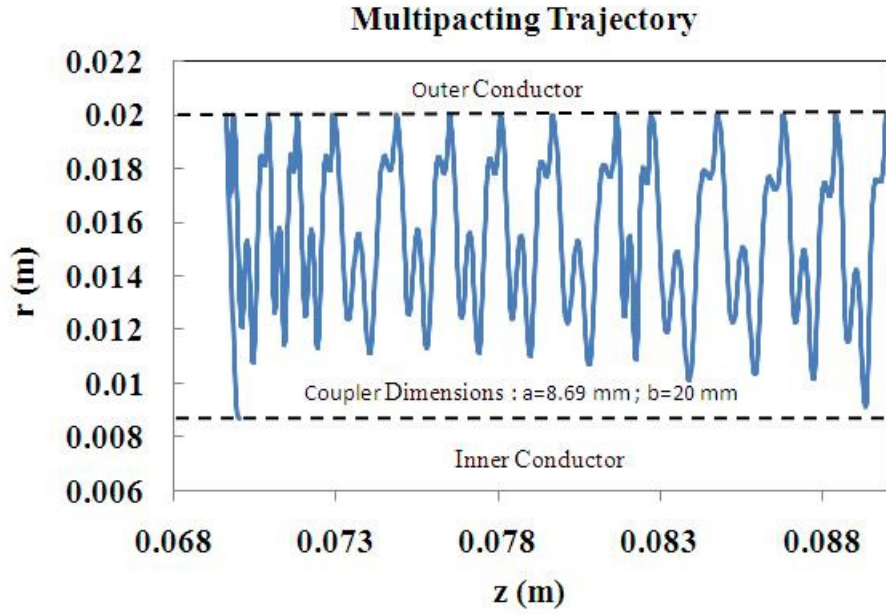


Figure 45: One Point, 3rd order trajectory of coupler 2

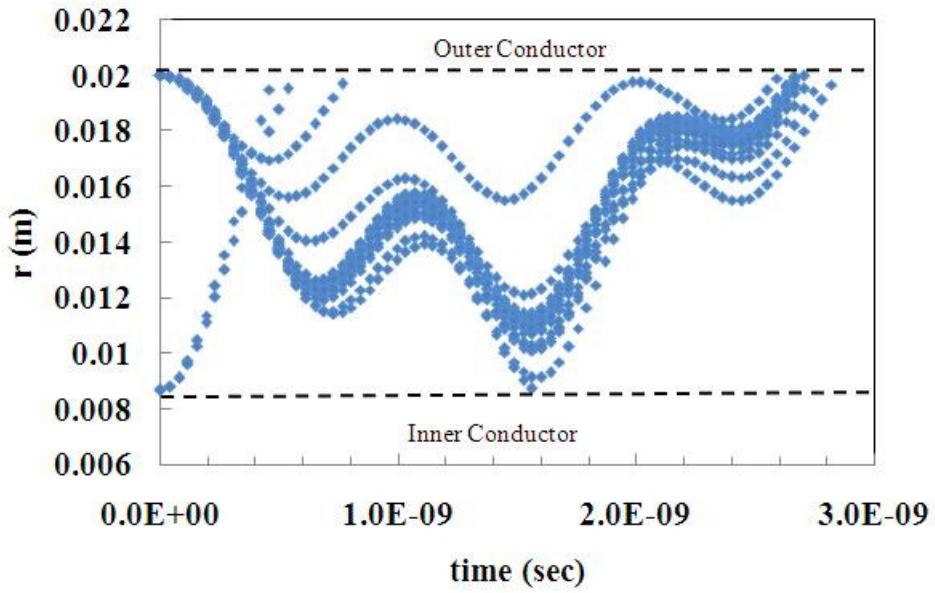


Figure 46: One point, 3rd order trajectory as a function of time of coupler 2

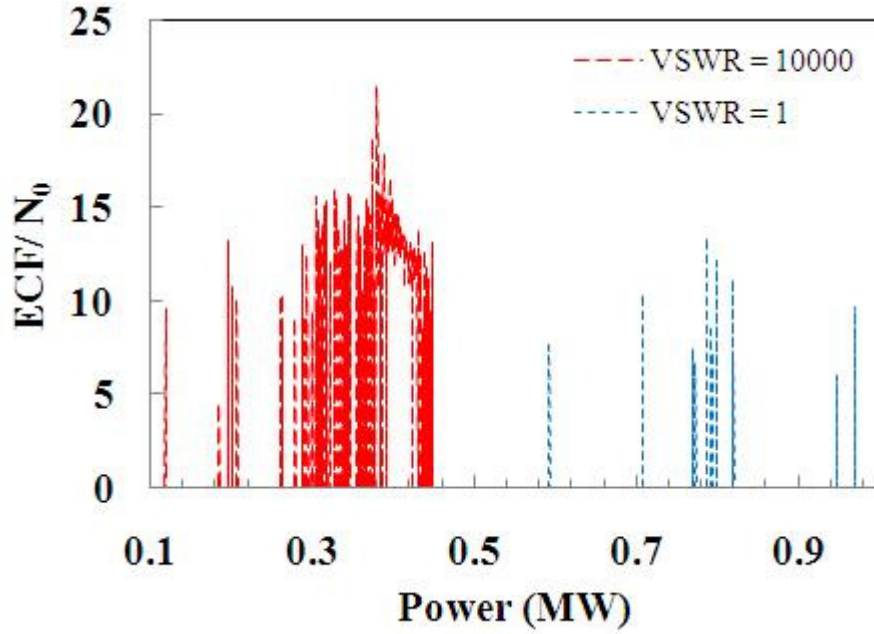


Figure 47: Multipacting bands of coupler 1 calculated for different loads

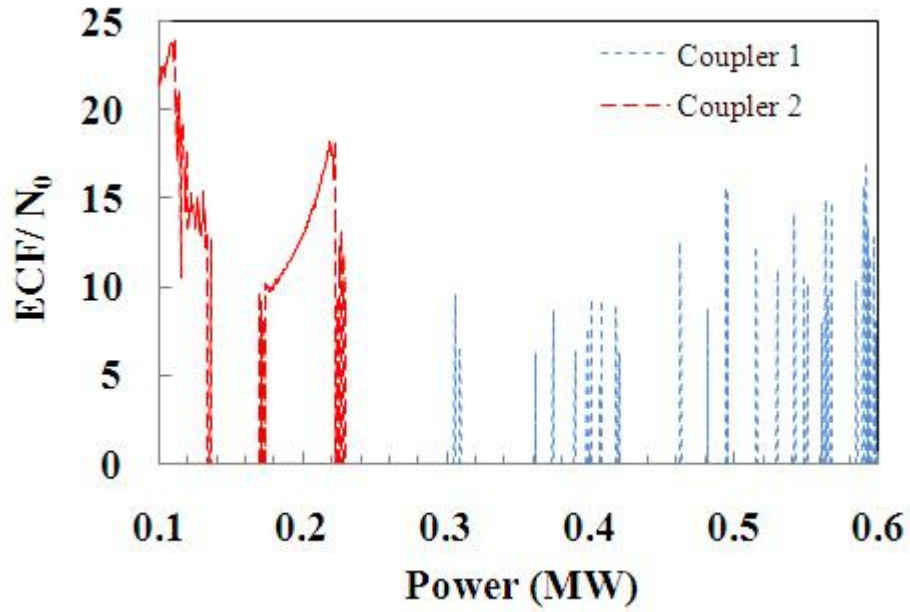


Figure 48: Multipacting bands for different coupler size at a frequency of 1.05 GHz

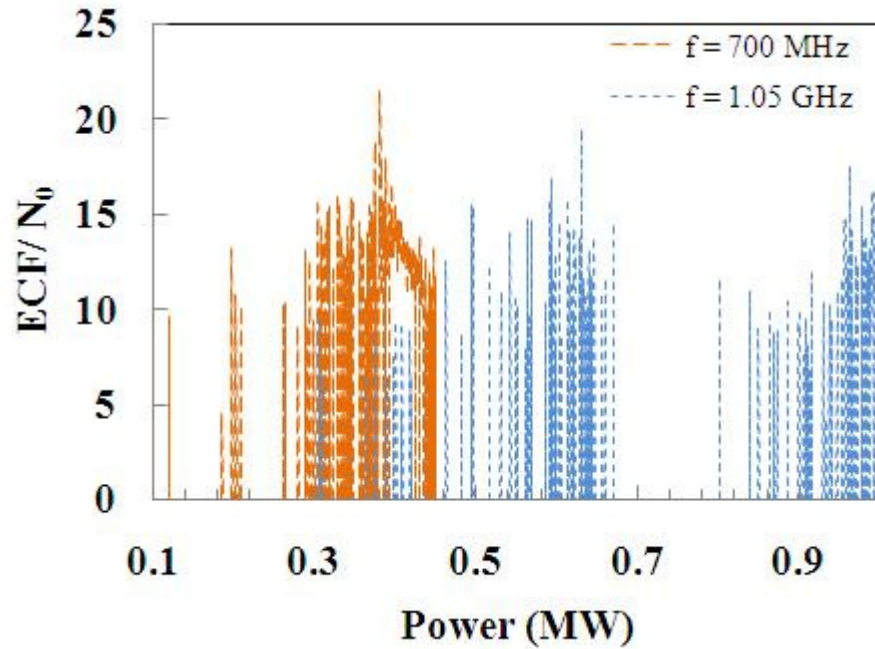


Figure 49: Multipacting band calculated for coupler 1 at different frequencies

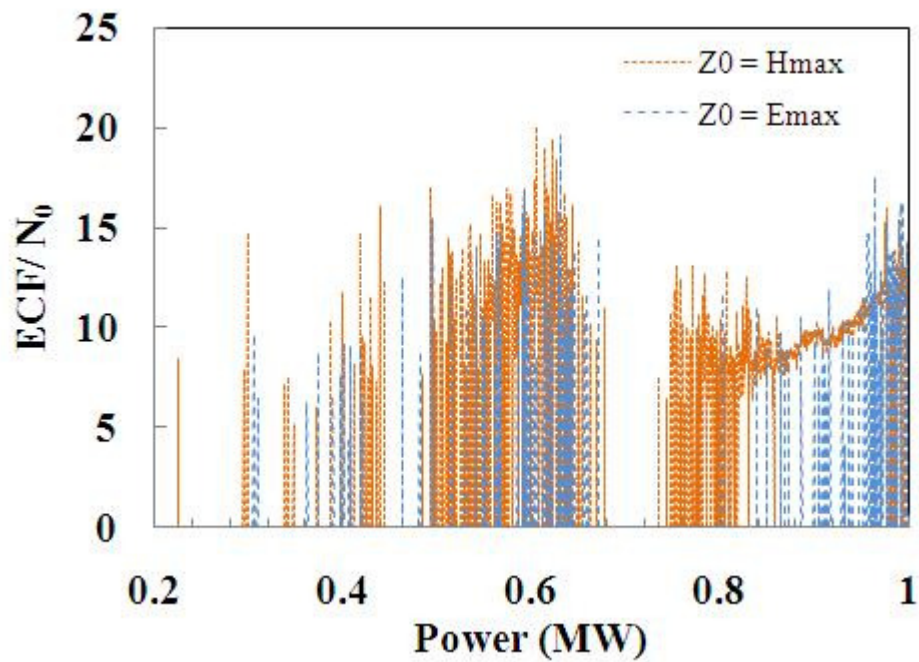


Figure 50: Multipacting bands of coupler 1 calculated at 1.05 GHz at different initial position

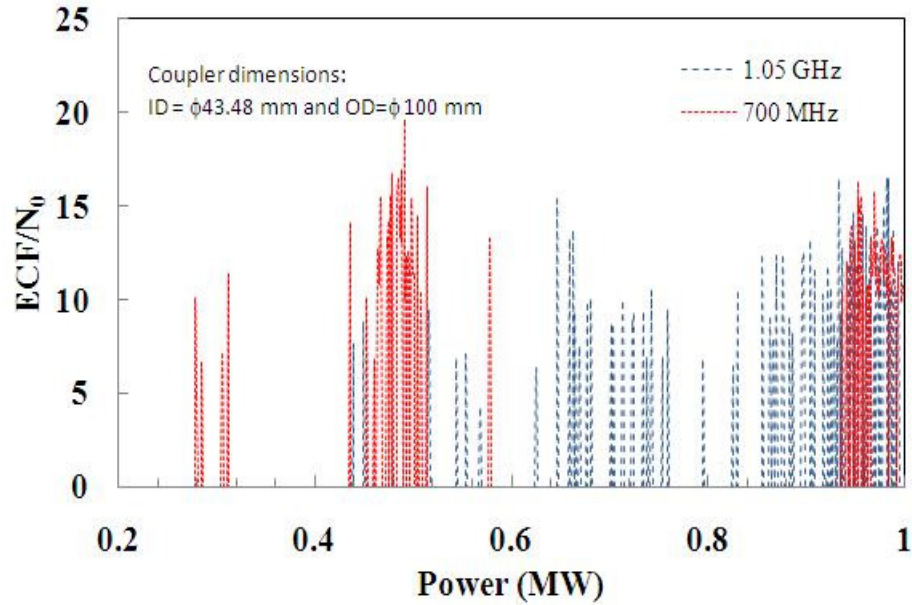


Figure 51: Multipacting bands of coupler 3 at different frequencies calculated under standing wave condition.

5.5] Conclusion

The validation of program was carried out by calculating the multipacting for different coupler sizes at different frequencies under various operating conditions. P. Yla-Oijala has given the scaling laws for couplers based on operating frequency and the dimensions.

The scaling law for the one point multipacting of co-axial coupler is given by [95],

$$P \propto (f d)^4 Z_0 \quad (83)$$

Where, ‘ f ’ is the RF frequency in GHz, ‘ d ’ is the outer conductor diameter of coaxial in mm and ‘ Z_0 ’ is the characteristics impedance which is 50Ω in this case. Table 10 shows the comparison of the multipacting bands predicted by the code and the scaling law. The results obtained from code are in good agreement with the scaling law.

Table 10: MP power levels estimated by code and from scaling law

Coupler 3, 700 MHz		Coupler 1, 1.05 GHz	
P(MW) by scaling law	P (MW) by code	P(MW) by scaling law	P (MW) by code
0.1 - 0.18	-	0.27	0.32
0.24 - 0.33	0.28 - 0.32	0.4	0.36 - 0.42
0.6	0.44 - 0.56	0.67	0.48 - 0.66
1.33	0.96 to > 1	1.1	0.84 to > 1

Some of the recent work done on the multipacting of coaxial geometries like quarter wave resonator has shown that the trajectories that are stable in r-z plane are more dangerous as they are confined to narrow region and will sustain for longer period compared to the trajectories that are walking in z-direction [96]. In our case, the observed trajectories are walking in z-direction and since in practice coupler will have finite dimensions, trajectories may die and would not lead to any serious multipacting breakdown. Any soft barriers, if exist can be overcome by rf conditioning.

Other remedies involve the application of DC bias voltage on the inner conductor [53,97] or the coating of Ti or TiN on the surface, especially it is useful to avoid the multipacting in ceramic window [98]. Figure 52 shows the multipacting trajectory of a resonant electron in coupler 1 at 700 MHz, at a power level of 0.43 MW, starting from the position of maximum electric field at a phase of 1.131 rad simulated by code. The application of DC bias voltage disturbs the resonant condition. The figure shows decaying trajectory of the resonant electron due to successive increase in bias voltage. The multipacting was fully quenched by application of -8 kV bias voltage at all the power levels shown in figure 49 at 700 MHz while at higher

frequency of 1.05 GHz, bias voltage of -9 kV is required. Similarly for complete removal of multipacting in coupler 3, bias voltage of -9 kV at 700 MHz and -10 kV at 1.05 GHz is required as simulated by the code.

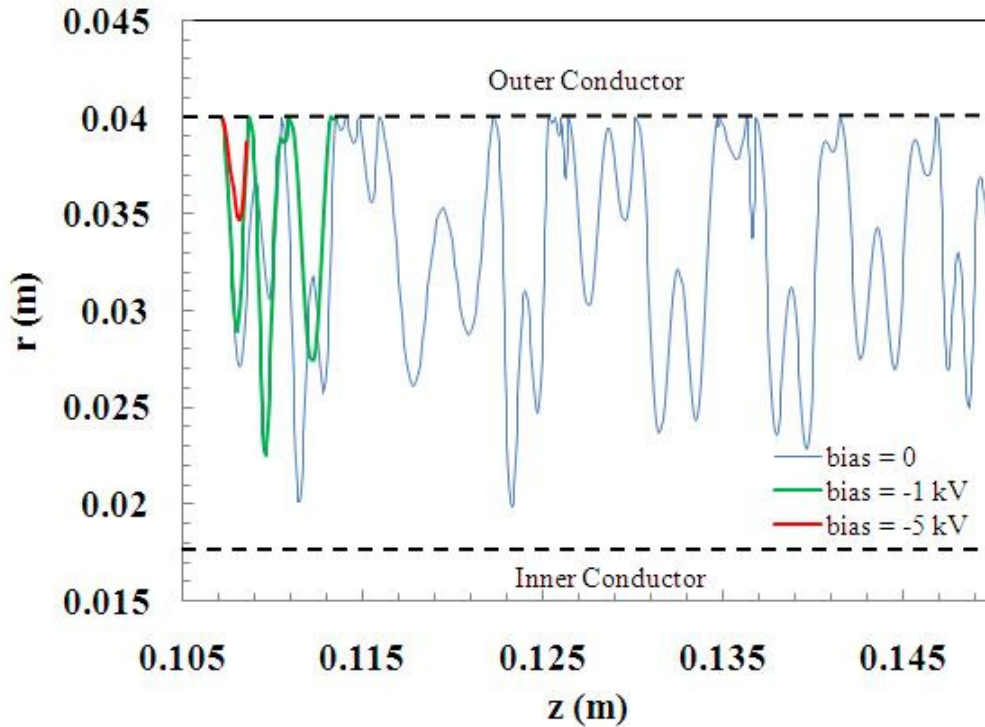


Figure 52: Multipacting trajectory of coupler 1 at 700 MHz at different DC bias voltages

The analysis of other coupler components like door-knob transition, ceramic window or waveguide bends require 3-d codes. The present code and the studies carried out so far serve as the basis for the future work.

CHAPTER 6

STUDY OF MATERIALS FOR CAVITY PRODUCTION

6.1] Introduction

The future of the accelerators relies on superconducting cavity technology due to the requirement of high accelerating gradients with low losses. Various surface treatments such as buffered chemical polishing (BCP), electropolishing (EP), low-temperature baking (LTB) are carried out on the cavities in order to improve the performance. In particular, a low temperature baking at a temperature of 120 °C and for the duration of 12 - 48 hr after BCP or EP was found to be beneficial in reducing the so-called high field Q-slope (HFQ) [99]. Cavities treated by EP and LTB typically reach higher accelerating gradients than those treated by BCP and followed by LTB. Nevertheless, the underlying mechanism causing the HFQ and the improvement after baking is still unclear.

Since 2005, large-grain Nb has emerged as an alternative material to fabricate high performing SRF cavities in a cost-effective way [100]. In the past few years, Jefferson Lab has been collaborating with CBMM to study the superconducting and thermal properties of large-grain Nb samples cut from ingots of different purity, in an attempt to optimize the ingot production with respect to material processes relevant to SRF cavity production and cost. Here, the results of measurements of thermal conductivity, DC magnetization, critical temperature and AC penetration depth on four large-grain Nb samples of different purity, after EP and LTB. For comparison, the same measurements were done on a standard high-purity fine-grain Nb sample which underwent the same treatments.

6.2] Experimental Setup

A system was developed at Jefferson Lab to measure superconducting properties of the cylindrical samples, as described in [101]. The cylindrical samples are 120 mm long and have a

outer diameter ~6 mm. A channel about 2 mm diameter, 115 mm long was drilled concentric to the sample. The demagnetization factor, N_d , is nearly zero (~0.007). The sample is clamped on a flanged copper block. Two heaters were clamped at the sample ends (distance ~70 mm) and in between two Cernox temperature sensors were also clamped to the samples (distance ~ 34 mm). In the center of the sample a pick-up coil (~150 turns, length ~30 mm, 0.28 mm diameter copper wire) was inserted as shown in figure 53. The whole assembly was inserted in a copper tube that is brazed to a stainless steel pipe having a Conflat flange at one end. The indium wire provided the vacuum sealing between two copper flanges. The inside of the Cu tube is evacuated to a pressure lower than 10^{-4} mbar. The assembly was bolted to a vertical test stand and is concentric to a superconducting magnet that could provide longitudinal magnetic field up to 1 T (0.1% field homogeneity over the sample length). The measurements were carried out on the large-grain (LG) niobium samples machined from ingots with different impurity concentrations (mainly different Ta content) labeled A, B, C and D from CBMM, Brazil, as well as a fine-grain (FG) niobium sample from Wah Chang having grain size ~50 μm and residual resistivity ratio, RRR , greater than 250.

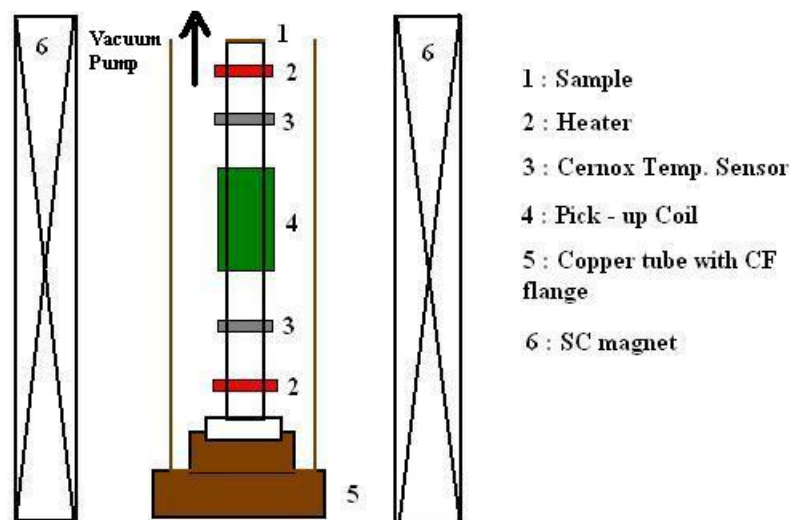


Figure 53: Schematic of the experimental setup.

6.2.1] Sample Preparation

The samples are labeled according to the ingot from which they were machined. The expected value of RRR from the chemical analysis of the ingots, for the various samples is shown in Table 11. Initial treatments on the samples are described in [102]. The samples surface treatments and test sequence were as follows:

- (1) Baseline measurements were carried out on the samples that were previously etched by BCP and baked at 160 °C for 12 h.
- (2) The samples were electropolished with HF:H₂SO₄ (1:10) solution. Figure 54 shows a schematic of the apparatus used to carry out the electropolishing and Figure 55 shows the I-V characteristics for sample A. The EP was carried out for 100 min (~ 50 μm removal) at a voltage of 12 V. The temperature of the acid was maintained at ~17-18 °C using a cold water bath. The same parameters were maintained for the EP of all the samples.
- (3) The samples were baked at a temperature of 120 °C for 48 h in ultra-high vacuum (~10⁻⁹ mbar).

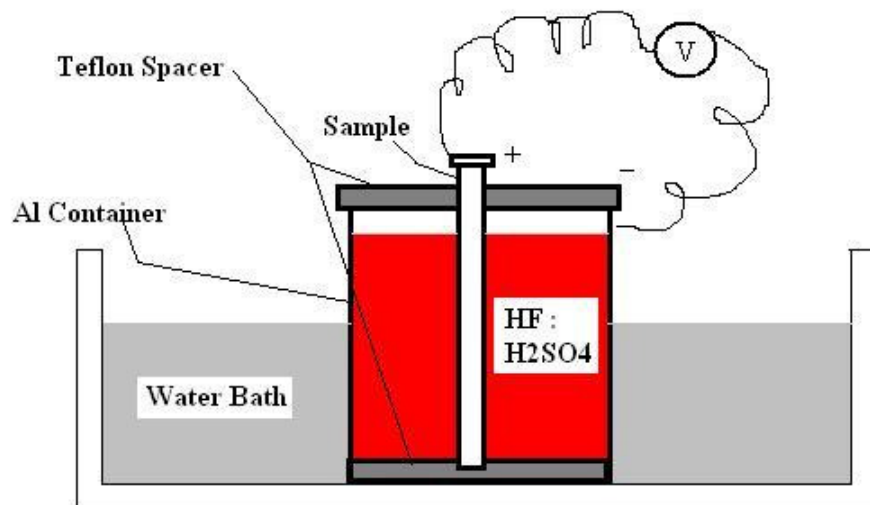


Figure 54: Schematic of the EP setup.

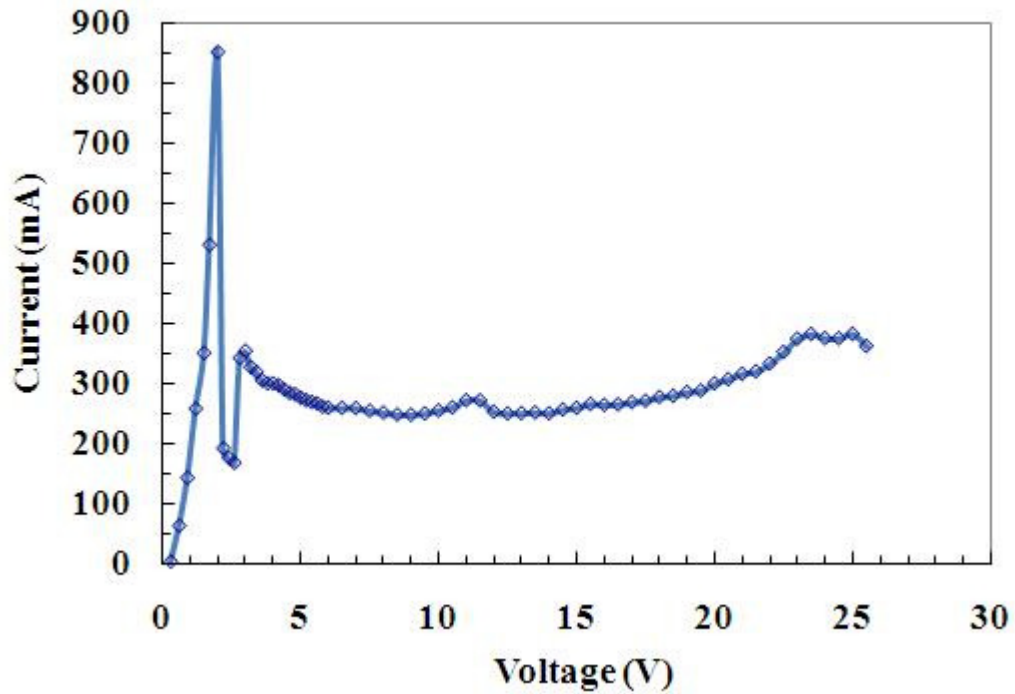


Figure 55: Typical I-V curve for the EP of the samples.

6.3] Experimental Methods

6.3.1] Thermal Conductivity Measurement

A temperature controller (Lakeshore, model 332) is used for this measurement. A known amount of power is set in the top heater mounted on the sample. The opposite side of the sample is in contact with a He bath through the Cu block. The actual power, P , set in the heater is measured by measuring the voltage and current using a multimeter (Keithley, model 2000). Upon reaching thermal equilibrium, the temperature of the top and bottom sensor is recorded. The thermal conductivity is calculated using Fourier's law:

$$\kappa = \left(\frac{P}{\Delta T} \right) \left(\frac{d}{A} \right) \quad (84)$$

where, ΔT is the temperature difference between top and bottom temperature sensor, d is the distance between two temperature sensors and A is the cross-sectional area of the sample

6.3.2] Magnetization Measurement

The DC magnetization measurement was carried out using a single-coil magnetometer method, as described in [103]. The magnetic field of the superconducting coil was ramped linearly at a rate of 3.9 mT/s. The induced voltage generated in the pick-up coil is recorded with a nanovoltmeter (Keithley, model 2182). Figure 56 shows the recorded voltage as a function of applied magnetic field for sample A after EP, as the magnetic field is ramped up from 0 to +H. The highest peak corresponds to the onset of flux penetration, H_{ffp} , while the small peak indicates the upper critical field, H_{c2} . In some cases, additional voltage peaks between H_{ffp} and H_{c2} , associated with flux-jump, were measured. The magnetization, M , as a function of the applied field, H_a , is calculated by using the following equation 85:

$$M(H_a) = \left(\frac{-1}{1 - N_d} \right) \int_0^{H_a} \frac{V(H') - V_n}{V_s - V_n} dH' \quad (85)$$

where V_s and V_n indicate the voltages in the superconducting and the normal conducting state, respectively.

Magnetization measurements were carried out in the zero-field cooled (ZFC) state at different temperatures of the sample, between 2 K and 8 K. After a measurement at a certain temperature, the field in the magnet was turned off, the sample warmed above the critical temperature, T_c , and then ZFC to the next temperature value.

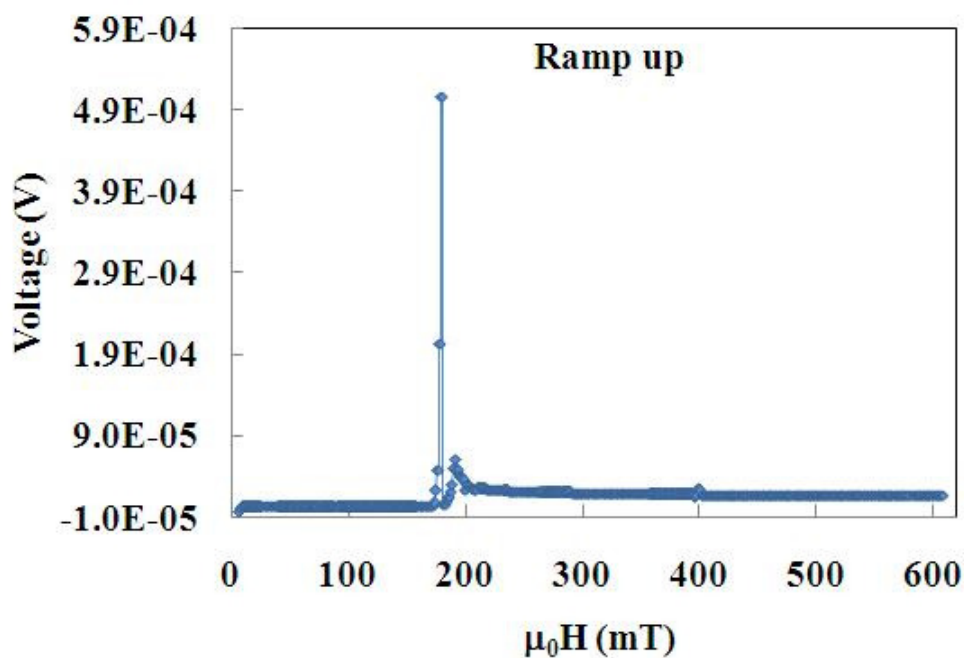


Figure 56: Measured voltage from the pick-up coil as a function of the applied magnetic field during a ramp-up of the field from 0 mT to 600 mT.

6.3.3] Measurements of Surface Superconductivity

The same pick-up coil used for the magnetization measurements is connected to an external capacitor to form an L-C resonant circuit. An AC current of peak value equal to 31 mA ($I_{\text{rms}} \sim 22$ mA) flows in the pick-up coil, therefore generating a small AC magnetic field which is superimposed parallel to the DC magnetic field generated by the superconducting magnet. The inductance change of the pick-up coil, as a result of a change of the penetration depth in the Nb sample due to either the applied DC magnetic field or the temperature of the sample, results in a change of the resonant frequency of the L-C circuit. This measurement technique has been used since the 1960's-70's to measure the penetration depth of superconducting samples as a function of temperature [104] and field [105].

The measurements were carried out on ZFC samples in an applied DC magnetic field from 0 to 1 T, ramped at a rate of 3.9 mT/s. The capacitor used in the L-C oscillator had a typical

capacitance value of 30 nF, corresponding to a resonance frequency of ~ 270 kHz in the superconducting state. This corresponds to sampling about 30 μm from the surface. The measurements were repeated at different temperatures ranging from 2 K to 8 K. After every measurement the sample was warmed up to 9.3 K and zero-field cooled. Figure 57 shows the oscillator frequency change as a result of varying magnetic field at a temperature of 4 K for sample D that was treated by BCP and baked at 160 $^{\circ}\text{C}$, 12 h. The “hysteresis loop” between H_{fp} and H_{c2} is related to the surface pinning. Above H_{c2} , the bulk of the sample is in normal state but the surface superconductivity persists till the surface critical field, H_{c3} . The ratio H_{c3}/H_{c2} is temperature dependent and it is equal to 1.925 at 2.0 K [106].

A measurement of T_c is done inductively, by measuring the frequency of the oscillator as a function of the sample temperature, with no magnetic field applied. An example of such measurement is shown in figure 58 for sample D after BCP and baking at 160 $^{\circ}\text{C}$, 12 h.

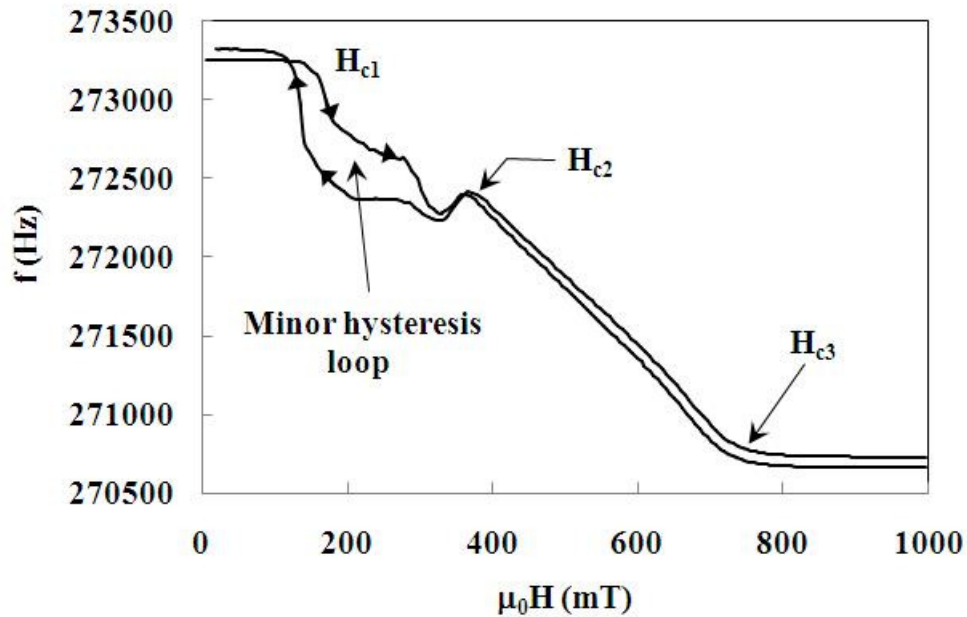


Figure 57: Frequency change measured during ramp-up and ramp-down of the applied magnetic field at 4 K.

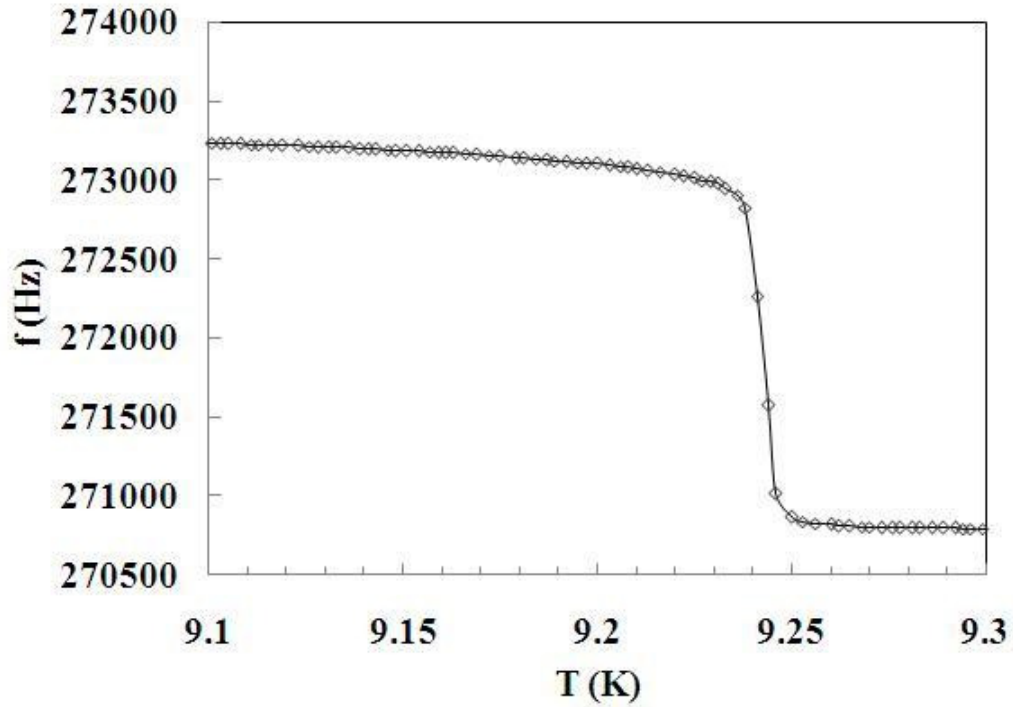


Figure 58: Frequency change measured during warm-up of sample D in zero applied field allowing measuring the critical temperature

6.4] Experimental Results

6.4.1] Thermal Conductivity

Figure 59 shows the plots of the thermal conductivity, κ , as a function of temperature for samples D and FG after EP and LTB at 120 °C for 48 h. The RRR-value of the samples is obtained from the thermal conductivity at 4.3 K, using the rule-of-thumb $RRR \cong 4 \times \kappa (4.3\text{K})$. Table 11 shows a comparison of the calculated RRR values and those obtained from a chemical analysis of the ingots.

Table 11: RRR and Ta concentration from the chemical analysis of the samples and calculated from the thermal conductivity at 4.3 K measured on the samples treated by EP.

Sample	Ta content (wt-ppm)	RRR from chemical analysis	RRR from thermal conductivity
A	1295	97 ± 10	62 ± 7
B	1310	150 ± 27	164 ± 7
C	600	114 ± 15	159 ± 21
D	970	145 ± 25	118 ± 12
FG	100	>250	280 ± 30

6.4.2] DC Magnetization

Figure 60 shows the magnetization measurements carried out at 2 K on sample D after various surface treatments. Similar results were obtained from the measurements of the other samples. Table 12 shows the measured critical fields at 2 K for all the samples with various surface treatments. The estimated experimental errors in the determination of H_{ffp} and H_{c2} are about 2 mT and 10 mT, respectively. Since the lower critical field, H_{c1} , is defined for a reversible magnetization curve, which is not the case for our measurements, we refer to the field which corresponds to the deviation from the perfect diamagnetism as the “field of first flux penetration”, H_{ffp} , as discussed in [107]. This field corresponds to the zero-threshold in a plot of $\mu M(H)$ vs. H . The question whether H_{ffp} is actually larger or smaller than H_{c1} will depend on the surface barrier, which depends on roughness and impurities near the surface.

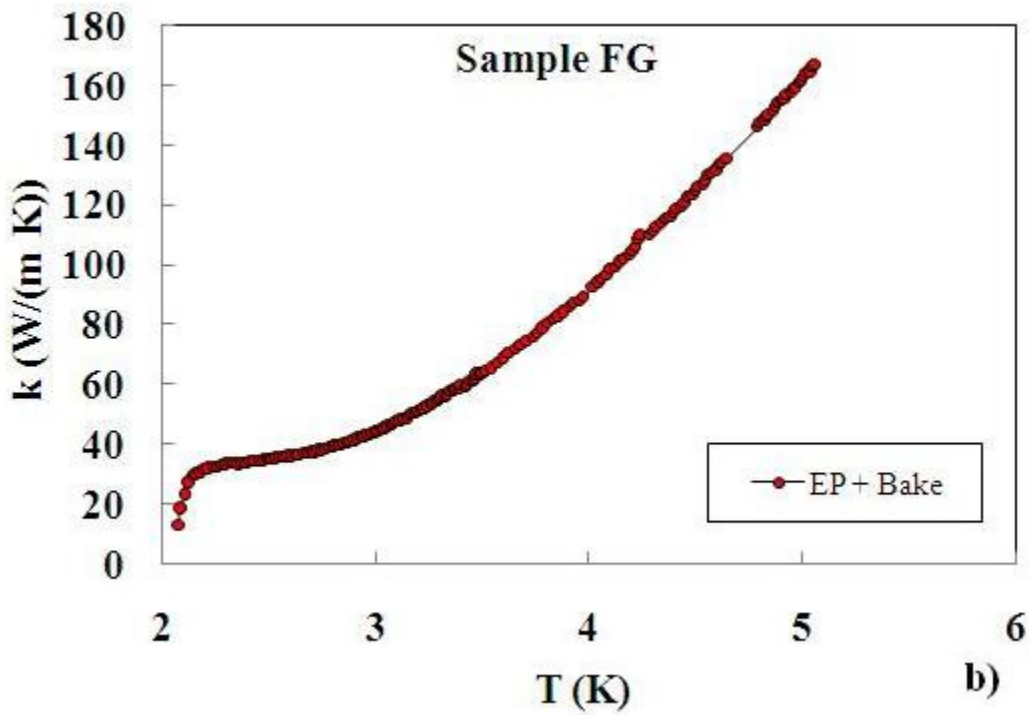
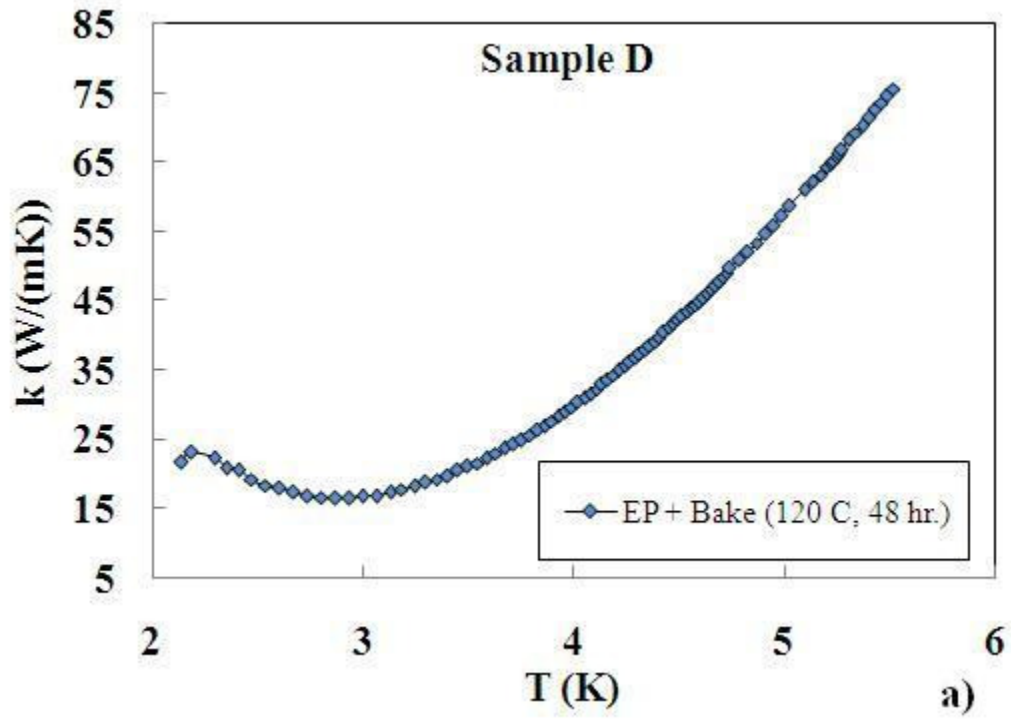


Figure 59: Thermal conductivity as a function of temperature measured on samples D (a) and FG (b) after EP and LTB.

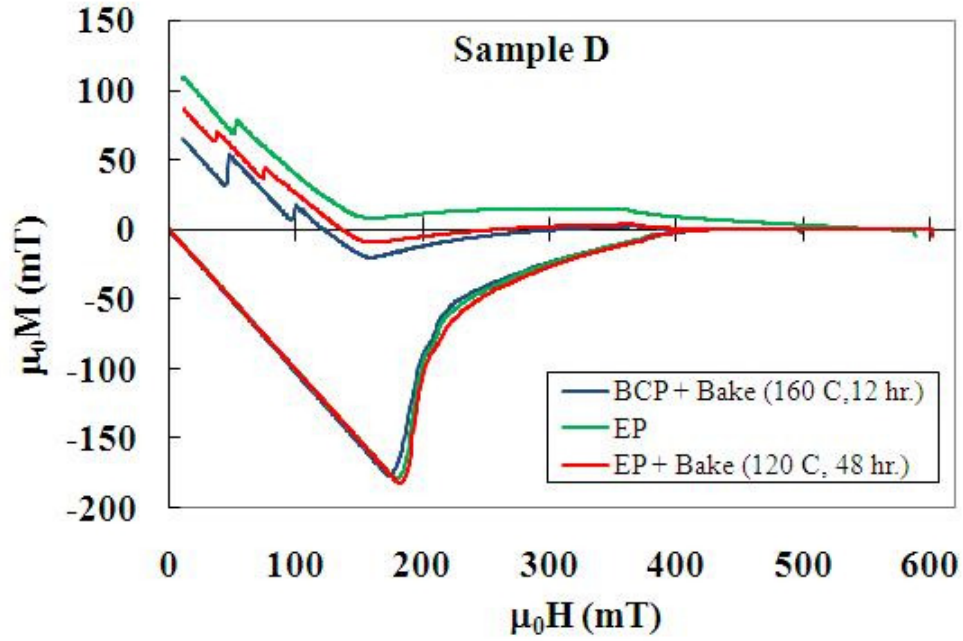


Figure 60: Magnetization as a function of the applied field measured on LG sample D at 2.0 K after different surface treatments

Table 12: Comparison of H_{ffp} and H_{c2} at 2 K after EP and LTB

Sample	EP		EP + LTB (120 °C, 48 h)	
	H_{ffp} (mT)	H_{c2} (mT)	H_{ffp} (mT)	H_{c2} (mT)
A	174	405	177	390
B	182	400	184	400
C	179	400	180	400
D	186	405	188	420
FG	183	380	183	400

The temperature of the samples was set to different values between 2 K and 8 K by using the top and bottom heaters mounted on the sample and magnetization measurements were

repeated for each temperature value. The power to the heaters is controlled by the PID control loop of the temperature controller to maintain the temperature of the sample within a range of ± 0.2 K about the set point. Figure 61 shows the critical fields H_{ffp} and H_{c2} as a function of temperature for LG sample D and for the FG sample. The temperature dependence of the critical fields is fitted using the following equations [108]:

$$H_{ffp}(T) = H_{ffp}(0)(1 - t^2) \quad (86)$$

$$H_{c2}(T) = H_{c2}(0) \left(\frac{1 - t^2}{1 + 0.4t^2} \right) \quad (87)$$

where $t = T/T_c$ is the reduced temperature. Table 13 lists the fitted values of $H_{ffp}(0$ K), $H_{c2}(0$ K) and T_c for the samples treated by EP. The experimental values of transition temperature quoted in the Table 13 were measured inductively, as described earlier. The values of $H_{ffp}(0$ K), $H_{c2}(0$ K) and T_c for the samples after LTB are listed in Table 14.

Table 13: Fitted values of $H_{ffp}(0$ K), $H_{c2}(0$ K) and T_c after EP. The experimental value of T_c is also indicated for comparison.

Sample	EP				
	$H_{ffp}(0)$ (mT)	T_c (K) (fit)	$H_{c2}(0)$ (mT)	T_c (K) (fit)	T_c (K) (expt.)
A	187.5	9.245	438.0	9.245	9.217
B	184.0	9.090	410.1	9.170	9.251
C	193.8	9.245	444.4	9.170	9.247
D	189.1	9.130	456.0	9.325	9.245
FG	192.5	9.366	427.4	9.325	9.366

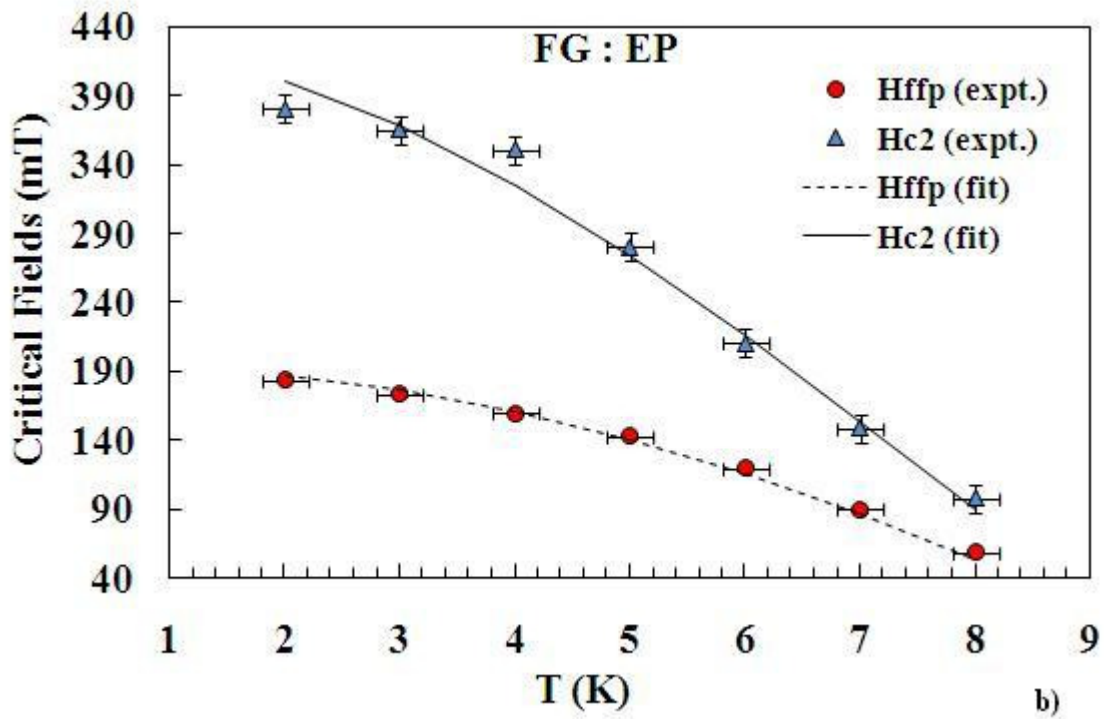
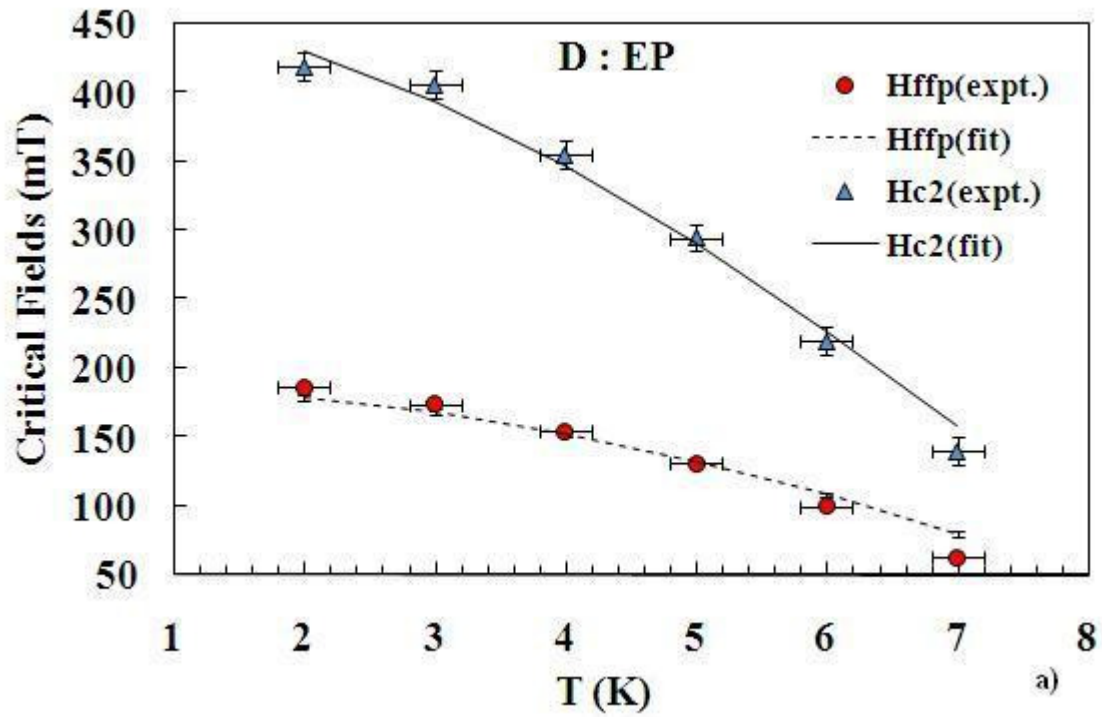


Figure 61: Critical fields as a function of temperature from DC magnetization methods for sample D (a) and FG (b) after EP. The data were fitted with Eqs. (4) and (5).

Table 14: Fitted values of $H_{\text{fp}}(0 \text{ K})$, $H_{c2}(0 \text{ K})$ and T_c after LTB at 120 °C for 48 h. The experimental value of T_c is also indicated for comparison.

Sample	EP + LTB (120 °C, 48 h)				
	$H_{\text{fp}}(0)$ (mT)	T_c (K) (fit)	$H_{c2}(0)$ (mT)	T_c (K) (fit)	T_c (K) (expt.)
A	190.1	9.217	446.9	9.218	9.218
B	198.9	9.258	449.4	9.258	9.258
C	192.9	9.240	435.0	9.245	9.240
D	192.4	9.245	451.3	9.245	9.244
FG	197.1	9.270	430.6	9.245	9.270

6.4.3] Surface Superconductivity

Measurements of the frequency shift, δf , of the L-C circuit as a function of the applied DC magnetic field, H , were carried out for all samples in the ZFC state at various temperatures, between 2 K and 8 K. Figure 62 shows the data for samples C and FG after different surface treatments. The critical fields H_{fp} , H_{c2} and H_{c3} are clearly visible from the data.

By plotting the derivative of δf with respect to H as a function of H it is possible to identify the various critical fields as those at which a change of the slope of $d(\delta f)/dH$ occurs. In particular, it is possible to obtain the so-called “coherent surface critical field”, H_{c3}^c [109], between H_{c2} and H_{c3} . This field is considered a field up to which a long-range, coherent superconducting phase is present at the surface. The values of the critical fields at 2.0 K, measured within a surface layer $\sim 30 \mu\text{m}$ thick for the various samples after EP and LTB are listed in Table 15.

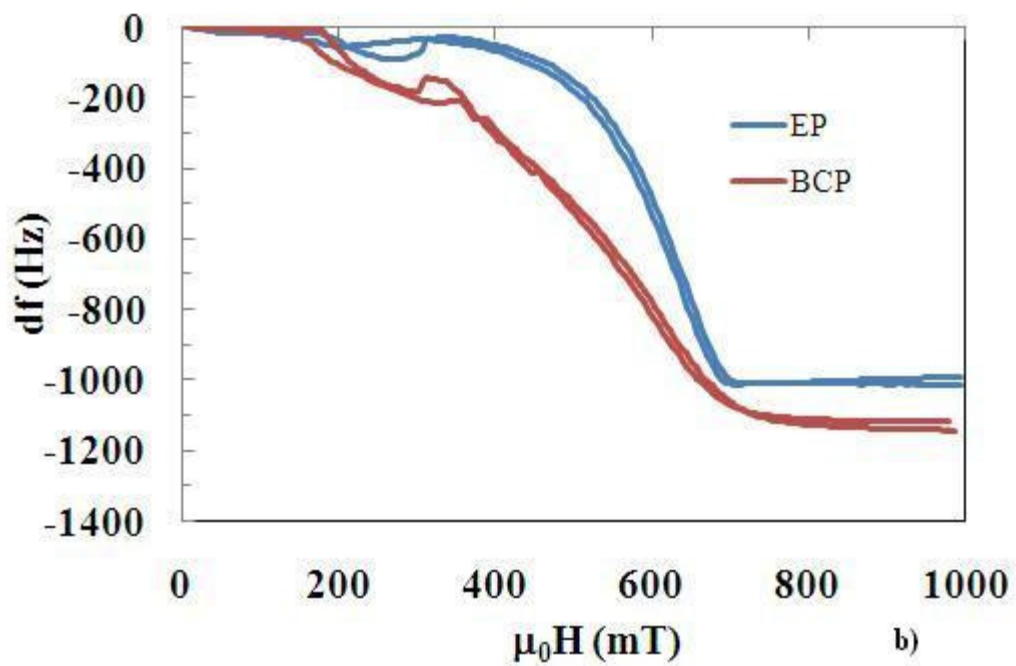
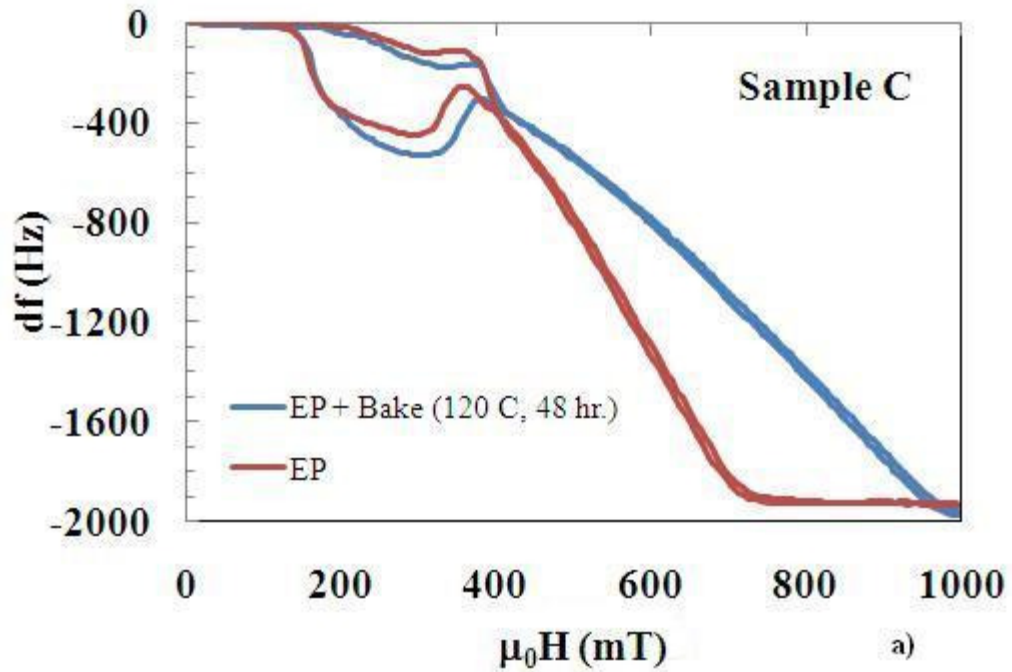


Figure 62: Frequency shift vs. H for sample C after EP and LTB (a) and for sample FG (b) after BCP and EP.

Table 15: Critical fields in a ~30 μm depth from the surface measured at 2 K, after EP and LTB

Sample	EP				EP + LTB			
	H_{ffp} (mT)	H_{c2} (mT)	H_{c3} (mT)	H_{c3}^c/H_{c3} 3	H_{ffp} (mT)	H_{c2} (mT)	H_{c3} (mT)	H_{c3}^c/H_{c3}
A	162	322	749	0.89	175	351	850	0.87
B	175	317	705	0.89	180	381	>1000	< 1.0
C	160	331	753	0.87	168	351	1000	0.9
D	160	330	740	0.9	166	347	750	0.93
FG	164	301	700	0.93	170	320	>1000	0.93

6.4.4] Critical Current Density, J_c

The critical current density, J_c can be derived from the magnetization loop using the Bean critical state model and is proportional to the width of the magnetization during ramp up or ramp down of the applied magnetic field [110-112]. J_c was calculated from magnetization measurement using equation (88) under the assumption of full flux penetration,

$$J_c = \frac{3}{2}(M_+ - M_-) \left(\frac{b_s^2 - a_s^2}{b_s^3 - a_s^3} \right) \quad (88)$$

where, M_+ is Magnetization during ramp-up, M_- is Magnetization during ramp-down, b_s is the outer radius and a_s is the inner radius of the sample. Figure 63 (a) and (b) shows the variation of J_c with reduced magnetic flux density, b ($=B/B_{c2}$). The maximum J_c , $J_{c,max}$ scales with the temperature. The experimental results were fitted with the following equation [113],

$$J_c = J_c(0)(1-t)^K \quad (89)$$

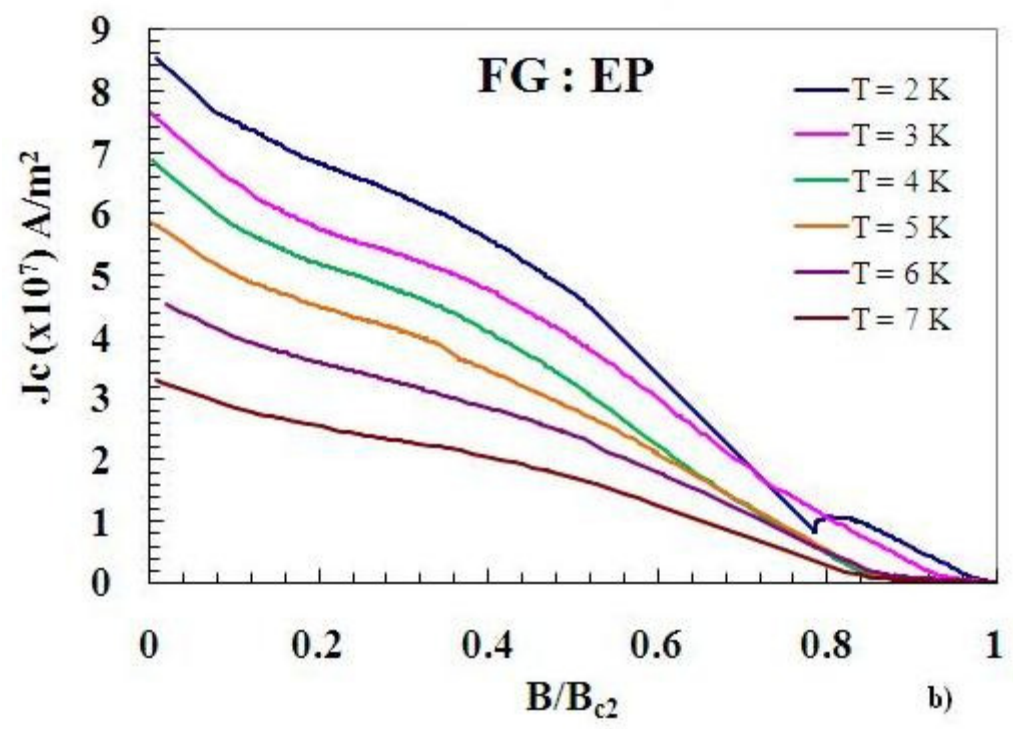
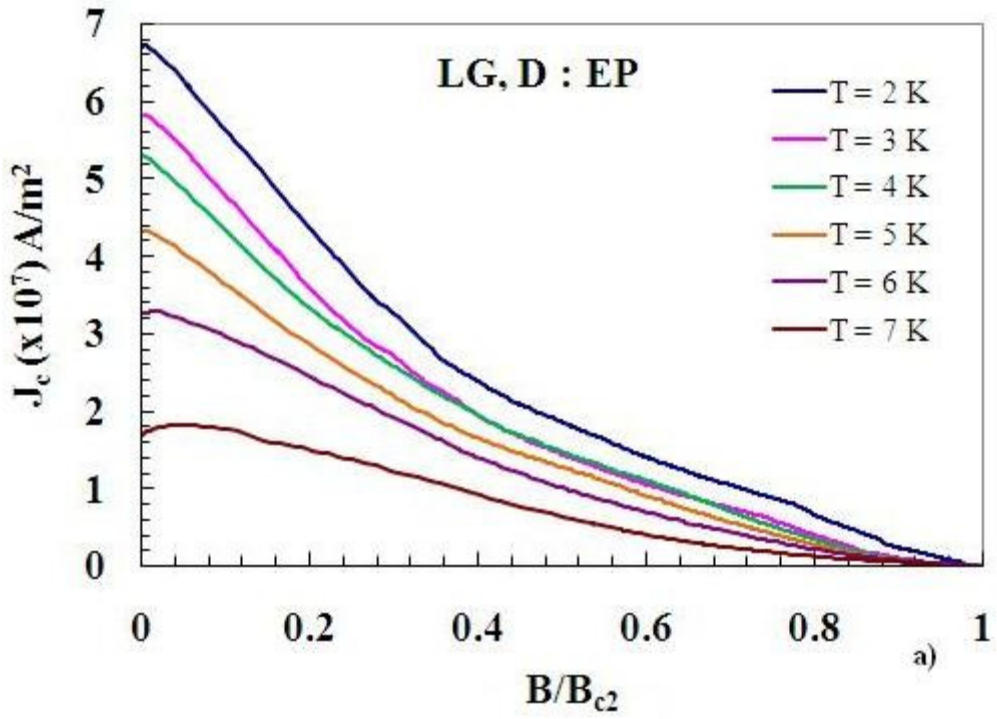


Figure 63. Plot of Critical current density as a function of reduced magnetic flux density, b ($=B/B_{c2}$) at different temperatures for (a) sample D, (b) FG

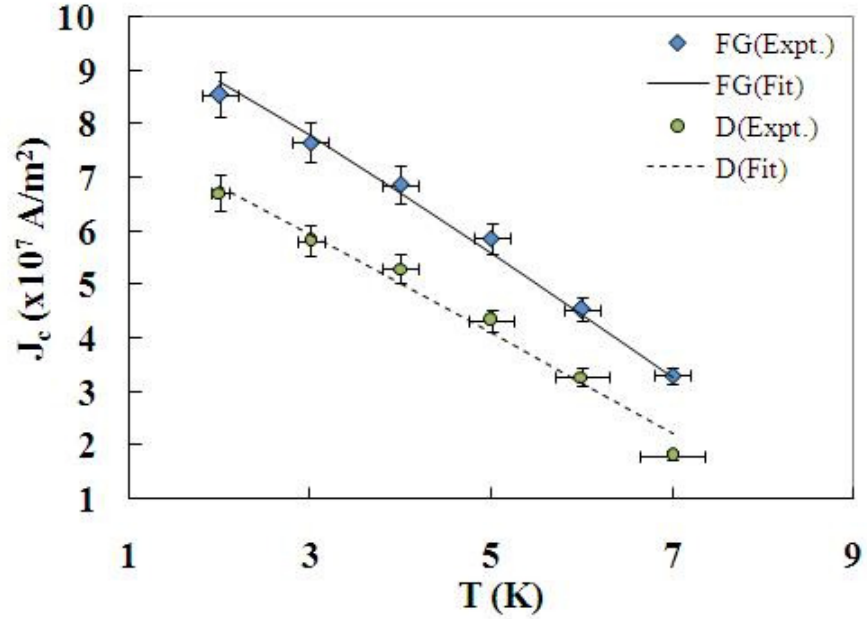


Figure 64: Variation of maximum critical current density with temperature; data and fit for sample D and FG

A comparison between the experimental data and a fit with equation 89 is shown in figure 64 for sample D and FG. Experimental values of T_c listed in table 13 were used to fit J_c at different temperatures. The fitted values of J_{cmax} at 0 K, $J_c(0)$ and parameter ‘K’ are listed in the table 16.

Table 16: Fitted Parameters $J_c(0)$ and K at 2 K after EP treatment

Sample	$J_c(0)$	K
A	5.87×10^7	0.65
B	7.91×10^7	1.0
C	6.17×10^7	0.52
D	8.64×10^7	0.95
FG	1.08×10^8	0.85

6.4.5] Pinning Force, F_p

The critical current flowing around the vortices in the mixed state exerts a Lorentz Force proportional to J_c and magnetic induction, B that is given by equation (90),

$$F_L = J_c \times B \quad (90)$$

Vortices are pinned at defects in the sample that prevents their movement. When the Lorentz force exceeds the pinning force the vortices begin to move (depinning). Thus the pinning force, is equal to Lorentz force when the vortices are stationary. The calculated J_c and volume pinning force, F_p are the bulk or the average properties of the measured sample.

The pinning force depends on temperature, applied magnetic field and microstructure of the sample under consideration. Any dislocation network, grain boundary or surface precipitate of the size of the order of the coherence length (about 40 nm in Nb) can act as a pinning center. These pinning centers are randomly distributed within the sample. Also, a single pinning center can pin one or multiple vortices at a particular site. In view of this scenario it is not possible to give an exact mathematical expression for the basic pinning force involved but one can study the scaling of the pinning force with various parameters.

Let's consider that ' F_p ' as the pinning force per unit volume, ' N_p ' as the number of pinning sites in a unit volume and ' f_p ' as the elementary pinning force involved. The nature of f_p is different for the line pinning or the point pinning. In a simple case where vortices are randomly distributed and the applied magnetic field is not very large (near H_{ffp}), each pinning site can be considered as independent and the total pinning force is just the summation due to all the pinning sites. Therefore the pinning force density has a simple dependence

$$F_p \propto N_p f_p \quad (91)$$

As the magnetic field is increased, the spacing between the vortices is reduced and as a result attractive or repulsive interaction between vortices results in a pinning force that is less than the mere summation of force due to individual vortices. In short, the average superconducting order parameter and hence the average magnetic induction is changed with variation in the applied magnetic field. Thus, the experimental curves show the maximum at particular value of ‘b’ [110].

An empirical scaling law of the pinning force per unit volume, F_p is given by [114,115],

$$F_p \propto H_{c2}^m b^p (1-b)^q \quad (92)$$

The temperature dependence of F_p is defined by the first term in equation (92) while terms containing reduced magnetic field define the basic pinning force. Figure 65 shows the plot of normalized pinning force as a function of reduced magnetic flux density at different temperatures for sample D and FG. The data is fitted using equation 93. A maximum pinning force is observed around $b = 0.3 \pm 0.06$ for all the LG samples. In case of FG sample, a maximum is observed at $b \sim 0.5$.

$$f = A b^p (1-b)^q \quad (93)$$

The very fact that the normalized pinning force plotted as a function of the reduced magnetic field, b follows the same curve at all temperatures indicates that the basic pinning force in a sample is unique and depends on the microstructure. Figure 66 shows the plot of the maximum pinning force, $F_{p,max}$ at different temperatures and the corresponding upper critical field, $H_{c2}(T)$ in logarithmic scale. The slope of the straight line fit gives the index ‘m’ and hence the dependence of F_p on $H_{c2}(T)$. In all the LG samples studied, ‘m’ is 1.7 ± 0.15 and in case of FG, $m \sim 1.9$. Also it is clear from figure 64 and 66 that J_c and F_p in LG material is less than FG material. As J_c is inversely proportional to grain size, the LG material has less J_c and F_p .

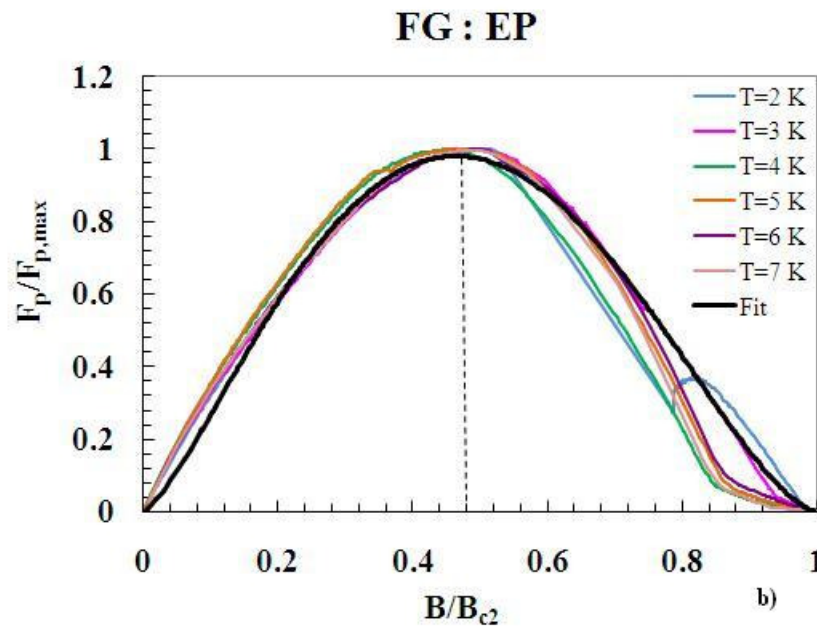
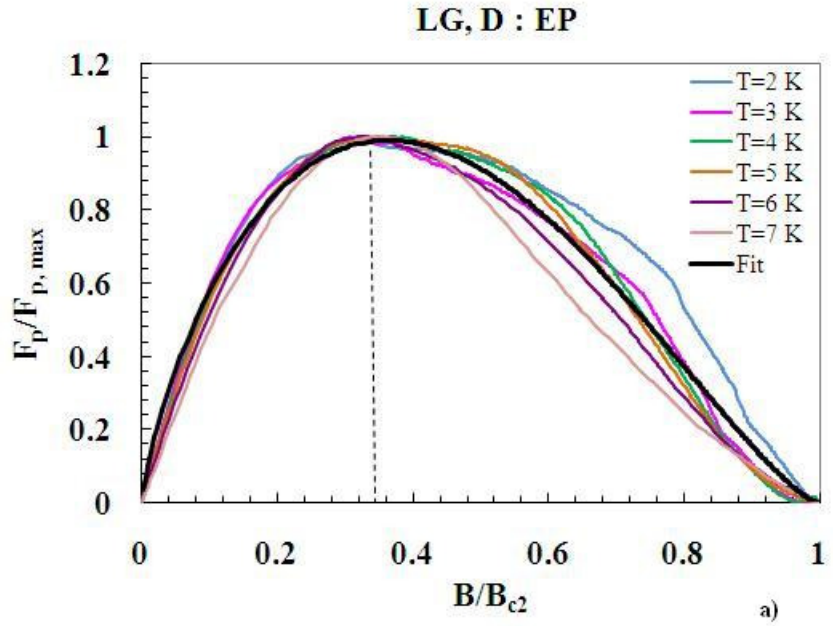


Figure 65: Normalized pinning force plotted against the reduced magnetic flux density, b ($=B/B_{c2}$) for all temperatures and fit using equation 11; a) LG sample D, $A=4.11$, $p=0.79$, $q=1.38$
 b) FG, $A=7.77$, $p=1.39$, $q=1.61$

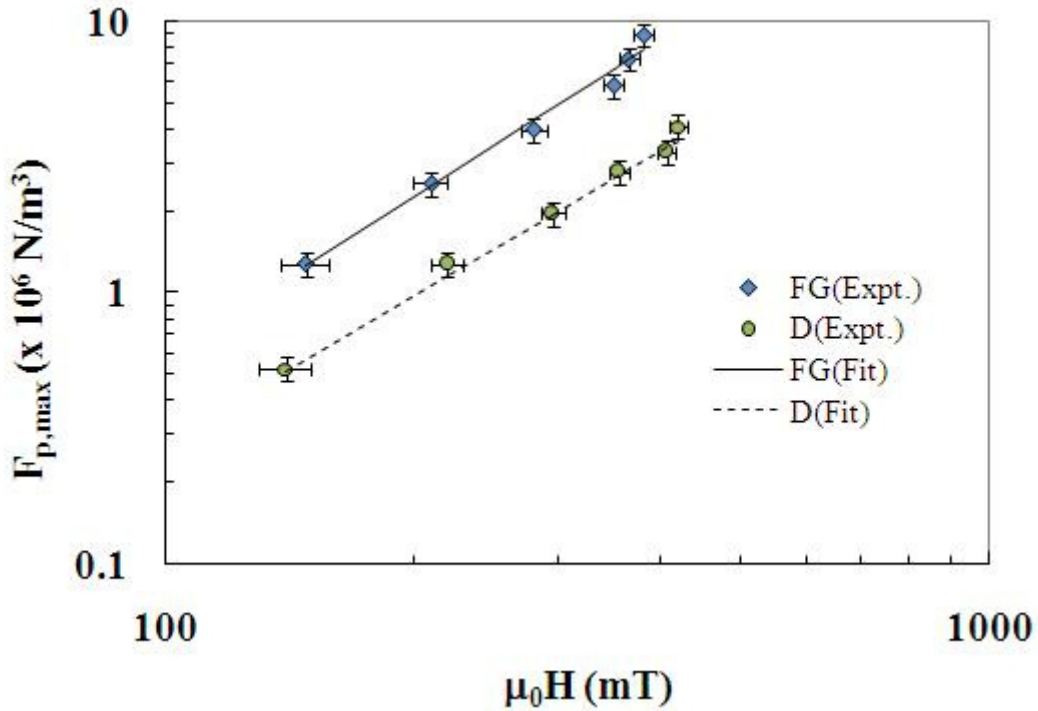


Figure 66: Plot of $F_{p,max}$ as a function of $H_{c2}(T)$ at different temperatures for sample D and FG

6.5] Discussion

The results from the thermal conductivity measurements of the LG samples show, unlike for the FG sample, the presence of a phonon peak at about 2 K. The requirement of niobium with $RRR > 250$ for SRF cavity production results only from the need for high thermal conductivity at 2 K. For materials such as LG Nb, where the temperature dependence of the thermal conductivity is non-monotonic between 2 K and 4.5 K because of the phonon peak, the RRR -value might not be the relevant parameter to be specified. The samples used for this study had been machined from a solid piece of Nb, therefore some mechanical damage to the surface is to be expected. Prior to the measurements reported in this article, the samples were etched by BCP and heat treated at 600 °C for 10 hr. in a vacuum furnace. These treatments seem to have recovered the phonon peak. The deep-drawing process to form half-cells introduces a plastic strain in the material of the order of 20% [116]. What heat treatment parameters will allow

recovering the phonon peak after such process still needs to be investigated. The presence of the phonon peak at 2 K makes LG Nb more advantageous than FG Nb with respect to thermal stability. This could lead to cavities with higher Q -values at 20-25 MV/m accelerating field levels.

The average value of $H_{c2}(0\text{ K})$ from DC magnetization measurements after EP is 435 mT, consistent with the value of 410 mT reported in [112]. While the RRR -values change by almost a factor of 3 among the various samples, the values of $H_{c2}(0\text{ K})$ are within 10%. The change in $H_{c2}(0\text{ K})$ after LTB is also within 10%. The average value of $H_{ffp}(0\text{ K})$ after EP is 189 mT, of the order of the thermodynamic critical field [112, 117] and consistent with $H_{c1}(0\text{ K})$ values between 185-195 mT reported in [118]. As a very smooth surface can be achieved with LG Nb, enhanced surface barrier can increase the onset of flux penetration above $H_{c1}(0\text{ K}) \sim 170\text{ mT}$. As for the upper critical field, the variation of $H_{ffp}(0\text{ K})$ among samples and before and after LTB is within 10%.

The critical fields measured in a $\sim 30\text{ }\mu\text{m}$ depth from the surface are lower than the bulk values by about 10%-20% after EP and increase by up to 10% after LTB. Once more, no significant difference between the LG samples of different purity and the FG sample was found. The average value of the surface $H_{ffp}(2\text{ K})$ is significantly higher after EP, compared to results after BCP treatment on the same samples [102] (164 mT compared to 110 mT). This result is consistent with the onset of the HFQ in SRF cavities typically being higher in EP-treated than BCP-etched cavities. Measurements of AC susceptibility by Kötzler et al., indicated that the ratio $H_{c3}^s/H_{c3} = 0.81$ was independent of surface treatments [109]. Our data indicate $H_{c3}^s/H_{c3} = 0.90 \pm 0.02$, independent of surface treatment or purity of the samples. The average value of the ratio H_{c3}/H_{c2} at 2 K after EP is 2.29 ± 0.02 , consistent with the results of Casalbuoni et al. [112]. This

ratio increases to > 2.65 after LTB indicating an increase of the field range where a coherent superconducting phase persists at the surface. The higher values of H_{c3}/H_{c2} at 2 K than the value of 1.925 calculated theoretically can be explained by the presence of an impurity layer at the surface, as shown in [112].

Differences in the area of the hysteresis loop and in the $\delta f(H)$ dependence above H_{c2} were found among the different samples, as can be seen, for example, in figure 62. The frequency shift δf is related to the penetration depth, $\delta\lambda$, so that, at the same field, a larger δf corresponds to a larger $\delta\lambda$. As can be seen in Fig. 62b, above H_{c2} , $\delta\lambda$ for a BCP-treated surface is larger than for an EP-treated surface. This can be explained by a shorter mean free path and therefore higher impurity content introduced by BCP at the surface.

DC magnetization measurements carried out on LG and FG sample allowed us to obtain field and temperature dependence of the critical current density and pinning force. The calculated J_c and F_p in LG samples is found to be smaller than the FG which is expected, due to fewer grain boundaries. Because of lower J_c value it is expected that LG Nb would have lower pinning efficiency or the flux trapping efficiency than FG. This should result in lower RF losses and hence high Q_0 value.

6.6] Conclusion

The data we presented indicate that superconducting properties such as bulk and surface critical fields and critical temperature do not depend significantly on the RRR of either LG Nb samples with RRR -values ranging between ~ 60 and ~ 160 or FG, high-purity Nb ($RRR > 250$), all samples being treated by EP. In particular, Ta concentrations of up to 1300 wt-ppm do not seem to influence the superconducting properties of the samples. This is consistent with the results from similar measurements by Roy et al. [119] and measurements on SRF cavities [100]. The

thermal conductivity of LG samples shows a phonon peak at ~ 2 K, which can be advantageous to maintain low RF losses in the operation of SRF cavities.

The results of the measurements of the onset of flux penetration in a ~ 30 μm thick surface layer, after various surface treatments such as BCP, EP and LTB, are consistent with changes in the onset of HFQ in SRF cavities after such treatments. These results, combined with those related to the surface critical field, suggest that the LTB allows improving the surface barrier and the field-range for coherent surface superconductivity.

The present experiments reveal certain advantages of LG over FG niobium material. These are following,

- (i) in spite of lower RRR, H_{c1} value of LG is comparable to FG.
- (ii) The phonon peak at 2^0K indicates better thermal stability.
- (iii) The lower J_c and F_p indicates the lower flux trapping during cavity cooldown and hence should exhibit higher Q_0 .

CHAPTER 7

CONCLUSION

This thesis covers the discussion of the design of fundamental power coupler for the superconducting accelerator. The coupler dimensions are optimized upon considering the effect of beam loading on the coupling. The external Q was evaluated using different computational methods using CST MWS. The Kroll-Yu method that was thought to be useful for the evaluation of low Q_{ext} has been successfully implemented for deduction high Q_{ext} . The comparison between different computational methods to evaluate Q_{ext} and experimental data shows the discrepancy above 10^7 . A ceramic window is another important subsystem of the power coupler which is a topic of further study. In case of multicell, the end cell is optimized so as to obtain the required coupling. A further analysis is required to understand the effect of field asymmetry introduced by single coupler and the transverse kick received by beam bunch due to the field [120].

A computer program is developed to study the multipacting in a coaxial coupler. The analytical solutions of e.m.fields are used to simulate the path of secondary electrons. The multipacting barriers are calculated for the designed coupler. The results are in accordance with scaling law. The calculated multipacting bands under traveling wave condition occur at power levels approximately four times higher than the standing wave condition. The multipacting can be completely avoided by DC biasing. A further up-gradation of code is required for the 3-d simulation of complicated structures.

Over the year high purity fine grain niobium material was used for cavity production but since 2005, large-grain (grain size of few cm^2) Nb sheets directly sliced from ingots are also considered for the cavity fabrication. The performance of the LG cavities is comparable to that of

standard fine-grain Nb cavities. Also, the large-grain Nb could be, on a large scale, cheaper than fine-grain material. The performance of SRF cavities made of bulk Nb is often limited by “high field Q-slope” or Q-drop [121]. A low-temperature (~ 120 °C for 12-48 h) baking (LTB) is often found to be beneficial in reducing the Q-drop. Preliminary theoretical and experimental studies indicate that magnetic vortices pinned near the surface are one among the possible causes for the Q-drop [122]. Magnetic vortices can be produced in SRF Nb cavities because of the imperfect shielding of the Earth’s magnetic field or thermoelectric currents during cavity cool down across the critical temperature.

The thesis covers the study of fine grain and large grain (Ingot A, B, C, D) used for the cavity production. A systematic study of superconducting properties of materials is carried out with the aim to understand the effect of various surface treatments on the superconducting properties of material and their possible effect on the cavity performance. Mainly the effect of electropolishing and low temperature baking is studied on the FG and LG niobium material. The bulk magnetization measurements are not sensitive to the surface treatments but the AC measurements do reveal some of the interesting features like reduction of penetration depth in EP samples compared to BCP and the increase in the H_{c3} after LTB which essentially indicates the increase in the range of coherent surface superconducting phase. The critical current density and pinning force is calculated from the DC magnetization data for LG and FG material. The calculated pinning force in LG material is smaller than FG material due to fewer grain boundaries. The change in critical current density and pinning force is negligible after LTB.

How LTB modifies the surface characteristics of the materials is the topic of further study and analysis. The study of new materials for SRF applications and understanding their limitations is another challenging area [123, 124].

REFERENCES

- 1] http://energy.nobelprize.org/reports/rubbia_report.pdf
- 2] http://fire.pppl.gov/rubia_iaea_2000.pdf
- 3] <http://www.world-nuclear.org/info/inf35.html>
- 4] <http://energy.nobelprize.org/presentations/rubbia.pdf>
- 5] “Shaping the Third Stage of Indian Nuclear Power Program”, DAE Report,
<http://www.dae.gov/pub/3rdstage.pdf>
- 6] P.K.Nema, P.Singh, P.Satyamurthy, S.B.Degweker, V.K.Handu, “ADS Program and associated developments in India-Roadmap and Status Activities”, ADS-INT-03, presented at IAEA Conference,

http://www-pub.iaea.org/MTCD/publications/PDF/P1433_CD/datasets/papers/ads_int-03.pdf
- 7] Cristian Bungau et. al.,” Neutron Spallation Studies for an Accelerator Driven Subcritical Reactor”, Proceedings of PAC09, Vancouver, BC, Canada
- 8] C.Pagani, P.Pierini, “High Power CW Superconducting Linacs for Nuclear Waste Processing”, 1999 Cryogenic Engineering Conference, Montreal, Canada, July 12-16, 1999
- 9] C.E.Reece, “Proceedings of the 3rd Workshop on RF Superconductivity”, Argonne, IL (1999), pp 545
- 10] P. Bernard, G. Cavallari, E. Chiaveri, E.Haebel et. al., “Proceeding of the 11th International Conference on High-Energy Accelerators”, Geneva, Switzerland (1980), pp. 878

- 11] V.Nanal, "Operational Experience of the SC Linac Booster at Mumbai", Proceedings of HIAT09, Venice, Italy
- 12] A.Roy, "SRF Activities at IUAC New Delhi and other Laboratories in India", Proceedings of SRF2007, Peking University, Beijing, China
- 13] P.Singh et. al. "Accelerator Development in India for ADS Program", *Pramana*, Vol. 68, No. 2, 331-342, DOI: 10.107/s12043-7-38-0
- 14] A.Roy, A.S.Dhavale, J.Mondal, K.C.Mittal, "RF Design of a Single Cell Superconducting Elliptical Cavity with Input Coupler", 12th Workshop on RF Superconductivity, Cornell University, USA (2005)
- 15] A.Roy, J. Mondal, K.C.Mittal, "Superconducting Elliptical 1050 MHz $\beta=0.49$ Cavity Design for High Current Proton Accelerator", InPAC'06, Mumbai, India, November 1-4, (2006)
A.Roy, J.Mondal, K.C.Mittal, "RF properties of 1050 MHz, $\beta=0.49$ elliptical cavity for high current proton acceleration", JINST report, JINST 3: P04002, 2008
- 16] A.S.Dhavale and K.C.Mittal, "Evaluation of external Q of the superconducting cavity using Kroll-Yu method", *Review Of Scientific Instruments* 77, 066101 (2006)
- 17] P. Kneisel, in Proceedings of the 9th Workshop on RF Superconductivity, Santa Fe, NM, 1999, edited by F. Krawczyk, (LANL, Los Alamos, NM, 2000), p. 328.
- 18] B. Visentin, J. P. Charrier and B. Coadou, in Proceedings of the 1998 European Particle Accelerator Conference, Stockholm, Sweden, 1998, edited by S. Myers, L. Liljeby, Ch. Petit-Jean-Genaz, J. Poole and K.-G. Rensfelt (IoP, Philadelphia, USA, 1998), p. 1885.
- 19] G.Ciovati and P.Kneisel, "Measurement of the high-field Q drop in the TM_{010} and TE_{011} modes in a niobium cavity", *Physical Review Special Topics-Accelerators and Beams*, 9, 042001 (2006)

- 20] J.H.Billen and L.M.Young, Los Alamos National Laboratory, Report no. LA-UR-96-1834,
2004
- 21] <http://www.ansoft.com>
- 22] <http://laacg1.lanl.gov/laacg/c-on-line/descriptions/mafia.html>
- 23] <http://www.cst.com>
- 24] T.P.Wangler, "Principles of RF Linear Accelerators", Chapter 1, pp 1-51, edited by John
Wiley & Sons, Inc., 1998
- 25] H.Padamsee, J.Knobloch, T.Hays, "RF Superconductivity for Accelerators", Chapter 1, pp 1-
55, edited by John Wiley & Sons, Inc., 1998
- 26] F.E.Terman, "Radio Engineering"
- 27] A.F.Harvey, "Microwave Engineering"
- 28] R.E.Collins, "Foundations of Microwave Theory"
- 29] Jordan, "Electromagnetic Fields"
- 30] N. Marcuvitz, "Waveguide Handbook", Radiation Laboratory Series, Vol. 10, published by
Boston Technical Publishers, Inc., USA, 1964
- 31] A.C.Rose-Innes, E.H.Rhoderick, "Introduction to Superconductivity", Pergamon Press Ltd.,
First edition 1969
- 32] R.P.Hueberner, "Magnetic flux structure in superconductors", by Springer-Verlag Berlin
Heidelberg, 1979
- 33] C.Pagani, "Technical Issues for Large Accelerators based on High Gradient SC cavities",
EPAC 2004, Lucerne, Switzerland
- 34] Michael Pekeler, "Fabrication of Superconducting Cavities for SNS", LINAC 2004

- 35] P.N.Ostroumov, “Application of International Linear Collider SC Cavities for acceleration of Protons”, *Phys. Rev. ST. Accel. Beams*, 1, 120101 (2007)
- 36] C. Pagani, “SRF Activities at INFN Milano - LASA”, SRF 2001
- 37] A.Bossoti et. al., “RF Tests of the beta = 0.5, 5 – cell Trasco Cavities”, EPAC 2004, Lucerne, Switzerland
- 38] M.B.Kurup, R.G.Pillay, and H.G.Devare, *Indian J. Phys.* **62A**, 706 (1988).
- 39] S.Ghosh et. Al., “Progress of the Superconducting Linear Accelerator Project at IUAC”, Proceedings of InPAC 2011, India.
- 40] K.W.Shepard et. al., “High Energy Ion Linacs based on Superconducting Spoke Cavities”, *Phys. Rev. ST. Accel. Beams* 6, 080101, 2003
- 41] <http://www-td.fnal.gov/projects/magnets.html>, <http://en.wikipedia.org/wiki/Niobium-titanium>
- 42] T.Boutboul, C.-H.Denarie, Z.Charifoulline, L.Oberli and R.Richter, “Critical Current Test Facilities for LHC Superconducting NbTi cable strands”, LHC Project Report 520, Presented at 5th European Conference on Applied Superconductivity, 26-30 August, 2001, Copenhagen, Denmark, <http://cdsweb.cern.ch/record/528591/files/lhc-project-report-520.pdf>
- 43] J.H.Schultz, P.Titus, J.V.Minervini, B.Smith, M.Takayasu, J.V.Minervini, “Advanced Magnets and Implications for BPX-II”, Burning Plasma Science Workshop, May 1-3, 2001
- 44] I.V.Bogdanov, V.I.Gridasov, K.P.Myznikov, P.A.Shcherbakov, P.I.Slabodchikov, V.V.Sytnik, L.M.Tkachenko, L.M.Vassiliev, “Development of a high gradient quadrupole magnet with a Nb₃Sn cable”,
<http://accelconf.web.cern.ch/AccelConf/e98/PAPERS/TUP05E.PDF>

- 45] “High $-T_c$ Superconductors: Electronic Structure”, talk based on manuscript for an article ‘Encyclopedia of Materials’, edited by K.H.J.Buschow et. al., Elsevier, Oxford 2003,
<http://www.ifw-dresden.de/institutes/itf/members/helmut/v-a61.pdf>
- 46] A. Gurevich , “Multilayer coatings of superconducting cavities: challenges and opportunities”, presented at 15th SRF Workshop, Chicago, 2011 (SRF2011)
- 47] G.Ciovati, “Investigation of the superconducting properties of niobium radio-frequency cavities”, Ph.D.Thesis, August 2005
- 48] Hui Tian, “Surface study of Niobium for Superconducting Radio Frequency (SRF) Accelerators”, Ph.D. Thesis, August 2008
- 49] G.Devanz, H.Safa, C.Travier, “Preliminary design of a 704 MHz power coupler for a high intensity proton linear accelerator”, 7th European particle accelerator conference, Vienna, Austria (EPAC 2000)
- 50] G.Geschonke, “Superconducting structures for high intensity linac applications”, XVIII International Linac Conference, Geneva, Switzerland, 26-30 August, 1996, CERN-SL-96-68 RF
- 51] E.Chojnacki, S. Belomestnykh, “RF Power coupler performance at CESR and study of multipactor inhibited coupler”, 9th Workshop of RF Superconductivity , Santa Fe, No 1-5, 1999
- 52] S. Mitsunobu et. al., “High power input coupler for KEKB SC cavity”, 9th Workshop of RF Superconductivity , Santa Fe, No 1-5, 1999
- 53] H.P.Kindermann, E.Haebel, M.Stirbet, “Status of RF power couplers for superconducting cavities at CERN”, European Particle accelerator conference, Rome, Italy, June 10-14, 1996

- 54] S. Noguchi et. al., “Couplers-Experience at KEK”, 4th workshop on RF Superconductivity, August 1989, KEK, Tsukuba, Japan, vol. , pp 397-412, KEK Report 89-21
- 55] V. Nguyen et. al., “Development of a 50 kW CW L-band rectangular window for Jefferson lab FEL Cryomodule”, 1999 Particle Accelerator Conference, New York, March 1999, vol. 2, pp 1459-1461
- 56] E.N.Schmierer et. al., “Results of APT RF Power Coupler Development of Superconducting linacs”, 10th Workshop on RF Superconductivity, Tsukuba, Japan, September 2001
- 57] M.Stirbet, I.E., Campisi, K.M.Wilson, M.Drury, G.K.Davis, T.Powers, Proceedings of LINAC 2000, Gyeongju, Korea, pp. 728-730
- 58] D.Boussard, E. Chiaveri, E.Haebel, H.P.Kindermann, R.Losito, S.Marque, V.Rodel and M.Stirbet, “The LHC Superconducting cavities”, Particle Accelerator Conference, New York, 1999
- 59] H.P.Kindermann, M.Stirbet, “The Variable Power coupler for the LHC Superconducting cavity”, 9th workshop on RF Superconductivity, Santa Fe, NM, November 1999, pp. 566-569
- 60] S.Belomestnykh, “Review of high power CW coupler for superconducting cavities”, Workshop on High Power Coplers for Superconducting Accelerators, Jefferson lab., USA, 2002, SRF021105-09
- 61] V.Katalev, S.Choroba, “Tuning of External Q and phase for the cavities of a Superconducting Linear Accelerator”, Proceedings of LINAC 2004, Lubeck, Germany
- 62] P. Balleyguier, “External Q Studies For APT SC-cavity Couplers”, CEA/DPTA, 91680 Bruyeres-le-Chatel, France, P. 133-135

- 63] A.Roy, et. al., “Preliminary Design of RF Superconducting Single Cell Elliptical Cavity for Proton Linac”, Indian Particle Accelerator Conference(INPAC2005), March 2005, VECC, Calcutta.
- 64] H.Makio, E. Somersalo, P. Yla-Oijala et. al. “Computational methods for analyzing Electron Multipacting in RF structures”, Proceedings of ECMI, 1998.
- 65] “CST Microwave Studio™”, Version 3, Tutorials
- 66] K.Ko, C.-K.Ng, W.B.Herrmannsfeldt, “Modeling Accelerator Structures And RF Components”, Stanford Linear Accelerator Centre, Report No. SLAC-PUB-6084, March 1993, (A)
- 67] V.Shemelin and S.Belomestnykh, “Calculation of the B-cell Cavity External Q with MAFIA and Microwave Studio”, Cornell Publication:SRF020620-03 (2002).
- 68] J.C.Slater, “Microwave Electronics” (Van Nostrand, New York, 1950), Chap. 5, p. 85
- 69] N.M.Kroll, D.U.L.Yu, “Computer determination of the external Q and resonant frequency of waveguide loaded cavities”, SLAC-PUB-5171, Jan 1990 (A)
- 70] P.Balleyguier, “A straightforward method for cavity external Q computation”, Particle Accelerators, Vol. 57, p 113, 1997
- 71] P.Balleyguier, “External Q computation in cavities with MWS”, CST User Meeting, Darmstadt, September 2004.
- 72] G.L.Ragan, “Microwave Transmission Circuits”, Vol.9, Radiation Laboratory series, McGraw Hill Book Company, 1948

- 73] Sun An, H.S.Kim, Y.S.Cho, B.H.Choi, “Design of a fundamental power coupler for the PEFP superconducting RF cavities”, Journal of the Korean Physical Society, Vol. 52, No. 3, march 2008, pp. 793-798
- 74] V. Shemelin, “Optimal choice of cell geometry for a multicell superconducting cavity”, Physical Review Special Topics – Accelerators and Beams, **12**, 114701 (2009)
- 75] J. Sekutowicz, K.Ko et. al., “Design of a low loss RF cavity for the ILC”, SLAC-PUB-11730
- 76] E.L.Ginzton, “Microwave Measurement”, Chapter 10, pp435, McGraw Hill Book Company Inc., 1957
- 77] Y. Kang, S. Kim, M. Doleans et. al., Proceedings of 2001 Particle Accelerator Conference,
- 78] S.I.Kurokawa et. al., “Frontiers of Accelerator Technology”, Hayama/Tsukuba, Japan, World Scientific
- 79] E.Chivari, “Superconducting RF Cavities: Past, Present and Future”, IEEE Transactions on Applied Superconductivity, Vol. 13, No. 2, June 2003
- 80] P.Yla-Oijala, D.Proch, “MutiPac-Multipacting simulation package with 2D FEM field solver”, Proceedings of the 10th Workshop on RF Superconductivity, Tsukuba, Japan, 2001
- 81] G.Devanz, “Multipactor Simulations in Superconducting cavities and Power Couplers”, Phys. Rev. Special Topics – Accelerator and Beams, Vol. 4, 012001, 2001
- 82] R. Parodi, P.Fernandes, “TWTRAJ Users Guide”, LAL SERA 90-224, 20 December 1990
- 83] R.Ballantini, A.Chincarini, G.Gemme, R.Parodi, A.Podesta, “TWTRAJ, a Computer code for MP Simulation in Superconducting cavities”, Proceedings of the 10th Workshop on RF Superconductivity, Tsukuba, Japan, 2001
- 84] R. Ferraro et. al., “Guide to Multipacting/ Field Emission Simulation Software, 6th Edition”, Cornell LNS Report SRF/D-961126/10, 1996,

- W.Hartung, F.Krawczyk, H.Padamsee, “Studies of Multipacting in Axisymmetric Cavities for medium velocity beams”, Proceedings of the 10th Workshop on RF Superconductivity, Tsukuba, Japan, 2001
- 85] R.L.Geng et. al., “Exploring Multipacting Characteristics of a Rectangular Waveguide”, Proceedings of PAC99, New York, USA, 1999
- 86] S.Humphries, jr., TRAK3D, <http://www.fieldp.com/maze/tra3d.html>
- 87] L.V.Kravchuk et. al., “The Computer Code for Investigation of the Multipactor discharge in RF cavities”, Proceedings of PAC99, New York, USA, 1999
- 88] F.L.Krawczyk, “Status of Multipacting simulation capabilities for SCRF applications”, LA-U/R-01-6447, Invited talk published in the Proceedings of the 10th Workshop on RF Superconductivity, Tsukuba, Japan, 2001
- 89] J.R.M.Vaughan, “A New Formula for Secondary Emission Yield”, Transactions on Electron Devices, Vol. 36, No. 9, September 1989, p 1963-1967.
- 90] S. Humphries, “Modeling Secondary Emission in a Finite – element Multipactor code”, 9th Workshop on RF Superconductivity, Nov. 1-5, 1999, Los Alamos, California, USA.
- 91] W.H. Press, S.A. Teukolsky et. al., “Numerical recipes in C”, Second Edition, Cambridge University Press, 1992, p. 278-279.
- 92] L.Ge, C.Adolphsen, L.K.Ko, Lee, Z.Li et.al., “Multipacting Simulations of TTF-III Power Coupler Components”, Proceedings of PAC07, Albuquerque, New Mexico, USA, 2007
- 93] B. Rusnak, F.Wang, et.al. , “High Power Coupler Component Test Stand Status and Results”, UCRL-CONF-231932, June 20, 2007

- 94] R.E.Kirby, F.K.King, “Secondary Electron Emission Yields from PEP II Accelerator Materials”, SLAC-PUB-8212, October (2000),
R.E.Kirby, F.K.King, “Secondary Electron Emission from Accelerator Materials”, SLAC-PUB-8380, February(2000)
- 95] E. Somersalo, P. Yla-Oijala et. al. “Analysis of Multipacting in Coaxial Lines”, Proceedings of Particle Accelerator Conference, Dallas, USA, p. 1500-1502, 1995.
- 96] D.Nayak and I.Ben-Zvi, “Supressing multipacting in a 56 MHz quarter wave resonator”, Physical Review Special Topics – Accelerators and Beams, 13, 052001, 2010
- 97] P. Yla-Oijala, M.Ukola, “Supressing Electron Multipacting in Ceramic Windows by DC bias”, *Nucl. Instr. and Methods A*, 474, 3, p. 197-208, 2001
- 98] J. Lorkiewicz, B.Dwersteg, A.Brinkmann, W.Moeller et. al., “Surface TiN coating of TESLA Couplers at DESY as an antimultipacting remedy”, Proceedings of the 10th Workshop on RF Superconductivity, Tsukuba, Japan, 2001
- 99] G. Ciovati, *J. Appl. Phys.* **96**, 3 (2004).
- 100] P. Kneisel et al.,”Preliminary Results from Single Crystal and Very Large Crystal Niobium Cavities” in *Proceedings of the 2005 Particle Accelerator Conference*, edited by C. Horak, ORNL/SNS, Knoxville, TN, 2005, pp. 3991-3993.
- 101] G. Ciovati et al., “A Coaxial TE011 Cavity and a System to Measure DC and RF Properties of Superconductors” in *Proceedings of the 13th Workshop on RF Superconductivity-2007*, edited by J. K. Hao, S. L. Huang and K. Zhao, Peking University, Beijing, China, 2007, pp. 98-102.

- 102] J. Mondal et al., “Characterization of Ingot Material for SRF Cavity Production” in *Proceedings of the 14th International Conference on RF Superconductivity-2009*, edited by M. Abo-Bakr et al., Helmholtz Zentrum, Berlin, Germany, 2009, pp. 455-461.
- 103] N. J. Imfeld, W. Bestgen, and L. Rinderer, *J. of Low Temp. Physics*, **60**, 223-238 (1985).
- 104] A. L. Schawlow and G. E. Devlin, *Phys. Rev.*, **113**, 120-126 (1959).
- 105] W. Schwarz and J. Halbritter, *J. Appl. Phys.*, **48**, 4618-4626 (1977).
- 106] C.R.Hu and V.Korenman, *Phys. Rev.*, **185**, 672-682 (1969).
- 107] S.B.Roy, G.R.Myneni, and V.C.Sahni, *Supercond. Sci. Technol.*, **21**, 065002 (2008).
- 108] E. Helfand and N. R. Werthamer, *Phys. Rev.*, **147**, 288-294 (1966) and A. Gurevich (private communication).
- 109] J. Kötler, L. von Sawilski, and S. Casalbuoni, *Phys. Rev. Lett.*, **92**, 067005 (2004).
- 110] R.W.Heussner, C.Bormio Nunes, P.J.Lee, D.C.Larbalestier and P.D.Jablonski, “Properties of niobium-titanium superconducting wires with Nb artificial centers”, *J.Appl.Physics* 80(3), 1996
- 111] W.A.Fietz and W.W.Webb, “Hysteresis in Superconducting Alloys – Temperature and Field Dependence of Dislocation Pinning in Niobium Alloys”, *Phys.Rev.*, Vol. 178, No. 2, 1969
- 112] S. Casalbuoni, E.A.Knabbe, J.Kotler, L.Lilje, L. von Sawilski, P. Schmuser, “Surface Superconductivity in Niobium for Superconducting RF Cavities” , *NIM A538(205)*,45-64, DOI : 10.116/j.nima.2004.09.003
- 113] T.Matsushita, “Flux Pinning in Superconductors”,
- 114] E.H.Brandt, “The flux-line lattice in superconductors”, *Reports on Progress in Physics*, 58, 1465-1594, 1995, doi: 10.1088/0034-4885/58/11/003

- 115] P.H.Kes, C.A.M. van der Klein and D. de Klerk, “Calculations on the Reversible and Irreversible magnetic Behavior of Low Kappa Type –II Superconductors”, *Journal of Low temp. Physics*, Vol. 10, Nos. 5/6, 1973
- 116] T. Gnäupel-Herold, G. R. Myneni, and R. Ricker, “Investigation of Residual Stresses and Mechanical Properties of Single Crystal Niobium for SRF Cavities“, in *Single Crystal-Large Grain Niobium Technology: Proceedings of the International Niobium Workshop-2006*, edited by G. R. Myneni, T. Carneiro and A. Hutton, AIP Conference Proceedings 927, Melville, NY, 2007, pp. 48-59.
- 117] D. K. Finnemore, T. F. Stromberg, and C. A. Swenson, *Phys. Rev.*, **149**, 231-243 (1966).
- 118] K. Saito, “Theoretical Critical Field in RF Application”, in *Proceedings of the 11th Workshop on RF Superconductivity-2003*, edited by D. Proch, DESY, Germany, 2003, pp. 1-16.
- 119] S. B. Roy, V. C. Sahni, and G. R. Myneni, “Research & Development on Superconducting Niobium Materials via Magnetic Measurements”, AIP Proceedings on Symposium on Superconducting Sci. and Technology of Ingot Niobium (SSTIN10), Sep. 22-24, 2010, TJNAF, Newport News, VA
- 120] S.V.Kutsaev, M.V.Lalayan et. al., “Analysis of Input Coupler Asymmtry Influence on Beam Dynamics in accelerators with superconducting cavities”, *Proceedings of Linac08*, Victoria, BC, Canada.
- 121] Kneisel P, Myneni G R, Ciovati G, Sekutowicz J and Carneiro T 2006 *Proc. of International Niobium workshop on Single Crystal – large Grain Technology AIP Conf. Proc. 927 Araxa Brazil 84*
- 122] Gurevich A and Ciovati G 2008 *Phys. Rev. B* **77** 104501

- 123] Tsuyoshi Tajima, “LANL Activities on New Materials for SRF Cavities”, presented at Pushing the limits of RF Superconductivity Workshop at Argonne National Laboratory, Sept. 22-24, 2004
- 124] A. Gurevich and P.Bauer, “SRF material R&D”, presented at AARD Meeting, Fermilab., Feb. 15, 2006.